TRANSPORT MODELS FOR THE INTERENDOTHELIAL CLEFT

by

BING-MEI FU

A dissertation submitted to the Graduate Faculty in Engineering in partial fulfillment
of the requirements for the degree of Doctor of Philosophy,
The City University of New York

1995

This manuscript has been read and accepted for the Graduate Faculty in Engineering in satisfaction of the dissertation requirement for the degree of doctor of Philosophy.

5/16/95

Date

Professor Sheldon Weinbaum
Chair of Examining Committee

5/16/95

Date

Professor Gerard G. Lowen
Executive Officer

Dr. Fitz-Roy E. Curry
Dr. Stephen C. Cowin
Dr. Peter Ganatos
Dr. David S. Rumschitzki

Supervisory Committee

The City University of New York

Abstract

TRANSPORT MODELS FOR THE INTERENDOTHELIAL CLEFT

by

Bing-Mei Fu

Advisers: Professor Sheldon Weinbaum, Professor Fitz-Roy E. Curry

Vascular endothelium is the principal barrier to, and regulator of, material exchange between circulating blood and the body tissues. The ultrastructural pathways and mechanisms whereby endothelial cells and the clefts between the cells modulate capillary permeability to water and solutes have been a central unsolved question in microvessel transport since the early 1950's. Three new theoretical models have been developed in this research to examine the role of the detailed structure of the intercellular cleft and its components in the regulation of capillary permeabilities. These new approaches have resulted in a major revision of current ideas about the pathways for water and solutes through the junction strand and the structures that determine the molecular filter.

The combined junction-orifice-fiber entrance layer model proposed in this dissertation predicts that for measured hydraulic conductivity to be achieved the fiber layer must be confined to a relatively narrow region at the entrance to the cleft where it serves as the primary molecular filter provided the fiber matrix forms an ordered array. This model also provides an excellent fit for the hydraulic conductivity and the diffusive permeability data for solutes of size ranging from potassium to albumin for frog mesenteric capillary provided the junction strand contains at least two types of pores, infrequent 20 x 150 nm large orifice breaks and a continuous ~ 2 nm narrow slit or closely spaced 1.5 nm radius circular pores. The time dependent diffusion wake model in this study provides a new interpretation of labeled tracer

studies to define the permeability pathways for low molecular weight tracers which depend on the time dependent filling of the extravascular space. This model and recent microscope experiments with low molecular weight fluorescent probes support the existence of a previously unrecognized family of ~ 2 nm small pores that are distributed along the length in the junction strand. Furthermore, the convective-diffusion wake model developed herein, in conjunction with related experiments, is designed to evaluate the relative contribution of structures associated with the junctional strand and the fiber matrix to the molecular filter at the microvessel wall.

ACKNOWLEDGEMENTS

I would like to express heartfelt thanks to my mentor, Professor Sheldon Weinbaum, for his abundant encouragement, advice and patience, for always stimulating my confidence and providing me with an environment which allowed me to do research independently. Thanks also to Dr. Fitz-Roy E. Curry, my co-mentor, for his generous support and guidance which led me to enter into biomedical engineering, the interdisciplinary and the challenging field of research.

My gratitude is also to Professor Peter Ganatos, for his clear and concise explanation for any question whenever I brought to him. To Professor David Rumschitzki, for his caring critic. To Dr. Roger Adamson, for his considerate help when I was in Davis. To Professor Latif Jiji and Professor Andreas Acrivos, for their advice beyond heat transfer and fluid mechanics. To Dean Gerard Lowen, for his kindly encouragement.

And to my roommates, Professor Xu, Professor Zhu and their son, James, for giving me a home away from home. To friends who shared my joys and pains throughout the course of this work: Dan, Paul, Jie, Ruey, Yu, Fan, Ke, Liang, Yongyi, Yulong, Yaqi, Gangmin, Dajun, Hanqin, Jingnan, Mayumi, and Ping. And to Charles, for his love.

Finally, I wish to dedicate this work to my parents and sisters for loving me unconditionally.

TABLE OF CONTENTS

LIST OF FIGURES

CHAPTER 1

INTRODUCTION

The ultrastructural pathways and mechanisms whereby endothelial cells and the clefts between the cells modulate capillary permeability to water and solutes have been a central unsolved question in microvessel transport since the early 1950's. The present research examines three problems describing different but related aspects of capillary permeability corresponding to the intercellular cleft and its structural components. The first problem describes a new combined junction-orifice-fiber entrance layer model for capillary permeability. The new formulation is based on the predictions in Weinbaum et al. (1992) and the new information on junction strand structure obtained from recent serial section reconstructions of the cleft in Adamson and Michel (1993). The second problem describes a time dependent diffusion wake model for the spread of low molecular weight tracers on the tissue side of the junction strand and the time dependent filling of the extravascular tissue space. This model provides a new approach for detecting junction strand interruptions and small pores that lie beyond the resolution of conventional transmission electron microscopy. It also provides a new interpretation of labeled tracer studies which have been used to define the permeability pathways for low molecular weight tracers. It is shown that this interpretation depends critically on the time dependent filling of the extravascular space. In the third problem, a time dependent convective-diffusion model is developed to analyze the two-dimensional wake formed by the spreading of high molecular weight tracers. This model, in conjunction with related experiments which are currently in progress, is designed to evaluate the relative contribution of structures associated with the junctional strand and the fiber matrix to the molecular filter at the microvessel wall.

The microvascular bed is the primary location where water and solutes associated with nutrition and metabolism are exchanged between circulating blood and body tissues. Capillaries are the smallest ramifications of the microvessels. Capillary walls consist of endothelium, basal lamina and pericytes. The interendothelial cleft is widely believed to be the principal pathway for water and hydrophilic solute (such as glucose, amino acids, vitamins, hormones) transport through the capillary wall (Starling, 1909; Pappenheimer, 1951, 1953; Landis and Pappenheimer, 1963; Karnovsky, 1967, 1968; Renkin and Curry, 1978; Wissig, 1979). Direct and indirect evidence indicates that there are junctional strands with discontinuous leakages (Wissig, 1979; Bundgaard, 1980, 1984; Crone, 1981; Adamson and Michel, 1993) and fiber matrix components (Luft, 1966; Turner et al., 1983; Gingell, 1976; Simionescu et al., 1981, 1985; Schneeberger and Hamelin, 1984; Adamson, 1990; Adamson and Clough, 1992) at the endothelial surface and in the wide portion of the intercellular cleft. This evidence is the basis for the one-dimensional pore, restricted slit and fiber matrix theories which are summarized later in this section. The detailed three-dimensional analysis presented by Weinbaum et al. (1992) indicates that neither pore, restricted slit nor fiber matrix theory can by itself successfully explain the large body of experimental measurements for the filtration, permeability and selectivity coefficients in isolated capillaries.

An important difficulty in reconciling these different approaches is that the details of the structural features delineating the narrow regions of the junctions lie beyond the resolution of the electron microscope. Even the more sophisticated recent three-dimensional theoretical models based on the solution to the pure filtration and pure diffusion problem through a junction strand with a single size pore system cannot predict all the measured permeability coefficients (Tsay et al., 1989; Weinbaum et al., 1992). Using the recent experimental observations of Adamson and Michel (1993) for the junction strand structure, we will see in Chapter 2 that a

multiple size junctional pore system, which includes tiny pores or slits that are permeable to small solutes and large pores responsible for large solute permeability, when combined with a narrow fiber entrance layer in the cleft, can explain most of the available data for isolated perfused frog mesentery capillaries.

Chapter 3 of this research describes a new approach to explore junction strand structure. Instead of observing the junctional strand structure directly, we attempt to construct a detailed picture of the junctional strand as a transport barrier from a combined two-dimensional theoretical and experimental analysis of the diffusive wake formed by the spreading of low molecular weight tracers (such as lanthanum and sodium fluorescein) on the downstream side of the junction strand discontinuities. Important additional evidence in support of the small pore system proposed in Chapter 2 is obtained from the time dependent studies of the penetration of lanthanum in the cleft on the abluminal side of the junction strand, confocal microscopic measurements of the spread of sodium fluorescein in the tissue surrounding a perfused microvessel and a theoretical model which describes the time dependent labeling behavior observed in these experiments.

Another experimental difficulty is that the existence of fiber matrix components cannot be directly visualized in the wide part of the cleft. For this reason, it hasn't been clear whether the junctional barrier or the fiber matrix is the primary structure in determining the selectivity of the capillary wall. In Chapter 4, a time dependent convective-diffusion wake model for high molecular weight tracers is proposed to design experiments that can test for the location of the molecular filter. Before presenting the current work, we shall first review previous experimental and theoretical studies that have explored the structure function relationship in capillary permeability.

1.1 EXPERIMENTAL STUDIES ON THE INTERCELLULAR CLEFT

Vascular endothelium is the principal barrier to, and regulator of, material exchange between circulating blood and the body tissues. Freeze fracture studies and ultrathin serial sections have demonstrated that endothelial cells are joined by an array of junctional strands which are interrupted at intervals allowing passage of water and solutes. Fig. 1.1 shows a schematic drawing of the organization of tight junctions of capillary endothelium (Bundgaard, 1984). Cytochemical and permeability studies also indicate that at least part of the cleft may be filled with a fibrous matrix. These two structures form the principal barriers for water and solute transport in the capillary wall.

Numerous investigations have been conducted to resolve the detailed structure of the junctional strand. Karnovsky (1967,1968) showed that the tight junctions of heart and skeletal muscle capillaries were permeable to horse-radish peroxidase molecules (HRP, 6 nm diameter). Wissig (1979) proposed that the passage of microperoxidase (MP, 2 nm diameter) in the clefts of mouse skeletal muscle capillaries could occur either via tortuous pathways formed by discontinuities in multiple strand arrays or direct pathways through the protein strands. Firth et al. (1983) in his random thin section and freeze-fracture studies for pig placental capillaries indicated that there were one to five tight junction strands in series. He proposed that the tight junctions were formed by equally spaced junctional proteins with 5.5 x 11 nm rectangular pores between them and suggested that the thickness of these junctional bars was also approximately 11 nm. Sibley et al. (1982, 1983) observed that hemepeptide tracers of 6 nm diameter could penetrate the lateral intercellular space of a pig placental capillary.

Bundgaard (1984) was the first to attempt to reconstruct the three-dimensional junction strand ultrastructure using serial section electron microscopy. In his study, rat heart capillaries were analyzed using conventional 40 nm thin and 12.5 nm ultrathin serial section electron

microscopy. Large pores of 10-20 nm height and 20-80 nm length and small pores of 4-5 nm height and 5-30 nm length were observed. He sketched the latter pores as short discontinuities in the junction protein strands. In contrast to Bundgaard's work, Ward et al. (1988) examined the 3-D features of the junction strands of rat cardiac capillaries by using a goniometric tilting technique. After considering the tilting effects, they claimed that more than 70 percent of the random thin sections of junctional clefts were actually open and concluded that the pathway for small and intermediate solutes were not formed by interruption in continuous lines of membrane fusion but by continuous junctional regions with an approximate opening of 5 nm width. Recently, Adamson and Michel (1993) investigated the ultrastructure of the endothelial intercellular clefts of frog mesenteric capillaries using ultrathin serial sections of 30-40 nm thickness and serial reconstruction. They observed rather long breaks of typically 150 nm width and the same gap height 20 nm as that of the wide part of the cleft. A continuous ~ 2 nm translucent narrow slit along the outer leaflets in the tight junction was also revealed on a tilting stage.

The structure of the fiber matrix in the intercellular pathway is less clearly identified. Using ruthenium red staining, Luft (1966) showed that there is a 'fluffy layer' on the luminal surface of endothelial cells. Turner et al. (1983) observed that cationized ferritin was bound in a thin layer of 20-30 nm thickness near the endothelial cell surface. In general, there are anionic sites on the endothelial surface which correspond to ciliated glycoproteins embedded in the cell plasma membrane in association with proteoglycan and plasma proteins (Gingell 1976; Simionescu et al. 1981, 1985; Schneeberger and Hamelin 1984). This endothelial cell glycocalyx might correspond to the fiber matrix in the fiber matrix hypothesis proposed by Curry and Michel (1980). Firth et al. (1983), in his work on pig placental capillaries, suggested that there were linking molecules of 5 to 10 nm radius spanning the wide portion of the cleft.

Silberberg (1987) also proposed that the linking molecules might be necessary to provide the nearly uniform cleft height observed in the wide portion of the clefts. Adamson (1990) studied the fiber matrix by comparing normal capillary hydraulic conductivity L_p with L_p measured after partial enzymatic degradation of the endothelial cell glycocalyx. A 2-3 fold increase in L_p was observed in the frog mesentery capillary. Evidence for regularly spaced, cleft-spanning fiber matrix structures within the interendothelial cleft has been recently reported by Schulze and Firth (1992). In the study of Satcher (1993), fine perpendicular fibers could be clearly seen at the entrance to the cleft. Adamson and Clough (1992) used cationized ferritin as a marker of cell surface glycocalyx and observed that when the vessels were fixed after perfusion with frog plasma, the ferritin penetrated the outer region of the glycocalyx to a depth of 20 to 30 nm and that there was a separation layer of 32 nm thickness between this layer and the membrane surface.

1.2 THEORETICAL MODELS

Permeability studies show that the capillary wall behaves as a passive membrane for water and small hydrophilic solute transport (Crone and Levitt, 1984; Michel, 1984). This allows the interpretation of permeability properties in terms of capillary wall structure. The membrane transport properties are often described by Kedem-Katchalsky equations derived from the theory of irreversible thermodynamics

$$J_s = PRT\Delta C + (1 - \sigma)CJ_v \tag{1.1}$$

$$J_v = L_p(\Delta p - \sigma RT\Delta C) \tag{1.2}$$

where J_s and J_v are the solute and total volumetric fluxes; ΔC and Δp are the concentration and pressure difference across the membrane. L_p and P are the hydraulic and diffusive permeability

and σ is the reflection coefficient. All of the permeability measurements have been interpreted in terms of these three coefficients which are measured experimentally. Prior to the late 1980's, there were two major one-dimensional theories: the pore-slit and the fiber matrix theory, which attempted to correlate cleft structure with the large amount of experimental data for these coefficients.

1.2.A Pore-Slit Theory

In the pore-slit theory, hydrophilic pathways in transcapillary transport are assumed to be formed by pores or slits in the junctional strand arrays. In the classical pore theory first proposed by Pappenheimer et al. (1951, 1953), uniform cylindrical pores or uniform slits were used to represent these pathways. Since a uniform height slit could not account for both hydraulic conductivity and reflection coefficient data, this simple model was then modified by including a junctional constriction in an otherwise uniform width cleft, see Fig. 1.2(a) (Weinbaum et al., 1992). Provided this constriction was of 6-8 nm gap height, it could serve as the molecular filter and satisfy the measured reflection coefficients for solutes of 1.5-3.5 nm radius (Curry, 1986). A simple one-dimensional model is used to describe both filtration and solute transport. The basic assumption of this one-dimensional model is that the lateral spreading at the entrance/exit of junctional pores is negligible. Permeability is thus proportional to the length of open junction. Using one-dimensional models, Crone and Levitt (1984) estimated that the hydraulic conductivity L_p and diffusive permeability P of small solutes could be accounted for if 10% of the junction barrier had these constricted slit openings in muscle capillaries and 90% of the junction length were open in frog mesentery capillaries. The major discrepancies between the predictions of this one-dimensional model and the experimental measurements are: (1) it underestimates the diffusional resistance to large solutes when the

length of open junction is set to account for the diffusive permeability to small solutes and it overestimates the hydraulic resistance of the microvessel wall when the length of open junction is set to account for the diffusive permeability to small solutes; (2) the serial section studies (Bundgaard, 1984; Adamson and Michel, 1993) showed that the gap height at the interruptions in the junction strand are the same as the remaining wide part of the cleft (~ 20 nm), suggesting that the strand itself is probably not the site of the primary molecular sieve. Furthermore, the 40-80 nm and 150 nm breaks observed by these investigators were very infrequent and represented a fractional length of open junction that was small compared to the length predicted by the one-dimensional pore-slit models for frog mesentery; and (3) it can not explain the more than two fold decrease in hydraulic resistance after enzymatic removal of the endothelial glycocalyx in frog mesenteric capillaries (Adamson, 1990).

1.2.B Fiber Matrix Theory

In an attempt to reconcile the inconsistencies in the pore-slit models described above, Curry and Michel (1980) proposed that there was a diffuse matrix of sulphated proteoglycan molecules at the endothelial surface and in the wide portion of the cleft, as shown in Fig. 1.2(b), and that this matrix provided the primary molecular filter. This fiber matrix could also strongly influence the filtration and permeability properties of the cleft.

In the fiber matrix theory, the hydrodynamic resistance is described by the Carman-Kozeny equation (Sullivan et al., 1942), the diffusive resistance is described by a stochastic model for diffusion within a fibrous network (Ogston et al., 1973) and the sieving properties are approximated by applying the equation proposed by Anderson et al. (1974, 1981), which implies a pseudo-Poiseuillean velocity profile between fibers. Because of its flexibility in choosing the fiber radius and density, this model is able to account for some of the

inconsistencies that can not be explained by the pore-slit model.

The principal drawbacks of the one-dimensional fiber matrix model are: (1) the effect of junction strands, which have been observed in electron microscopic studies, is neglected; (2) the effect of the adjacent plasma membranes (cleft walls) is neglected and the permeability coefficients (L_p, P, σ) are calculated as if the fiber matrix filled an infinite domain. This is true only when the solidity ratio of the fiber matrix is large enough to offer the major transport resistance. Recent rapid freeze etching techniques (Satcher, 1993) and goniometric tilting methods (Shultze and Firth, 1992) have revealed an ordered array of cleft spanning fibers which are oriented perpendicular to the plasmalemma boundaries with a spacing of order 10 nm. This loose structure of cross-bridging fiber elements, where the space between fibers is of the order of half the channel height, does not meet the requirements of infinite medium theory. The predictions of the Carman-Kozeny equation for the filtration coefficient are especially suspect since they grossly underestimate the importance of viscous effects that originate from the interaction of the wall boundary layers with the cross-bridging fibers; and (3) as we shall show later in this section a more rigorous model which takes hydrodynamic and wall-fiber interactions into account shows that the fiber matrix model by itself provides for too great a hydrodynamic resistance if the matrix occupies all of the wide portion of the cleft.

These shortcomings of the simple one-dimensional models depicted in Fig. 1.2 have motivated a series of three-dimensional junction-pore-matrix models of increasing sophistication and accuracy which have the flexibility to examine in detail the permeability properties of a cleft with a bounded fiber array that is either ordered or random and a junction strand whose molecular structure can be varied to describe different junction protein arrangements.

1.2.C Basic Three-Dimensional Model

A basic 3-D model for a cleft with a junction strand and cross-bridging matrix fibers in its wide part was first proposed in Tsay et al. (1989) and applied to the filtration flow problem for predicting hydraulic conductivity L_p. This model is shown in Fig. 1.3 where the junction strand is treated as an impermeable barrier with periodically distributed discrete circular pores of 5.5 nm radius representing the individual missing proteins. In Tsay et al. (1989) intuitive arguments were presented for the matrix components in the wide part of the cleft to be an ordered array of fibers that were aligned perpendicular to the plasmalemma boundaries. The fibers of radius a and channel height 2B were thus arranged in a square 2-D array with periodic spacing 2w and open gap Δ between fibers. In this initial model the fibers were assumed to fill the entire wide portion of the cleft as assumed in the original fiber matrix model of Curry and Michel (1980) sketched in Fig. 1.2(b). The ordering of the fibers was based on Michel's hypothesis (1988) that the positive arginine groups at the ends of the albumin molecule ordered the negatively charged matrix. According to the experimental data (Crone and Levitt, 1984; Clough and Michel, 1988), the height of the wide part of the cleft 2B is much smaller than the depth of the cleft L and the distance between the junctional pores 2D. Thus, a Hele-Shaw model was proposed to examine the effects of a junction strand with its pores on the hydraulic conductivity of capillary interendothelial clefts. One of the important predictions of this 3-D model is that the lateral spreading of streamlines fore and aft of the junction strand greatly reduces the hydrodynamic resistance and shows that L_p is not proportional to the length of the junction breaks as had previously been assumed in the simple 1-D models. In Tsay et al. (1989) the flow through the fiber matrix was described by a two term approximation for the flow around a periodic square array of cylindrical posts in a channel. This two term approximation had been developed by Lee (1969) to describe the flow past the septal posts in lung alveoli. This solution showed marked deviation from the predictions of the Carman-Kozeny

equation for the flow through an infinite medium, but the predictions of the Lee approximation were also suspect since they are valid for the flow past posts whose aspect ratio was close to unity and whose post spacing is larger than the channel height.

In Tsay and Weinbaum (1991), an exact infinite series solution to the full boundary value problem for the doubly periodic fiber array is constructed using the fundamental singularities for a single circular post developed in Lee and Fung (1969) and a quasi-periodic function that is a linear combination of the Weierstrass z function and its derivatives to describe the periodicity conditions for each fiber unit cell. This highly accurate solution for an ordered perpendicular fiber array successfully describes the transition in behavior from the Hele-Shaw potential flow limit to the viscous two-dimensional limiting case for the hydrodynamic interaction between the fibers when their aspect ratio is infinite. This solution also serves to justify the use of the Brinkman approximation in developing expressions for L_p and P for a random fiber array.

The basic 3-D model of Tsay et al. (1989) was extended in Weinbaum et al. (1992) for both the filtration problem and the diffusive permeability problem for predicting P. This more sophisticated 3-D junction-pore-matrix model based on the more rigorous solution obtained in Tsay and Weinbaum (1991) is developed to describe the additional resistance due to an ordered or random matrix in the wide part of the cleft. This model explores the behavior of three different molecular models for the junctional strand discontinuities sketched in Fig. 1.4: (a) a more frequent circular pore of 5.5 nm radius formed by isolated missing junction proteins; (b) a restricted rectangular slit of four to eight missing proteins and 8 nm gap height; and (c) larger more infrequent breaks of four to eight missing proteins with gap height of 22 nm, equal to the width of the wide part of the cleft. These pore structures were chosen based on the electron microscopic observations of Firth et al. (1983) and Bundgaard (1984). The principal predictions

of this model are: (1) infrequent larger breaks are most likely required to account for the measured L_p and the permeability of intermediate size solutes between 0.5 and 2.0 nm radius; (2) these larger breaks must be accompanied by a sieving matrix, but this matrix probably occupies only a small portion of the depth of the cleft and/or its entrance at the luminal surface; (3) neither junctional pore, restricted slit, or fiber matrix models can by themselves satisfy permeability and selectivity data; and (4) one-dimensional models are a poor description of a cleft with infrequent larger breaks since the solute will be confined to small wakelike regions on the downstream side of the junction strand discontinuities and thus not fill the wide part of the cleft.

1.3 THREE NEW APPROACHES

1.3.A Combined Junction-Orifice-Fiber Entrance Layer Model

The prediction in Weinbaum et al. (1992) as to the likely geometry of the large pores in the junction strand has been recently confirmed by the serial section electron microscopic studies of frog mesentery by Adamson and Michel (1993). These serial reconstructions revealed rather long breaks of typically 150 nm width and the same gap height as the wide part of the cleft. The average spacing between these breaks in frog mesentery is 2640 nm. A continuous narrow slit of roughly 2 nm width, which runs along the junctional strand, was also suggested based on goniometric tilting of their sections.

There is evidence indicating that the components of the endothelial cell glycocalyx may correspond to the fiber matrix proposed in the fiber matrix theory (Curry and Michel, 1980). In an earlier study, Adamson (1990), had shown that the enzymatic degradation of the surface layer led to a 2.5 fold increase in L_p. More recent studies indicate that this glycocalyx carries a negative charge and is able to bind cationized ferritin in a thin layer of up to 100 nm thickness

near the endothelial wall (Turner et al., 1983; Adamson and Clough, 1992).

According to these new experimental results, a modified model, which includes a large orifice-like junctional break, a finite region of fiber matrix components at the entrance of the cleft and very small pores or slits in the continuous part of the strand to account for the permeability of small ions, will be developed in Chapter 2.

1.3.B Time Dependent Diffusion Wake Model

The latest time dependent studies of the penetration of lanthanum in the cleft on the abluminal side of the junction strand and confocal microscopic measurements of the spread of sodium fluorescein in the tissue surrounding a perfused microvessel provide additional evidence in support of the small pore system proposed in Chapter 2.

Adamson and Michel (1993) observed the penetration of lanthanum tracers beyond the junction strand approximately 15 seconds after tracer was introduced and concluded that about 6 percent of the cleft length was labeled to the margins of the cleft exit. When these studies were repeated recently by Dr. Adamson in Dr. Curry's lab, a striking difference between the tracer distributions after short (10 sec.) and longer (60 sec.) perfusions was observed. At 10 seconds the frequency of discontinuities in the junctional strand, identified by the penetration of lanthanum beyond the junctional constriction in one or more sections of a serial section sequence, was rare. However, when serial sections of a frog mesenteric capillary were perfused for 60 seconds following the same procedure, lanthanum was observed to fill the cleft beyond the junctional constriction to the abluminal border in every section. Most significantly, all clefts from this vessel exhibited this same pattern of leakage.

These observations strongly suggest that clefts leak along their length but that the threshold for visibility of lanthanum is only exceeded after the diffusional filling of the

surrounding tissue has risen to a level where the concentration at the cleft exit has reached some threshold for detection. Thus, the wakes from the large breaks are labeled at early times because their high flux density allows the local concentration at the cleft exit in the vicinity of these large pores to rise much more rapidly. However, the results of our two-pore model in Chapter 2 predict that the total flux through the infrequent large pores is less than 1/3 of the flux through the small pore system, and that after longer times the latter flux will dominate and fill the entire tissue space surrounding the cleft exit. When this occurs every cleft should be labeled on the abluminal side of the junction strand. The importance of the time dependent labeling of the extravascular space had not previously been considered in the interpretation of electron microscopic labeled tracer studies. In fact, all previous permeability measurements have been based on the assumption that the tissue concentration was low and could be neglected in calculating endothelial permeability.

Strong evidence in support of this hypothesis has been provided by the first confocal microscopic images obtained by Adamson et al. (1995) for the detailed time varying distribution of a low molecular weight fluorescent tracer surrounding an individually perfused microvessel under well controlled conditions in situ. This new experimental technique provides critical information on the distribution of the tracer in a cross-sectional plane, the rate of tracer diffusion into the tissue, and the concentration of the tracer at the capillary wall as it enters the tissue (cleft exit concentration). The results show that the concentration at the cleft exit rose to about 50 percent of the luminal concentration after 58 seconds of perfusion and suggest that the tracer wakes in the lanthanum studies should become visible along the entire length of the junction strand when the cleft exit concentration is close to this value provided the small pore is distributed along the entire length of the junction strand.

These intriguing time dependent results have motivated a much more sophisticated three

region model in Chapter 3 for analyzing the time dependent labeling of the wakes on the abluminal side of the junction strand and the time dependent, spatially varying labeling of a low molecular weight tracer in the tissue space surrounding the vessel. As noted above all previous models have tacitly assumed that in both tracer labeling and permeability studies the concentration at the cleft exit vanishes because the tissue space is treated as an infinite reservoir. The model in Chapter 3 attempts not only to predict the quasi-steady spatial variation of the cleft exit concentration, but also how this concentration changes with time since this will have a profound effect, as discussed above, on the time dependent labeling of the lanthanum wakes that are observed downstream of the large breaks in the junction strand.

1.3.C Time Dependent Convective-Diffusion Wake Model

Another experimental limitation is that the existence of fiber matrix components cannot be directly visualized in the wide part of the cleft. For this reason, two alternative hypotheses have been formulated to describe the size selective structures that determine capillary permeability. One hypothesis proposes that the molecular filter lies within the small discontinuities in the strand of molecules forming the junctional complex between adjacent endothelial cells (Crone and Levitt, 1984). The second hypothesis also proposes that the breaks in the junctional strand determine small solute permeability, but assumes that the primary molecular filter is a fibrous network associated with the cell surface and/or the wide part of the junctional cleft (Curry and Michel, 1980; Michel, 1988). The principal motivation for the development of the two-dimensional convective-diffusion wake model proposed in Chapter 4 of this research is to design experiments that can test for the location of the molecular filter. Whereas the wake of a small electron dense tracer on the abluminal side of the junctional strand provides information about the size and frequency of the discontinuities which can be easily

penetrated by small solutes, the distribution of larger solutes on the luminal side of the junction barrier will help us determine the location of the molecular sieve. If the breaks in the junctional strand are the primary molecular filter, there will be a large change in the tracer concentration and its distribution across the strand at the sites of small solute leakage. On the other hand, if the accumulation of the tracer is near the entrance of the cleft or the tracer concentration decreases with increasing depth into the cleft towards the junctional strand, this would suggest that the fiber matrix is the principal molecular sieve. The models for the ultrafiltration of solute at the junction strand or by matrix components in the wide part of the cleft will examine these possibilities.

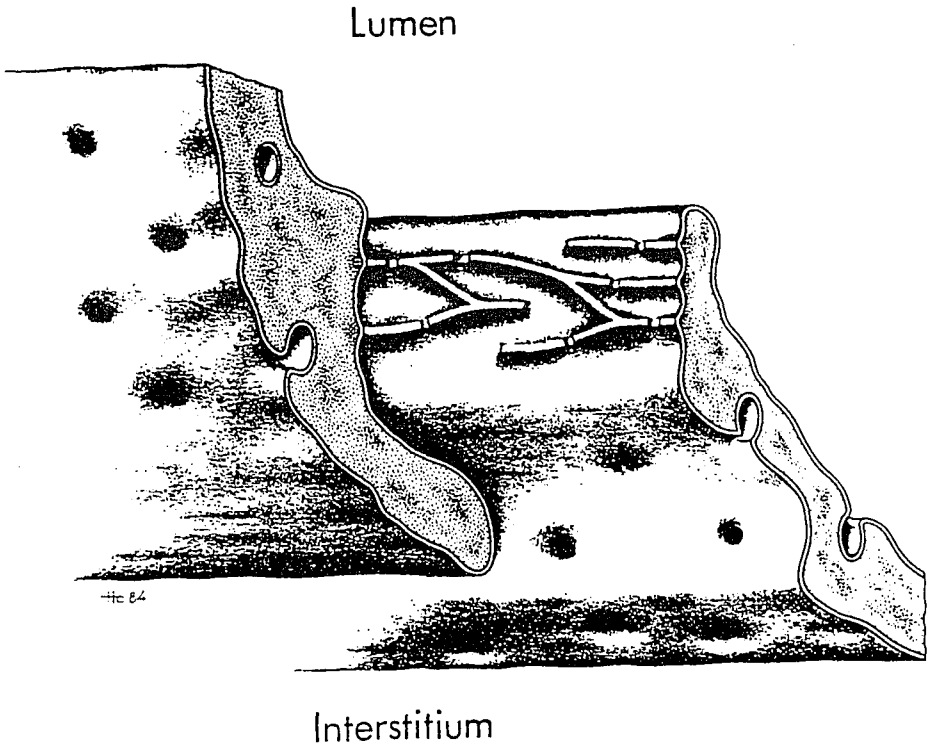

Fig. 1.1 Schematic drawing of the organization of tight junction of capillary endothelium. A small segment of a capillary wall is viewed from the peripapillary space. The junction region on the lateral surface of an endothelial cell is exposed. Passage of hydrophilic solutes through the junctional region can occur by circumvention of lines of contact and via discrete interruptions in the lines. (from Bundgaard, 1984)

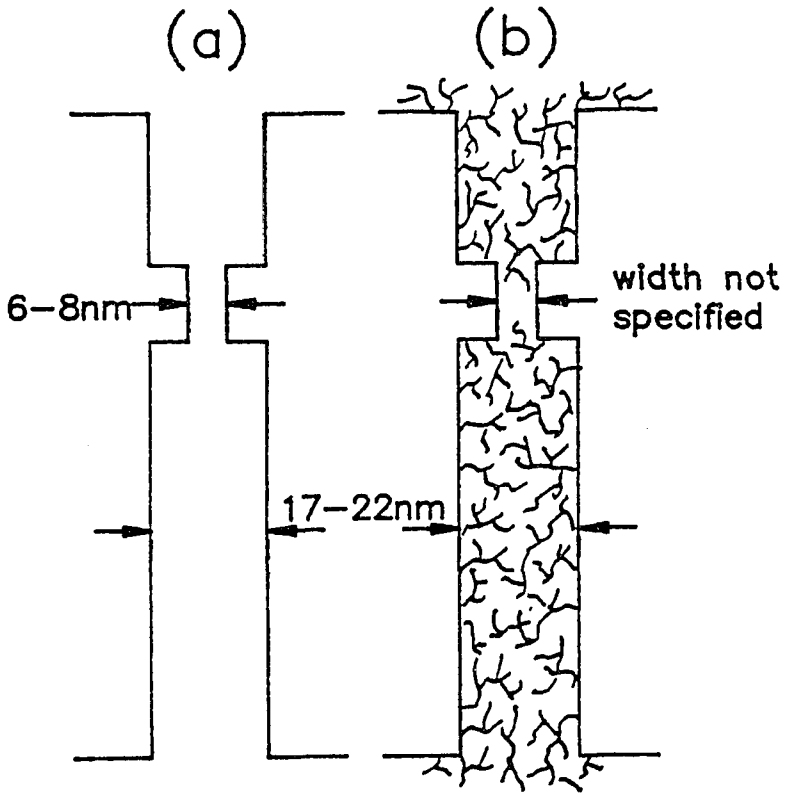

Fig.1.2 Two one-dimensional models of intercellular pathway. **(a)** Pore-slit model. This model proposed that the junctional cleft is 17-22 nm wide except for one or more constrictions. The constriction is assumed to be the main molecular filter and its width, 6-8 nm, is chosen to fit reflection coefficient data. **(b)** Fiber matrix model. The fiber matrix is assumed to be contained in the wide part of the channel and acts as the molecular filter. Both models assume that the permeability is proportional to the fractional length of the tight junction which is effectively open. (from Weinbaum et al., 1992)

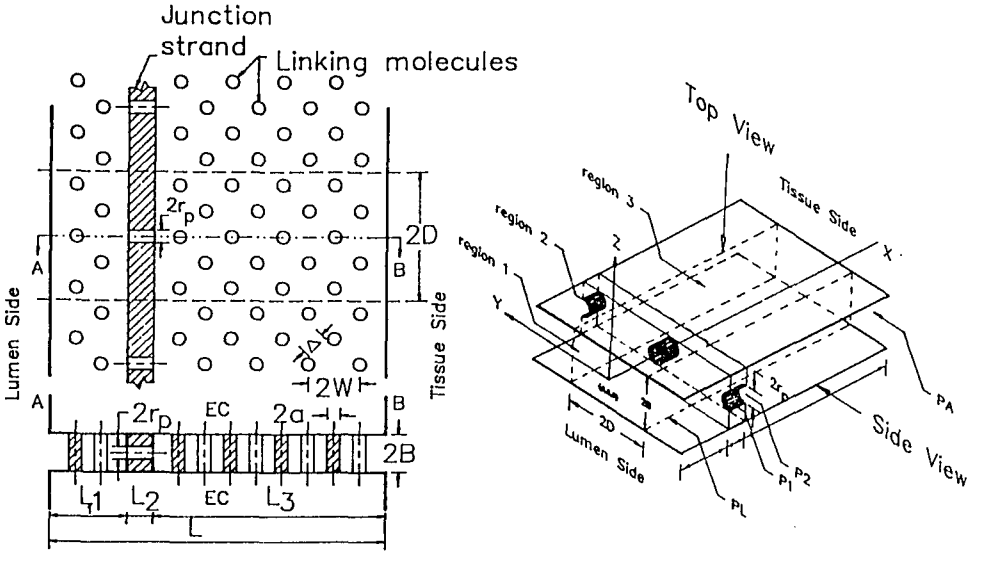

Fig. 1.3 Sketch of the basic three-dimensional junction-pore-matrix model of the intercellular cleft. Junctional strand with periodic pores lies parallel to luminal front. L_2 is the depth of pores in the junctional strand and L_1 and L_3 are the depths between the junctional strand and the luminal and abluminal fronts. Within the wide portion of cleft, cross-bridging fibers are represented by either a periodic square array or a random array of cylindrical posts. The radius of these posts is a and the gap spacing between posts for periodical array is Δ. The distance between two adjacent pores in the junctional strand is 2D. (from Tsay et al., 1989)

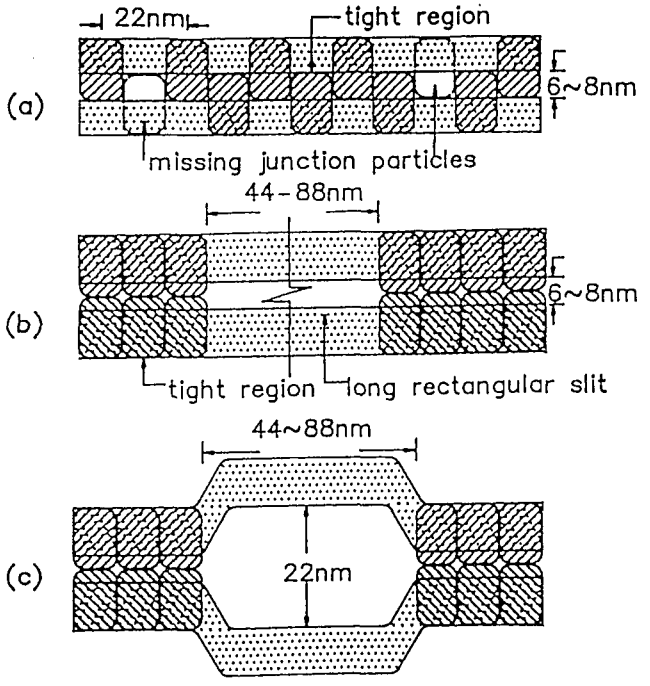

Fig. 1.4 Three schematic diagrams of junction protein arrangements. These protein arrangements correspond to **(a)** small gaps suggested by Bundgaard's (1984) ultrathin sections (the zigzag protein pattern was first proposed in Tsay et al., 1989); **(b)** long rectangular junction pores, similar to those in the one-dimensional constricted channel model; and **(c)** large pores formed by discontinuities of 44-88 nm in the junctional strands. (from Weinbaum et al., 1992)

CHAPTER 2

A COMBINED JUNCTION-ORIFICE-FIBER ENTRANCE LAYER MODEL FOR CAPILLARY PERMEABILITY

2.1 INTRODUCTION

This chapter is a continuing effort based on the previous theoretical work by Tsay et al.(1989) and Weinbaum et al.(1992) to delineate the role of the intercellular junction and matrix structure in the regulation of capillary permeability. There are two major hypotheses describing the molecular filter for capillary permeability. One hypothesis, the pore theory, suggests that small 5.5 nm radius pores or narrow 6-8 nm slits in the junctional strand array are the major molecular filter (Pappenheimer et al., 1951; Perl, 1971; Casley-Smith et al., 1975; Wissig, 1979; Crone and Levitt, 1984; Tsay and Weinbaum, 1989). The other hypothesis, the fiber matrix theory, states that the solute transport is regulated by the size and distribution of a fibrous network in the wide portion of the cleft and at the endothelial surface (Curry and Michel, 1980). Recently, a three-dimensional junction-pore-matrix model has been developed (Weinbaum et al., 1992) to quantitatively evaluate these two hypotheses. In this model, three types of junctional pores, a circular pore of 5.5 nm radius, a rectangular slit of 8 nm gap height and a larger rectangular pore of 22 nm gap height and 22-88 nm width were examined. These pore structures were chosen based on the electron microscopic observations of Bundgaard (1984) and Wissig (1979).

Three important results were obtained from this three dimensional junction-pore-matrix model when applied to the experimental data for single perfused frog mesentery capillaries. First, the results for the three different types of junctional pores indicate that a cleft with a junction strand with any of the pores could not by itself explain all the measured data for the hydraulic conductivity L_p, diffusive permeability P and the reflection coefficient σ. Second, a

cleft filled entirely with a fiber matrix, without a junction strand present, which satisfied the measured value of L_p, substantially underestimated the diffusional resistance for small and intermediate size solutes. Third, a cleft with a junction strand with pores and fibers throughout its wide part, while able to reconcile the data for L_p and small solute permeability, could not satisfy the permeability data for solutes greater than 0.5 nm radius and could not explain the 2.5 fold increase in L_p that occurs when the endothelial cell glycolcalyx at the luminal front is enzymatically removed (Adamson, 1990). For the 5.5 nm radius pore and the 8 nm gap height slit, where the pores are the primary size selective filter, the addition of fibers leads to an even larger disagreement between theoretical predictions and experimental measurements. The junction pore which suggested the best agreement for P is an infrequent 22 nm gap height break whose width is at least a standard transmission section thickness, 40 nm.

The above prediction as to the likely geometry of the large pores in the junction strand has been recently confirmed by the serial section electron microscopic studies of frog mesentery by Adamson and Michel (1993). These serial reconstructions revealed rather long breaks of typically 150 nm width and the same gap height as the wide part of the cleft. These breaks were spaced between 2140 and 4450 nm apart depending on whether conventional thin sections were used, or the breaks were identified by the leakage of the lanthanum tracer extending to the abluminal front. The junction strand pores were thus orifice like discontinuities in a narrow barrier whose depth was the diameter of the individual proteins in the strand. This type of the break is more realistically modeled by the flow through a zero thickness orifice in a channel as proposed in the appendix by Parker et al. in Adamson and Michel (1993), rather than Poiseuille flow in a rectangular channel, the pore model in Weinbaum et al. (1992). The rigorous hydrodynamic theory in Zeng and Weinbaum (1993) indicates that an orifice with the dimensions of the breaks observed in Adamson and Michel (1993) is described well by Hele-

Shaw flow theory. A similar model for the junction strand breaks, to that proposed by Parker et al. is thus used in this study except that the theory is now extended to include diffusion and modified to include finite regions of fiber matrix components in the wide portions of the cleft and very small pores or slits in the continuous part of the strand to account for the permeability of small ions.

There is evidence indicating that the components of the endothelial cell glycocalyx may correspond to the fiber matrix proposed in the fiber matrix theory (Curry and Michel, 1980). Using ruthenium red staining, Luft (1966) first showed that there was a 'fluffy' endothelial coat. More recent studies indicate that this glycocalyx carries a negative charge and is able to bind cationized ferritin in a thin layer of 20 to 30 nm thickness near the endothelial wall (Turner et al., 1983; Adamson and Clough, 1992). There is indirect evidence based on chemical staining that matrix components may fill portions of the wide part of the cleft on the luminal side of the junction complex (Schneeberger and Hamelin, 1984). These authors showed, using an immunoperoxidose method in rat lung, that albumin bound to matrix components in the wide part of the cleft but was absent in the junctional region. The first direct visualization of such components was just reported in the rapid fixation scanning electron micrographs of the arterial endothelial surface by Satcher (1993). In the latter study fine perpendicular fibers could be clearly seen at the entrance to the cleft. In this paper we shall present results for this perpendicular fiber arrangement in either a periodic or random array.

Adamson (1990) studied the fiber matrix hypothesis by comparing normal capillary hydraulic conductivity L_p with L_p measured after partial degradation of the endothelial cell glycocalyx. He observed that L_p increased from 2.0×10^{-7} cm/s/cm H_2O to 4.9×10^{-7} cm/s/cm H_2O after enzymatic degradation, a nearly 2.5 fold increase. This is the only experiment which tries to isolate the hydraulic resistance due to fiber matrix components at the endothelial surface

or in the wide part of the cleft at the luminal front. It will be shown that this behavior is not consistent with the 150 nm wide orifices being the only pathway for water and small ions, but can be explained if a significant fraction of the water and small ions passes through a narrow continuous slit in the junction strand. Evidence for such a structure has been reported in Adamson and Michel (1993).

2.2 MATHEMATICAL MODELLING

2.2.A Model Geometry

A three-dimensional schematic of our idealized model for the interendothelial cleft is shown in Fig. 2.1. The breaks in the junction strand observed by Adamson and Michel (1993) are represented as orifice openings of dimensions 2d x 2b in a zero thickness barrier. The spacing between orifices is 2D and these openings are periodically arranged in the plane of the strand. We shall first consider a basic model without very small pores or slits, in which the junction barrier is impermeable except for the junctional orifices. The junctional orifices connect the two wide portions of the cleft. A fiber layer, which is either an ordered period or random array of perpendicular fibers, is assumed to appear at the lumen front of the cleft and extend to a depth L_f into the wide part of the cleft. This basic model is then modified to include a family of very small pores or slits. A continuous narrow slit of height $2b_s$ is also shown in Fig. 2.1.

For the basic orifice model only pores whose gap height 2b is equal to the gap height 2B of the wide portion of the cleft will be examined. We require that $2b = 2B$ since we assume that this distance is set by the background force balance between the plasma membranes when the slit width $2d >> 2B$. This is consistent with observations in Adamson and Michel (1993). L_2, the thickness of the junction barrier is neglected in the basic model for the orifice flow, but

will be considered later in determining the resistance of the very small pores. L_1 and L_3 are the depths of the cleft on each side of the junction strand. The value of L_1 determines the position of the junctional strand. Results in a previous study (Tsay et al., 1989) indicate that the position of the junction strand has very little effect on the total hydraulic resistance across the junctional cleft; therefore, one chooses $L_1 = L_3$ in all our calculations. L is the total cleft depth and L_f is the depth of the fiber layer at the lumen front.

In the model, periodic and random fiber arrays are examined. For the periodic array, the fibers are represented by a periodic square array of circular cylindrical elements. These fibers are assumed to be oriented perpendicular to the plasmalemma membranes forming the interendothelial channel as observed in the scanning electron micrographs of Satcher (1993). The fiber diameter is 2a and the distance between adjacent fibers is 2W. The open spacing between fibers is Δ. The volume fraction of the fiber matrix is S_f. A hydrodynamic theory for predicting the added hydraulic resistance of this bounded perpendicular fiber array is presented in Tsay and Weinbaum (1991). For the random fiber array we also assume that the fibers form perpendicular cross-bridges across the cleft but are randomly arranged using the stochastic model of Yu and Soong (1975).

2.2.B Hydraulic Conductivity

(a) Large breaks, orifice model

We consider first the basic orifice model with matrix components filling a portion of the wide part of the cleft. Two major simplifications are introduced in the model. First, the thin viscous layers near the edges of the orifice are neglected. In Zeng and Weinbaum (1993) it is shown that there are narrow viscous boundary layers of thickness O(B) near these edges where the velocity adjusts to satisfy no slip boundary conditions. Second, the water flow in the wide

portion of the cleft is analyzed using two-dimensional Hele-Shaw theory which neglects the no slip conditions at the barrier. The justification for this simplification has been discussed in Tsay et al. (1989).

In regions 1 and 3, since the height of the cleft 2B is small compared to both the average distance between the pores 2D and the depths L_1 and L_3, the water flow in the wide part of the cleft can be approximated by a Hele-Shaw flow.

$$u = u_0(1 - \frac{z^2}{B^2}) \tag{2.1}$$

where

$$u_0 = -\frac{B^2}{2\mu}\nabla p \tag{2.2}$$

is the velocity at the center plane z = 0 of the cleft. The pressure field in a Hele-shaw flow satisfies

$$\frac{\partial^2 p}{\partial x^2} + \frac{\partial^2 p}{\partial y^2} = 0 \tag{2.3}$$

The boundary conditions at the boundary plasmalemma membranes of the cleft are no slip

$$u = v = 0 \qquad\qquad at \quad z = \pm B \tag{2.4}$$

where u, v are the x, y components of the fluid velocity **u** and w = 0. The viscous resistance in Hele-Shaw flow originates from the shearing stress at the boundary plasmalemma membranes at z = $\pm$B and the pressure disturbances produced by the vertical boundaries or obstacles in the x, y plane, where no slip boundary conditions cannot be satisfied.

The effect of the hydrodynamic interaction with the cross-bridging fibers in the entrance subregion of the cleft can be treated by replacing the actual fluid viscosity μ by an effective viscosity μ_{eff}. The effective viscosity μ_{eff} is defined by $\nabla<p> = -3\mu_{eff}<U>/B^2$ where $< >$

denotes an average value of a region which is small compared to the depth of the fiber layer L_f. The effective viscosity can be written as μf where f is a hydrodynamic interaction function which depends on the fiber configuration, the fiber volume fraction S_f, and the aspect ratio B/a of the fibers. It was shown in Tsay and Weinbaum (1991), where an exact infinite series solution for the square fiber array in a channel was obtained, that the following solution of the Brinkman equation gives a very good approximation for f when $B/a > 5$.

$$f = \frac{\beta^3}{3(\beta - \tanh\beta)} \tag{2.5}$$

$$\beta = \frac{B}{\sqrt{K_p}}$$

K_p is the Darcy permeability which describes the flow through an infinite matrix which has the same fiber geometry as the interior of the bounded flow under consideration. For a two-dimensional square fiber array, K_p is given by

$$K_p = 0.0572a^2\left(\frac{\Delta}{a}\right)^{2.377} \tag{2.6}$$

which is shown in Tsay and Weinbaum (1991) to be a highly accurate approximation to the exact solution for the two-dimensional periodic array in Sangani and Acrivos (1982).

If the perpendicular fibers observed in Satcher (1993) are arranged in a random array we adopt the approach described in Weinbaum et al. (1992). One retains expression (2.5) for f but uses a Carman-Kozeny approximation for K_p given by

$$K_p = \frac{(1 - S_f)^3}{S_f^2}\cdot\left(\frac{a^2}{4C}\right) \tag{2.7}$$

where C is a fiber density correction factor. When the fibers are circular cylinders

perpendicular to the flow, Happel (1959) used a periodic unit cell model with vanishing shear at the edge of the periodic unit to obtain the following approximate expression for C

$$C = \frac{2(1 - S_f)^3}{S_f}[\ln(\frac{1}{S_f}) - \frac{(1 - S_f^2)}{(1 + S_f^2)}]^{-1} \tag{2.8}$$

The randomness in the distribution of fibers can now be taken into account using a stochastic model developed by Yu and Soong (1975). In this model N fibers are randomly inserted into M subregions and a nonuniform fiber density distribution is generated. Each subregion has a different value of S_f given as

$$S_{fi}^{(k)} = n_i^{(k)}(\frac{M}{N})S_f \tag{2.9}$$

when $n_i^{(k)}$ is the number of fibers in subregion i. By assuming that there is at least one fiber in each subregion, a different value of K_p is obtained for each region. The average value of K_p, which we denote by K_{pr} is calculated as

$$K_{pr} = \sum_{n_1=1}^{N}\sum_{n_2=1}^{N}\cdots\sum_{n_M=1}^{N} K_p^{(k)}\frac{(N - M)!}{\prod_{i=1}^{M}(n_i^{(k)} - 1)!M^{(N-M)}} \tag{2.10}$$

$$n_1 + n_2 + \cdots + n_M = N$$

The mean K_{pr} is used to replace K_p in Eq. 2.5 for a random fiber array.

For mathematical convenience we shall combine the unbounded fiber layer on the lumen surface observed by Turner et al. (1983) and Adamson and Clough (1992) and the cleft-spanning fibers in the wide part of the cleft and treat the entire matrix layer as if it existed in the entrance region of the wide part of the cleft. However, any thickness of surface layer can be converted into an approximate equivalent thickness of matrix inside the cleft by comparing

the Darcy permeability K_p (K_{pr} for random array) of the unbounded fiber matrix with $K_{p,eff}$ ($K_{pr,eff}$ for random array) of the bounded fiber array. In Tsay and Weinbaum (1991), the relationship between K_p and $K_{p,eff}$ was developed as

$$K_{p,eff} = K_p\left(1 - \frac{\tanh(B/\sqrt{K_p})}{B/\sqrt{K_p}}\right)$$

where B is the half height of the cleft. Fig. 2.3(a) describes the ratio of $K_{p,eff}/K_p$ as a function of the solid fraction S_f of fiber matrix for a periodic and a random array. When $S_f = 0.017$ for the periodic array and $S_f = 0.085$ for the random array, both of which are determined by satisfying the measured reflection coefficient 0.9 of the frog mesentery to albumin, $K_{p,eff}/K_p$ are 0.74 and 0.89, respectively. Therefore, the resistance of a 100 nm thick fiber layer at the luminal surface is equal to that of a bounded fiber layer whose depth is 74 nm for a periodic, or 89 nm for a random array inside the cleft.

The large breaks in the junction strand are more accurately modeled as a zero thickness orifice rather than as a pore since $d >> L_2$ and B. Furthermore, for $D >> d$ we can neglect the interaction between adjacent breaks. The solution for a Hele-Shaw flow through a single orifice in a channel of depth L is significantly simplified when the junction barrier is located in the middle of the cleft, $L_1 = L_3$, provided the effective viscosity is uniform in each region. An exact analytic solution is difficult to obtain for a finite fiber layer where $L_f < L_1$, since the pressure will not be uniform along the interface $x = L_f$ between the fiber free and fiber filled regions. A reasonable approximation, however, is to assume an average effective viscosity in region 1, $\mu^{(1)}$, which is an average of μ_{eff} in the fiber layer and μ in the fiber free subregion, which is proportional to the relative depth of each region. Thus,

$$\mu^{(1)} = \frac{\mu_{eff} L_f + (L_1 - L_f)\mu}{L_1} \tag{2.11}$$

Our boundary value problem is, therefore, reduced to flow through two connected regions with different average viscosities $\mu^{(1)}$ and $\mu^{(3)}$ in regions 1 and 3.

One can show, see Appendix, provided that $\mu^{(1)}$ and $\mu^{(3)}$ are constants, although these constants may be different, the pressure at the orifice is a constant given by

$$p(\frac{L}{2}, y) = \frac{\mu^{(3)} p_L + \mu^{(1)} p_A}{\mu^{(1)} + \mu^{(3)}} \qquad 0 \le y \le d \tag{2.12}$$

where p_L is the lumen pressure at x = 0. The boundary condition at the junction barrier, if impermeable, is

$$\frac{\partial p}{\partial x} = 0 \qquad d \le |y| \le \infty, \qquad x = \frac{L}{2} \tag{2.13}$$

The solution of Eq. 2.3 subject to the split boundary conditions (2.12) and (2.13) is not straightforward because they are of mixed type. They are most easily treated using a Schwarz-Christoffel conformal mapping that transforms the region, $0 \le x \le L/2$, $0 \le y \le \infty$, into $0 \le \xi \le \infty$, $0 \le \eta \le \infty$ in the ξ, η plane (Fig. 2.2). The transformation is

$$w = \sin(\pi \frac{z}{L}) \qquad z = x + iy \qquad w = \xi + i\eta \tag{2.14}$$

where the boundaries $x = L/2$, $0 \le y \le \infty$ and $x = 0$ are mapped into the lines $1 \le \xi \le \infty$, $\eta = 0$ and $\xi = 0$. The orifice $x = L/2$, $0 \le y \le d$ is transformed into $1 \le \xi \le \alpha$, $\eta = 0$, and α is given below. The boundary conditions (2.12), (2.13) and $p = p_L$ are unchanged. The solution for the potential pressure field in the ξ, η plane is given in Sneddon (1966). After transforming this solution back to the physical plane, it can be written for region 1 in Fig. 2.1 as

$$p^{(1)}(x, y) = (p_L - p_A)[1 - \theta \int_0^{\infty} u^{-1} A(u) e^{-\eta u} \sin(\xi u) du] + p_A \quad 0 \le x \le \frac{L}{2}, \quad y \ge 0 \quad (2.15)$$

here

$$\xi = \sin(\pi \frac{x}{L}) \cosh(\pi \frac{y}{L}) \qquad \eta = \cos(\pi \frac{x}{L}) \sinh(\pi \frac{y}{L})$$

$$\theta = \frac{\mu^{(1)}}{\mu^{(1)} + \mu^{(3)}}$$

$$A(u) = \frac{2}{K(\alpha^{-1})} \sum_{n=1}^{\infty} (-1)^{n-1} P_{n-1}(\frac{2}{\alpha^2} - 1) J_{2n-1}(\alpha u)$$

$$\alpha = \cosh(\pi \lambda)$$

$$\lambda = \frac{d}{L}$$

where p_L, p_A are the constant pressures at the luminal and the abluminal fronts of the cleft, $\mu^{(i)}$, $i = 1, 3$ are the average viscosities in regions 1 and 3, K is a complete elliptic integral of the first kind, P_{n-1} are Legendre polynomials, J_{2n-1} are Bessel functions of the first kind and the other lengths are shown in Fig. 2.1. This solution differs from that in Parker et al., Appendix in Adamson and Michel (1993), in that the latter solution is only valid for $\mu^{(1)} = \mu^{(3)}$.

A similar solution to (2.15) can be found in region 3

$$p^{(3)}(x, y) = \frac{\mu^{(3)}}{\mu^{(1)}}[p_L - p^{(1)}(1 - \frac{x}{L}, y)] + p_A, \quad \frac{L}{2} \le x \le L, \quad y \ge 0 \qquad (2.16)$$

The final expression for the flow rate through a single orifice is

$$Q = \int_{-B}^{B}\int_{-d}^{d} u_0(L_1, y)(1 - \frac{z^2}{B^2})dydz = \frac{4B^3}{3(\mu^{(1)} + \mu^{(3)})} \frac{K[(1-\alpha^{-2})^{1/2}]}{K(\alpha^{-1})}(p_L - p_A) \qquad (2.17a)$$

where

$$u_0(L_1, y) = [\frac{\pi B^2}{2(\mu^{(1)} + \mu^{(3)})}][\frac{\alpha}{K(\alpha^{-1})}][\frac{1}{\sqrt{\alpha^2 - \cosh^2(\pi \frac{y}{L})}}][\frac{(p_L - p_A)}{L}] \qquad (2.17b)$$

The above expression for Q is easily converted into a filtration coefficient. The number of orifices per unit capillary surface area is $L_{jt}/2D$, where L_{jt} is the total cleft length (total cell perimeter) per unit capillary surface area. Thus, the hydraulic conductivity for the large orifice system is

$$L_{pl} = [\frac{4B^3}{3(\mu^{(1)} + \mu^{(3)})}][\frac{K[(1 - \alpha^{-2})^{-\frac{1}{2}}]}{K(\alpha^{-1})}][\frac{L_{jt}}{2D}] \qquad (2.18)$$

(b) Small junctional pore and slit system

It is difficult to generalize the orifice solution in the previous subsection for the case where the junction barrier is permeable in the regions $d \leq |y| \leq D$, since $\partial p/\partial x$ at $x = L/2$ is unknown and varies as a function of y at the barrier. However, much simpler approximate solutions can be obtained for a continuous narrow slit or distribution of small circular pores in the region where the junction strand is intact. We shall see later in the results that these small pore pathways are required in addition to the large orifice openings just considered if water and small ion permeability are to both agree with the measured values for P and L_p.

We consider first a narrow continuous slit of gap height $2b_s$ which is of the order of 2 nm. This type of continuous slit is suggested by the goniometric tilting of transmission electron micrographic sections of fused junctional regions of frog mesentery capillaries in Adamson and

Michel (1993). In these studies changes in tilt angle of a section nearly always revealed a narrow gap of roughly these dimensions between the outer leaflets of opposing membrane bilayers. Since the fractional length of the orifice type breaks is small, we can neglect their presence for the purpose of estimating the additional contribution to L_p from the narrow slits. We thus consider a second pathway in parallel with the orifice openings that is a simple one-dimensional model in which a narrow slit of height $2b_s$ and depth L_2 connects regions 1 and 3. In this model the contribution of the narrow slit hydraulic conductivity L_{ps} to the total L_p is given by

$$L_{ps} = (R_1 + R_2 + R_3)^{-1} \tag{2.19}$$

where

$$R_i = \frac{3\mu}{2B^3 L_{jt}}[L_i + (f - 1)L_{f,i}] \qquad i = 1, 3 \tag{2.20a}$$

$$R_2 = \frac{3\mu L_2}{2b_s^3 L_{jt}} \tag{2.20b}$$

The ratio of the resistances of the narrow and wide parts of the clefts for this simple one-dimensional model is

$$\frac{R_2}{R_i} = \left(\frac{B}{b_s}\right)^3 \left[\frac{L_2}{L_i + (f - 1)L_{f,i}}\right] \tag{2.21}$$

Numerical results in Weinbaum et al. (1992) show that for a = 0.6 nm and Δ = 7 nm, f is of O(10) in Eq. 2.5. Thus, if L_2 = 10 nm (thickness of junction strand), L_i = 200 nm and B/b_s = 10, R_2/R_i will be at least 5 even if the entire wide part of the cleft is filled with matrix that is a selective sieve for albumin (7 nm diameter). We shall use this calculation to justify the simple model for the very small circular pore that we present next.

A second possibility for a small ion parallel pathway is a small circular pore of radius r_p that might exist between adjacent proteins in the junction strand. This small pore would have a spacing $2D \approx 10$ nm which is approximately the diameter of a single protein. Our results later will show that for $r_p = 1.5$ nm a frequent circular pore of this type can also account for the measured P for small ions in frog mesentery. The hydraulic resistance of this small pore is approximately one order of magnitude greater than the narrow slit whose relative resistance was just estimated. This small pore, if $L_2 = 10$ nm, would have a hydraulic resistance which is at least 50 times the wide part of cleft even if a size selective matrix for albumin was present in the latter part of the cleft. Thus, for this small circular pore $R_2 >> R_i$, $i = 1, 3$, and L_{ps} in (2.19) can be approximated by the simple Poiseuille flow result

$$L_{ps} = \frac{\pi r_p^4}{8\mu L_2}\left(\frac{L_{jt}}{2D}\right) \tag{2.22}$$

The more accurate expression for L_{ps} in Tsay et al. (1989) and Weinbaum et al. (1992), which does take account of the interaction between pores in the wide part of the cleft confirms the simple approximation given by (2.22).

2.2.C Diffusive Permeability

(a) *Large breaks, orifice model*

An equivalent theory to that developed in subsection B(a) for filtration can be developed for solute diffusion through the junction-orifice-matrix geometry shown in Fig. 2.1. This theory closely parallels the solution for the pressure field in the boundary value problem for determining L_p since the concentration C satisfies the same governing equation (2.3) and boundary conditions as for p. One first needs to develop a suitable average expression for the diffusion coefficient which is equivalent to $\mu^{(1)}$ in Eq. 2.11.

The added resistance of a fiber layer at the cleft entrance can be represented by the effective solute diffusivity $D_{i,eff}$ which accounts for both the effect of the plasmalemma membranes and the fiber matrix. Weinbaum et al. (1992) propose the following approximate expression for $D_{i,eff}$ for solutes moving in a confined periodic fiber array

$$D_{i,eff} = D_{iw}(1 + \frac{r_s}{\sqrt{K_p}} + \frac{1}{3}\frac{r_s^2}{K_p})^{-1}[\frac{1 - b_1 S_e}{1 + b_1 S_e}] \qquad (2.23)$$

Here D_{iw} is the restricted diffusivity derived in Ganatos et al. (1980, 1981) for a sphere diffusing in a channel without matrix, but which includes the hydraulic resistance of the plasmalemma boundaries. The first term in parenthesis in (2.23) describes the added resistance of the fiber matrix based on the motion of a sphere in an unbounded Brinkman medium and the second term in parenthesis describes the steric hindrance of the fiber array. Here b_1 is the coefficient of the leading term of the pseudo doubly periodic Weierstrass expansion series that is used to describe the disturbance produced by each fiber for the diffusion problem; $S_e = S_f(1 + r_s/a)^2$ represents the effective fiber solid fraction; r_s is the solute radius; K_p is the Darcy permeability for the periodic unbounded fiber array. For a random array, we replace the second term in parenthesis in (2.23) by the expression in Ogston et al.(1973) for the steric hindrance of a random matrix. In stead of (2.23) we have

$$D_{i,eff} = D_{iw}(1 + \frac{r_s}{\sqrt{K_p}} + \frac{1}{3}\frac{r_s^2}{K_p})^{-1}\exp[-S_f(\frac{2r_s}{a} + \frac{r_s^2}{a^2})] \qquad (2.24)$$

The randomness in the distribution of fibers is taken into account using the same stochastic model described previously for K_p in Eqs. 2.7 and 2.10.

The equivalent expression to Eq. 2.11 for $\mu^{(1)}$ which takes account of the additional diffusional resistance of the fiber layer is

$$D^{(1)} = \frac{L_1 D_{iw} D_{i,eff}}{D_{iw} L_f + (L_1 - L_f) D_{i,eff}} \tag{2.25}$$

and a similar expression can be written for region 3. The final expression for P which corresponds to the solution for L_{pl} in Eq. 2.18 is

$$P_l = \frac{4BD^{(1)}D^{(3)}}{D^{(1)} + D^{(3)}} \frac{K[(1 - \alpha^{-2})^{\frac{1}{2}}]}{K(\alpha^{-1})} \frac{L_{jt}}{2D} \tag{2.26}$$

where α, k, L_{jt}, D have the same definitions as in (2.18).

(b) Small junctional pore and slit system

The simplified one-dimensional model for the additional diffusive permeability P_s for the narrow slit closely parallels that already described in determining L_{ps} for the narrow slit. Instead of Eq. 2.19 one has

$$P_s = (R_{D1} + R_{D2} + R_{D3})^{-1} \tag{2.27}$$

where the R_{Di} are the diffusive resistances in each region. For the narrow slit these are given by

$$R_{Di} = \frac{1}{2BL_{jt}D_{iw}}[L_i + (f_D - 1)L_{fi}] \qquad i = 1, 3 \tag{2.28a}$$

$$R_{D2} = \frac{L_2}{2b_s L_{jt} D^{(2)}} \tag{2.28b}$$

where f_D is equivalent to f in Eq. 2.20a and is given by $D_{iw}/D_{i,eff}$. For small ions $f_D \approx 1$, and $R_2/R_i \approx 0.5$ if $B/b_s = 10$ and $L_i/L_2 = 20$. Thus, in contrast to the filtration problem for the narrow slit, the diffusive resistance of the narrow slit is significantly less than the wide part of the cleft.

One can similarly show that for very small circular pores of radius r_p, $R_2/R_i \approx (4BD/\pi r_p^2)\,(L_2/L_i)$, which is of O(1) for the same values of these geometric parameters cited earlier for filtration. This is a maximum estimate for this ratio which neglects the additional resistance of the fiber matrix in the wide part. The diffusive resistance of the wide part of the cleft can, therefore, not be neglected in calculating P_s for the small circular pores and one cannot use a simple result equivalent to Eq. 2.22 for L_{ps} for determining P_s.

The appropriate diffusion problem for a junction strand barrier with small circular pores of radius r_p and spacing 2D separating regions where there may be a fiber matrix layer of thickness $L_{f,1}$ at the luminal front is defined by the boundary conditions:

$$\frac{\partial C_1}{\partial y} = 0 \qquad y = 0,\ D \tag{2.29a}$$

$$\frac{\partial C_1}{\partial x} = 0 \qquad d \le |y| \le D, \qquad x = L_1 \tag{2.29b}$$

$$\frac{\partial C_1}{\partial x} = Q \qquad |y| < d, \qquad x = L_1 \tag{2.29c}$$

in the fiber free portion of region 1. Here Q is the diffusive flux through the small pores in region 2 and d is an equivalent entrance width in the wide part which is determined by requiring that $4bd = \pi r_p^2$. At the interface with the fiber layer we require

$$C_1 = C_{1f} \qquad x = L_f \tag{2.29d}$$

$$f_D \frac{\partial C_1}{\partial x} = \frac{\partial C_{1f}}{\partial x} \qquad x = L_f \tag{2.29e}$$

Equivalent boundary conditions can be written for region 3. The expression for Q is written in terms of a one-dimensional diffusion equation in which the continuity of concentration and flux at the pore entrance and exit are satisfied. At $x = 0$, $C_{1f} = C_L$ and at $x = L$, $C_3 = C_A$.

The solution to the boundary value problem just summarized leads to the following expressions for R_{D1} and R_{D3} in (2.27)

$$R_{Di} = \frac{1}{2BL_{jt}D_{iw}}[L_i + (f_D - 1)L_{f,i} - \frac{2}{d^2}\sum_{n=1}^{\infty}\frac{F_{n,i}\sin^2(\lambda_n d)}{\lambda_n}], \quad i = 1, 3 \qquad (2.30a)$$

$$F_{n,i} = -\frac{f_D + \coth(\lambda_n L_{f,i})\tanh[\lambda_n(L_i - L_{f,i})]}{f_D\tanh[\lambda_n(L_i - L_{f,i})] + \coth(\lambda_n L_{f,i})}, \qquad i = 1, 3$$

$$\lambda_n = \frac{n\pi}{D}, \qquad n = 1, 2, 3, ...$$

In region 2, the small circular pore, the resistance is

$$R_{D2} = \frac{L_2}{\pi r_p^2}\frac{2D}{L_{jt}}\frac{1}{D^{(2)}} \qquad (2.30b)$$

where $D^{(2)}$ is the restricted diffusion coefficient in the junction pore region. An approximate solution for $D^{(2)}$ for circular pores is given in Curry (1984).

2.3 MODEL PARAMETERS

We shall first identify all the parameters that appear in the model and estimate, where available, the anticipated range of values. The values for the cleft depth, L = 400 nm, and total cleft length per unit area, L_{jt} = 2000 cm/cm^2, are based on the measurements for single perfused vessels in frog mesentery by Clough and Michel (1988). We believe the most reliable measurement of the gap height 2B of the wide part of the cleft is 20 nm, Frokjaer-Jensen (1991). These average values of L, L_{jt} and 2B are close to the mean values reported by other investigators for frog mesentery. The recent study by Adamson and Michel (1993) has provided the first reliable bounds on the size and spacing of the large breaks in the junction

strand of frog mesentery capillaries. Two estimates have been obtained. Conventional serial construction has revealed 3 breaks in a distance of 13.36 μm or a spacing of 4450 nm. Lanthanum labeling of consecutive sections has revealed eleven breaks where the tracer has penetrated to the abluminal side over a distance of 23.56 μm. The average spacing for all 14 breaks is 2640 nm while their average width is 2d = 150 nm. Results will be presented for all three orifice spacings, 2D = 2140, 2640 and 4450 nm.

The largest uncertainties in the model are the measured value of L_p and the structure of the fiber matrix. We will use the measured value of $L_p = 2.0 \times 10^{-7}$ cm/s/cm H_2O in Adamson (1990). This is significantly less than the measured average value $L_p = 5.9 \times 10^{-7}$ cm/s/cm H_2O in Clough and Michel (1988) and 4.0×10^{-7} cm/s/cm H_2O in Adamson and Michel (1993) for frog mesentery. The latter could be overestimates since centerline rather than average values of the velocity were used to calculate L_p. For a Poiseuille profile the average velocity is 1/2 the centerline value and thus if the average value of the velocity were used L_p would be between 2 and 3×10^{-7} cm/s/cm H_2O. We shall present results for L_p which lie in the range 2-4 $\times 10^{-7}$ cm/s/cm H_2O.

As discussed in the introduction there are no definitive studies on the fiber structure of the matrix. In the fiber matrix theory it is generally assumed that the dominant matrix structures determining resistance and the size of the molecular sieve are the GAG side chains of the proteoglycans. It is generally accepted that albumin, 7.0 nm diameter, does not easily pass through this matrix and has a reflection coefficient σ that is close to 0.9, Michel (1988). The sialic acid side chains in the GAG have a radius a = 0.6 nm. If these are ordered in a regular array, as proposed in Michel (1988), then $\Delta \approx 7$ nm for the perpendicular array shown in Fig. 2.1. For these values of a and Δ, the fiber volume fraction S_f is 0.017. For the random fiber array we require that the value of S_f satisfy the measured value for P for albumin. This

corresponds for a random matrix to $S_f = 0.085$ and a reflection coefficient σ of 0.95. The principal unknown for either matrix is the depth of the fiber layer L_f. This depth is determined by requiring the total hydraulic resistance satisfy the measured value of L_p. As discussed earlier and shown in Fig. 2.3(a) any thickness of surface fiber layer can be converted to an equivalent thickness of bounded cleft entrance layer in determining L_f.

2.4 RESULTS

(a) Hydraulic Resistance; Fiber Layer Depth

We shall first present results for the change in L_p with fiber layer thickness L_f for the basic orifice model and later in subsection (d) show how this will be altered if very small pores or a narrow slit are present in the continuous region of the junction strand. The filtration coefficient has been calculated for each of the three orifice spacings obtained from the Adamson and Michel (1993) data in Figs. 2.4(a),(b) for the periodic and random perpendicular fiber arrays in that order. The decrease in L_p as the fractional depth L_f/L of the cleft is increased is shown in this figure. One observes for the periodic perpendicular array in Fig. 2.4(a) that the measured value, $L_p = 2.0 \times 10^{-7}$ cm/s/cm H_2O, is achieved for 2D = 2140 nm when $L_f/L = 0.26$ or $L_f = 104$ nm. At the other extreme, 2D = 4450 nm, one is able to satisfy this measured value of L_p for the periodic fiber array when $L_f = 12$ nm. The corresponding values for the fiber layer depth for the random perpendicular array are $L_f = 23$ nm for 2D = 2140 nm and $L_f = 3$ nm for 2D = 4450 nm.

The first important observation from the above calculations is that the measured value of $L_p = 2.0 \times 10^{-7}$ cm/s/cm H_2O can not be achieved, using the basic orifice model, unless the matrix occupies a relatively small fraction of cleft depth. Since this value of L_p is at the lower end of the measured values for the hydraulic conductivity, the calculated depths of the fiber

layer cited above are close to maximum bounds if the only pathway for water is the 150 nm orifice observed in Adamson and Michel. The depth of the periodic fiber layer is somewhat larger for the same L_p than the random layer. The second important observation is the increase in L_p that results when the fiber layer is enzymatically removed as described in the experiments of Adamson (1990). In interpreting the results of this experiment one assumes that the enzymatic degradation has not also altered the structure of the junction strand. If the junction strand is unchanged, one can attribute the entire increase in L_p to the enzymatic removal of the matrix. This is described in the model by setting $L_f/L = 0$. In this limit Adamson found that L_p increased to 4.9×10^{-7} cm/s/cm H_2O from a control value of 2.0×10^{-7} cm/s/cm H_2O. One concludes from Figs. 2.4(a),(b) that this 2.5 fold increase in L_p can only be achieved when the orifice spacing $2D = 2140$ nm if the entire transendothelial water flux is accounted for by the large orifice-like breaks.

(b) Permeability Intermediate Size Solutes

The solutions for the solute permeability P corresponding to the calculations for L_p in Figs. 2.4(a),(b) for the basic orifice model are shown in Figs. 2.5(a),(b). All the curves in Fig. 2.5 satisfy the measured L_p of 2.0×10^{-7} cm/s/cm H_2O. One observes that the best fit for the intermediate size solutes between 1 and 2 nm radius is obtained for the most distant orifice spacing, $2D = 4450$ nm, for both the periodic and random fiber layers. For this value of 2D the fiber layer at the luminal surface is very thin (12 or 3 nm) and the enzymatic degradation of the fiber layer would lead to only a small increase in L_p. The solution for $2D = 2140$ nm, which did account for the 2.5 fold increase in L_p discussed in subsection (a) is thus not consistent with the curves which provide the best fit for P for intermediate size solutes. All the curves in Figs. 2.5(a),(b) significantly underestimate P for small ions. We shall show in

subsection (d) that both these difficulties can be accounted for if a second pore system for water and small solutes is included.

(c) Varying L_p of the Large Pore System

All the curves in Fig. 2.5 satisfy $L_p = 2.0 \times 10^{-7}$ cm/s/cm H_2O. However, as noted in the section describing choice of parameters, typical values of L_p lie in the range 2-4 x 10^{-7} cm/s/cm H_2O. In addition, if a second pore system does exist in parallel with the large orifice-like breaks, L_p for the orifice pathway (large pore system) by itself could be less than 2.0×10^{-7} cm/s/cm H_2O. The latter possibility might allow for a thicker fiber layer which fills the luminal side of the wide part of the cleft. Both these possibilities are examined in Figs. 2.6(a),(b) where L_p is allowed to vary between 1 and 4 x 10^{-7} cm/s/cm H_2O. In Fig. 2.6(a), a thin fiber layer ($L_f = 20$ nm) is maintained at the luminal surface and L_p is varied by changing the orifice spacing. One observes that the solution for P in which $L_p = 1.0 \times 10^{-7}$ cm/s/cm H_2O provides a remarkably good fit for the intermediate size solutes which is superior to the curves shown in Fig. 2.5(a). In general the smaller the value of L_p associated with the large pore system the better the fit for the intermediate size solutes. The difficulty with this $L_p = 1.0 \times 10^{-7}$ cm/s/cm H_2O solution is that it requires the orifice spacing, $2D = 8080$ nm, be much larger than the observed measurements in Adamson and Michel (1993), where the maximum value was only 4450 nm.

In Fig. 2.6(b) we have repeated the calculation in Fig. 2.6(a), but this time for a thick fiber layer that fills the entire wide part of the cleft on the luminal side of the junction strand. The interesting observation is that we again obtain a best fit for the intermediate size solutes when $L_p = 1.0 \times 10^{-7}$ cm/s/cm H_2O, but this time the orifice spacing is only 2700 nm and thus lies within the range of spacings, 2140 to 4450 nm, observed in the Adamson and Michel's

experiments and very close to their mean value 2640 nm. One also observes that if L_p of the large pore orifice pathway is 2.0 x 10^{-7} cm/s/cm H_2O or greater the orifice spacing will be significantly less than that observed in Adamson and Michel (1993) if $L_f = L_1$. The primary difficulty with the L_p = 1.0 x 10^{-7} cm/s/cm H_2O solution in Fig. 2.6(b) is that it underestimates by an order of magnitude P for small ions. This feature and the fact that L_p for the large pore system is only a half or less of the total L_p suggest that a second small pore parallel pathway is needed. The solutions for the two highest values of L_p are only approximate since the spacing 2D is not large enough to ignore orifice-orifice interaction.

(d) Permeability to Small Ions, Small Pore Pathway

As discussed in the theoretical formulation two alternate small pore pathways have been examined. The first is a small circular pore that might exist between adjacent proteins in an otherwise continuous junction strand and the other is a narrow continuous slit that runs along the entire length of the strand. The latter is suggested by the goniometric tilting experiments in Adamson and Michel (1993). In nearly all regions where the outer membrane leaflets appeared to be fused a very thin slit could be observed with proper tilt angle. The first possibility is examined in Fig. 2.7(a) and the second in Figs. 2.7(b),(c). In Figs. 2.7(a),(b),(c) we have assumed the same large pore structure (2D = 2640 or 4450 nm and 2d = 150 nm) and have required that the total L_p = 2.0 x 10^{-7} cm/s/cm H_2O.

(i) *Small circular pore*

Several different size small circular pores were examined in parallel with the basic large pore orifice pathway. The solution that provided the best overall fit for P for both small ions and intermediate size solutes was a value for r_p of approximately 1.5 nm. This solution is shown

in Fig. 2.7(a). The dotted curve is the contribution to P of just this small circular pore, the dashed curve is the large pore solution by itself and the solid curve is the superposition of the two contributions. The dash-dot curve is the combined solution for the maximum orifice spacing 2D = 4450 nm in Adamson and Michel (1993). The solution for P for the latter spacing provides an even better fit to the experimental data for P than the solution for 2D = 2640 nm. For both cases the filtration coefficient for the large orifice system, L_{pl}, is 1.7 x 10^{-7} cm/s/cm H_2O. This can be achieved when L_f = 95 nm for 2D = 2640 nm and L_f = 26 nm for 2D = 4450 nm. One observes that this type of small pore contributes only insignificantly to filtration, L_{ps} = 0.3 x 10^{-7} cm/s/cm H_2O, since its hydraulic resistance is very large, but greatly enhances small ion permeability. The contribution of this pathway falls off very rapidly with increasing solute size and is negligible for solutes larger than 1 nm radius. For the 2D = 2640 nm and L_f = 95 nm solution the fiber layer constitutes approximately 60 percent of the total resistance, see Fig. 2.4(a), whereas for the 2D = 4450 nm and L_f = 26 nm solution the fiber layer constitutes less than 20 percent of the total cleft resistance. Thus, only the combined small and large pore model for 2D = 2640 nm is also able to explain Adamson's (1990) experiment in which L_p was increased 2.5 fold by the enzymatic degradation of the fiber layer.

The principal problem associated with this combined small and large pore model is that it does not account for the variation in L_p and P that has been observed between individual vessels in the frog mesentery. In general, it has been observed that the variation in L_p roughly parallels changes in small solute permeability. This suggests that a significant fraction of the water and small solutes enter through the same pathway, (Curry, 1979; Michel, 1984). This type of small pore is not consistent with this observation since the contribution to L_p is much smaller than the contribution to P for small ions.

(ii) *Narrow slit pore*

The results for the narrow slit pathway are shown in Fig. 2.7(b) for 2D = 2640 nm. Numerical tests revealed that a nearly optimal fit for solutes less than 1 nm radius could be achieved with a slit height $2b_s$ = 1.5 nm. Results for two different slit depths L_2 are shown, 5.5 and 11 nm. A principal difference between the small circular pore solutions in Fig. 2.7(a) and the slit solutions in Fig. 2.7(b) is that the contribution of L_{ps} to the total L_p is substantially larger for the narrow slit geometry. When L_2 = 5.5 nm the contribution to L_p is comparable to the large pore orifice pathway and L_{pl} is reduced to 1.0 x 10^{-7} cm/s/cm H_2O. This smaller L_{pl} allows for a thicker fiber layer while still maintaining the orifice spacing at 2D = 2640 nm. If this fiber layer were enzymatically removed L_p would increase to 4.4 x 10^{-7} cm/s/cm H_2O. This solution thus also closely predicts the 2.5 fold increase in hydraulic permeability that was observed in Adamson (1990) after enzymatic degradation of the surface glycocalyx. The solution for L_2 = 5.5 nm also provides a somewhat better agreement for intermediate size solutes between 1 and 2 nm radius than the L_2 = 11 nm solution.

In Fig. 2.7(c) we have plotted a second set of solutions for the narrow slit geometry corresponding to the 2D = 4450 nm larger orifice spacing observed in Adamson and Michel (1993). In this case the fiber layer thickness is reduced to L_f = 40 nm to satisfy a total L_p of 2.0 x 10^{-7} cm/s/cm H_2O if L_2 = 11 nm and L_f =96 nm if L_2 = 5.5 nm. This last solution shows a remarkably good agreement with the measured P for all solute sizes and nearly perfectly predicts the break in the solute permeability curve that occurs at 1 nm radius. The difficulty with this solution is that if the fiber matrix were enzymatically removed from the wide part of the cleft, L_p would increase to only 3.3 x 10^{-7} cm/s/cm H_2O and thus somewhat underestimate the 2.5 increase in L_p observed in Adamson (1990) after the fiber layer was enzymatically removed.

2.5 DISCUSSION

The recent experiments of Adamson and Michel (1993) have provided valuable new data on junction strand structure in frog mesentery which have made it feasible to quantitatively evaluate the permeability pathways in the interendothelial cleft in a manner that, heretofore, had not been possible. By providing bounds on the size and frequency of the large breaks in the junction strand these experimental studies have made it possible to realistically assess the contributions to permeability of other structural components such as the thickness of the fiber layer and other alternate pathways for small ion permeability which the large pore system can not account for.

The solutions for the basic orifice model in Fig. 2.4 clearly indicate that neither an ordered or random fiber matrix with the proper reflection coefficient for albumin can exist throughout the wide part of the cleft. This matrix would reduce L_p to significantly less than 1.0 x 10^{-7} cm/s/cm H_2O for the observed frequency of orifice-like breaks, $2140 < 2D < 4450$ nm, observed in Adamson and Michel's experiments. However, within this range of 2D, it is possible to have an ordered matrix with the appropriate selectivity for albumin, which fills the entire luminal side of the wide part of the cleft if L_p of the orifice pathway were reduced to 1.0 x 10^{-7} cm/s/cm H_2O, see solid curve in Fig. 2.6(b). According to Fig. 2.4(a) these fibers would contribute approximately five times the resistance of all remaining structures in the cleft and thus L_p would increase fivefold if this layer were removed by enzymatic degradation. This increase is too large and the present calculations suggest that the thickness of the ordered part of the fiber layer is more likely of the order of 100 nm in frog mesentery, see Fig. 2.4(a), since this value for L_f provides the best agreement with Adamson's (1990) 2.5 fold measured increase in permeability after enzymatic degradation. Matrix could be present in other regions but it would have to be much more diffuse and not ordered. Such a scenario is consistent with a

model in which the albumin orders the fibers in the entrance region of the cleft and this forms a selective network which makes it difficult for albumin to penetrate further. The experiments of Schneeberger and Hamelin (1984) support this picture since staining for albumin was observed in the wide part of the entrance region of the cleft but absent from deeper regions near the junctional complex.

The foregoing estimate of L_f is consistent with the recent studies of Adamson and Clough (1992) on the thickness of endothelial cell glycocalyx in frog mesentery capillaries. These investigators used cationized ferritin as a marker of cell surface glycocalyx and observed that when the vessels were fixed after perfusion with frog plasma, the ferritin penetrated the outer region of the glycocalyx to a depth of 20 to 30 nm and that there was a separation layer of 32 nm thickness between this layer and the membrane surface. The total thickness of the glycocalyx 56 nm is thus somewhat smaller than the 100 nm thickness that we have estimated is necessary to predict the 2.5 fold increase in L_p after enzymatic degradation and thus suggests that the ordered fiber layer also penetrates an equivalent distance into the wide part of the entrance region of the cleft. While our mathematical model is for a perpendicular array of fibers in a channel, it is shown in Tsay and Weinbaum (1991) that the solution is also a reasonable approximation for an unbounded array if the fiber interaction layer thickness at the boundaries K_p is less than B. This condition is well satisfied for $S_f = 0.017$. L_f can therefore be used to estimate the combined thickness of the surface glycocalyx and its continuation into the wide part of the cleft at the luminal front. The inability of ferritin (11 nm dia.) to penetrate beyond the outer region indicates that the matrix is continuous and ordered at the surface and that the deeper regions are an effective filter.

It is clear that the orifice-like breaks in the junction strand can not account for small ion diffusive permeability, even if they are spaced near the low end, 2D = 2140 nm, of Adamson

and Michel's measurements, see Figs. 2.6(a),(b). This provides strong evidence for a second family of small pores. Two alternate hypotheses for this small pore family have been advanced in the present paper, a small circular pore of 1.5 nm radius and a narrow continuous slit of 1.5 nm height. Both pores can account for the permeability of solutes of less than one nm radius, but only the narrow slit can significantly contribute to filtration, compare Figs. 2.7(a),(b),(c). When the filtration coefficient of the narrow slit pathway L_{ps} is approximately 1.0 x 10^{-7} cm/s/cm H_2O, the spacing of the orifice breaks can be sufficiently far apart to both satisfy Adamson and Michel's measurements of 2D and provide very good agreement with the measurements of P for intermediate size solutes. The predicted thicknesses of the fiber layer for the solutions in Fig. 2.7(b) are also consistent with the 2.5 fold increase in hydraulic conductivity that would result from enzymatic degradation of the matrix on the luminal side of the junction strand.

An intriguing feature of the solute permeability curve is the break in slope for solutes less than or greater than approximately one nm radius. The proposed two pore, large orifice-narrow slit, model provides a rational explanation for this behavior that appears to be quantitatively consistent with the large body of data on selectivity, small ion permeability, hydraulic conductivity and permeability of intermediate size solutes for frog mesentery capillaries. An area that requires further examination is the role of the depth of the narrow slit. This depth reflects the number of continuous junction strands that appear in series. A further observation in frog mesentery capillaries is that small ion permeability and hydraulic conductivity appeared to be roughly coupled in different microvessels in Curry (1979); Michel (1984), and increase or decrease in parallel with one another. Figs. 2.7(b),(c) suggest that this increase or decrease may be associated with the average number of continuous junction strands that the water and small ions cross in traversing the cleft. The small circular pore in an

otherwise continuous strand would not qualitatively give this behavior since its contribution to L_p is too small. The narrow slit model, however, can account for a significant water flux and thus yield results that are roughly consistent with this coupled behavior. The depth of a single slit L_2 has been estimated in this study as 5.5 nm or half the width of a junction strand protein. This is a crude guess since the actual structure of the narrow slit region is well beyond the resolution of the electron micrographs of the narrow slit observed in Adamson and Michel (1993).

(a)

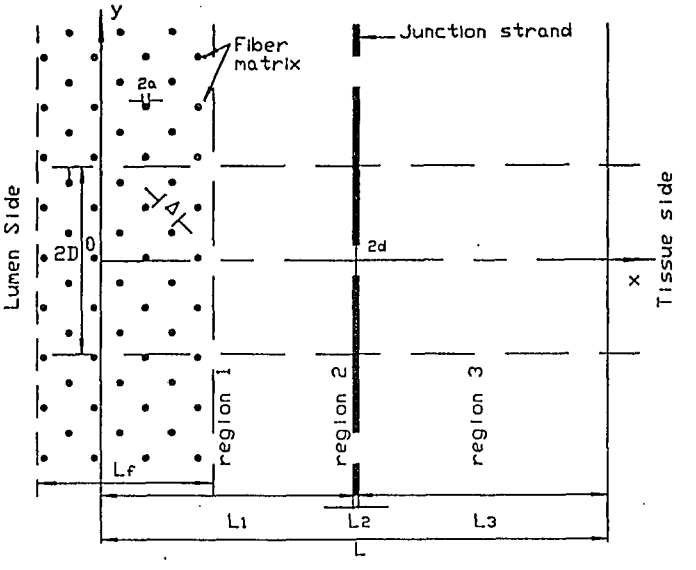

(b)

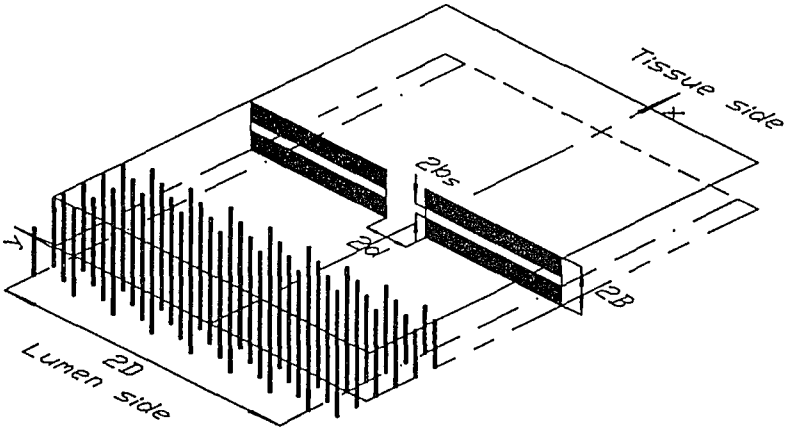

Fig. 2.1 **(a)** Plane view of junction-orifice-matrix entrance layer model of the intercellular cleft. Junction strand with periodic openings lies parallel to the luminal front. L_2 is the depth of pores in junction strand and L_1 and L_3 are depths between junctional strand and luminal and abluminal fronts. The distance between two adjacent breaks in the junctional strand is 2D. At the entrance of the cleft on the luminal side, cross-bridging structures are represented by a periodic square array of cylindrical fibers. The radius of these fibers is a, the gap spacing between fibers is Δ. **(b)** Three-dimensional sketch of single periodic unit of width 2D showing central orifice of height 2b and narrow slit of height $2b_s$ in junction strand.

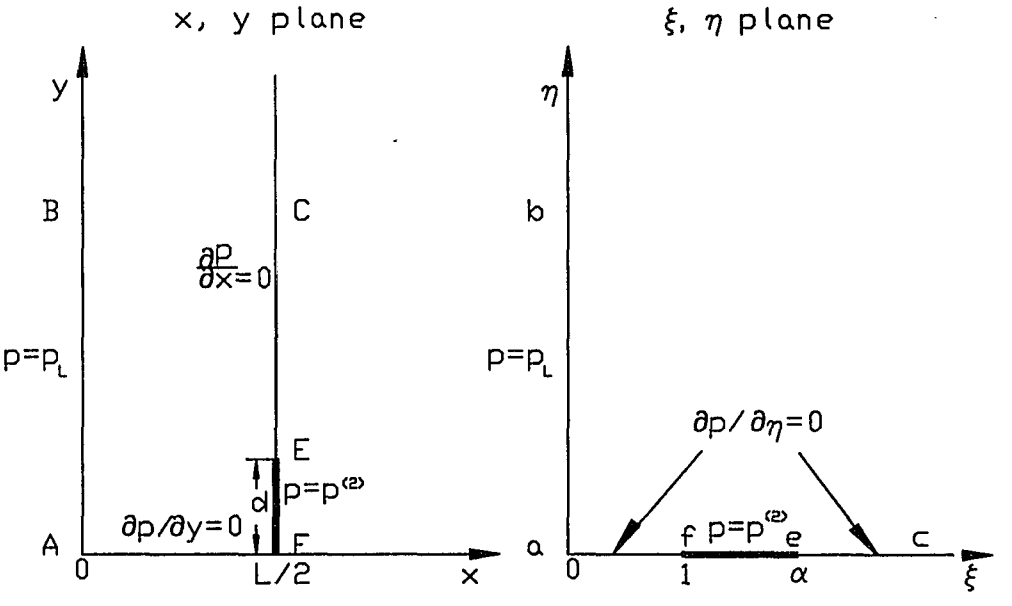

Fig. 2.2 The Schwarz-Christoffel transformation for mapping physical x, y plane into ξ, η plane.

(a)

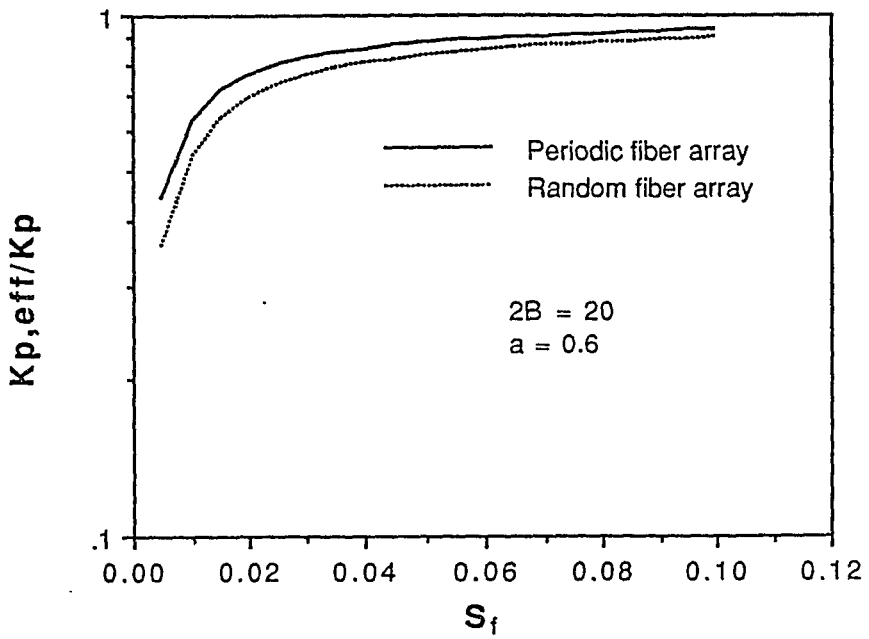

Fig. 2.3(a) The ratio of the effective bounded Darcy permeability $K_{p,eff}$ within the cleft to the unbounded Darcy permeability K_p as a function of solid fraction of the fiber matrix S_f for a periodic array (solid line) and a random array (dotted line). All lengths are in nm.

(b)

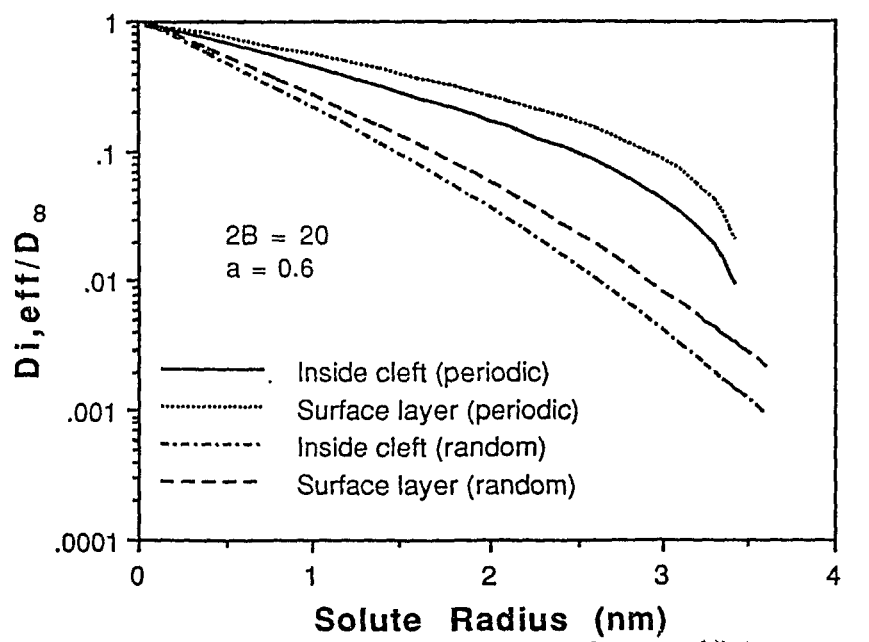

Fig. 2.3(b) The ratio of the effective solute diffusivity $D_{i,eff}$ in the bounded and unbounded fiber filled regions to the free diffusivity D_∞ as a function of solute radius. The solid line and the dotted line are for a periodic array of $S_f = 0.017$. The dashed line and the dash-dot-dash line are for a random array of $S_f = 0.085$. All lengths are in nm.

(a)

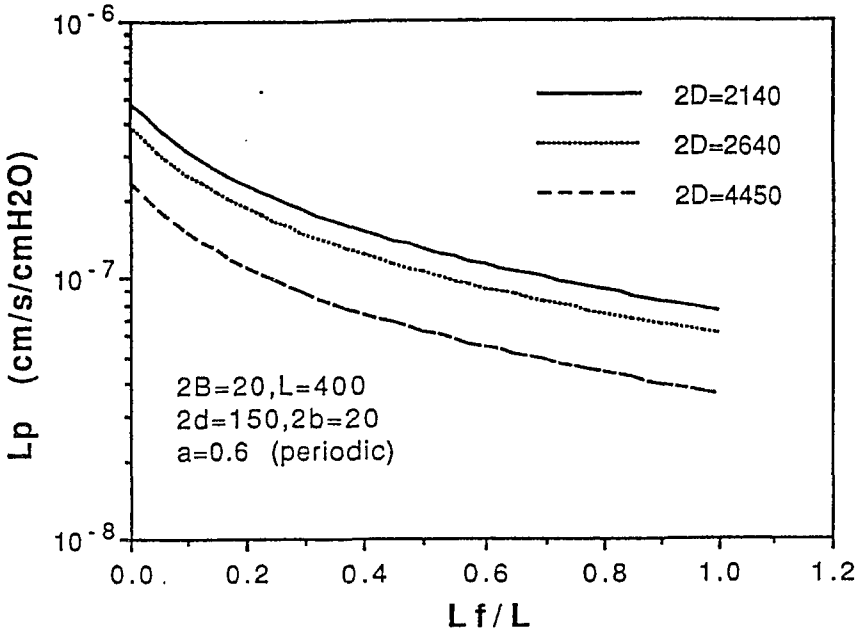

(b)

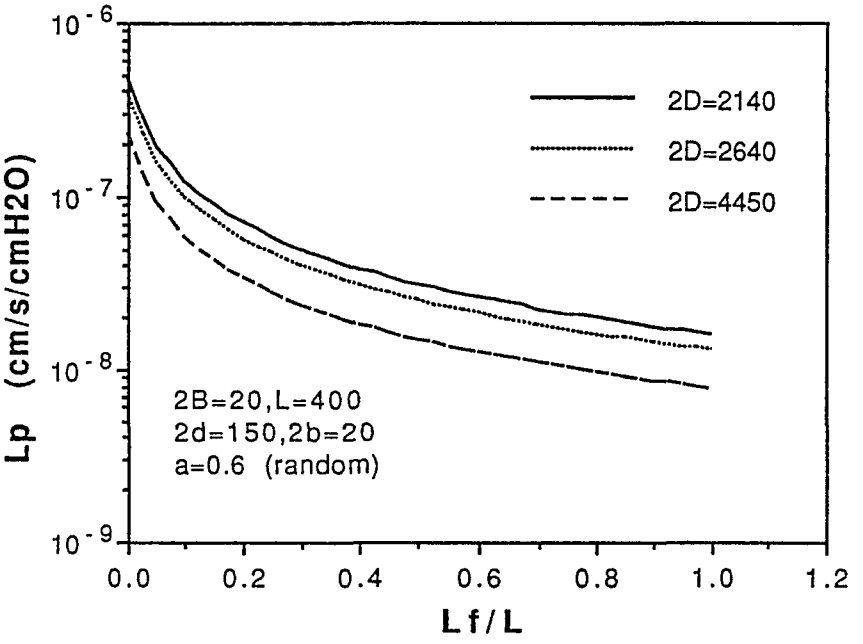

Fig. 2.4 L_p as a function of the dimensionless depth L_f/L of the fiber entrance layer for the minimum (2140 nm), maximum (4450 nm) and average (2640 nm) spacing 2D between adjacent breaks (Adamson and Michel, 1993). **(a)** matrix is periodic with solid fraction $S_f = 0.017$. **(b)** shows results for a random matrix with $S_f = 0.085$. All lengths are in nm. $L_1 = L_3$, $L_2 = 0$.

(a)

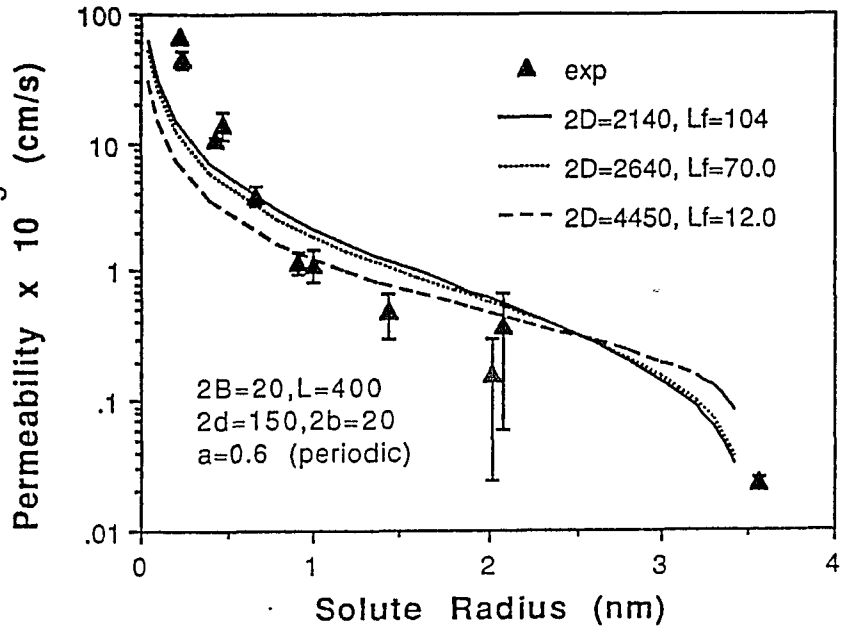

(b)

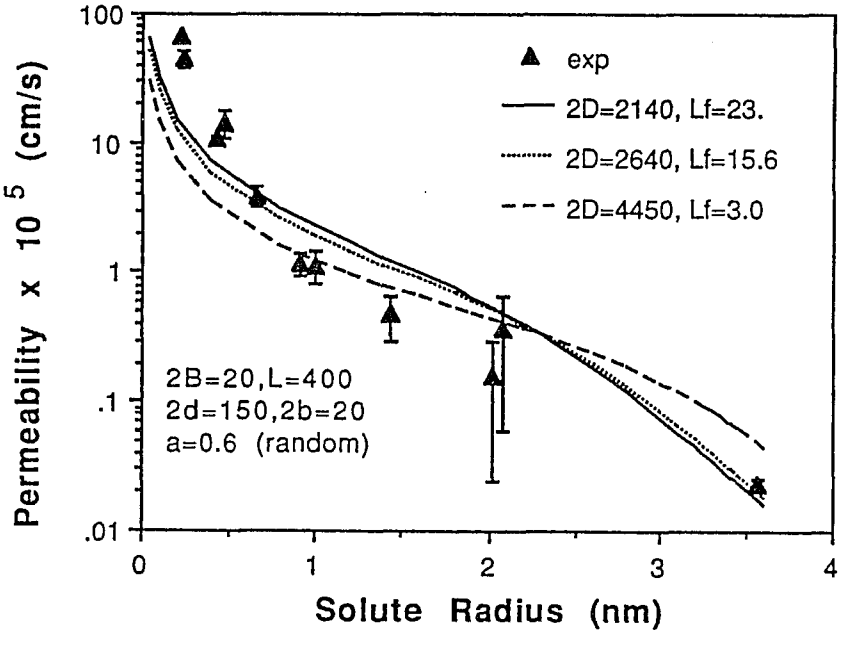

Fig. 2.5 Permeability P as a function of solute radius for same orifice spacings 2D as in Fig. 2.4. The depth of the fiber layer L_f determined by requiring L_p = 2 x 10^{-7} cm/s/cm H_2O. Results for periodic fiber matrix with S_f = 0.017 shown in **(a)** and random matrix with S_f = 0.085 in **(b)**. All lengths are in nm. $L_1 = L_3$, $L_2 = 0$.

(a)

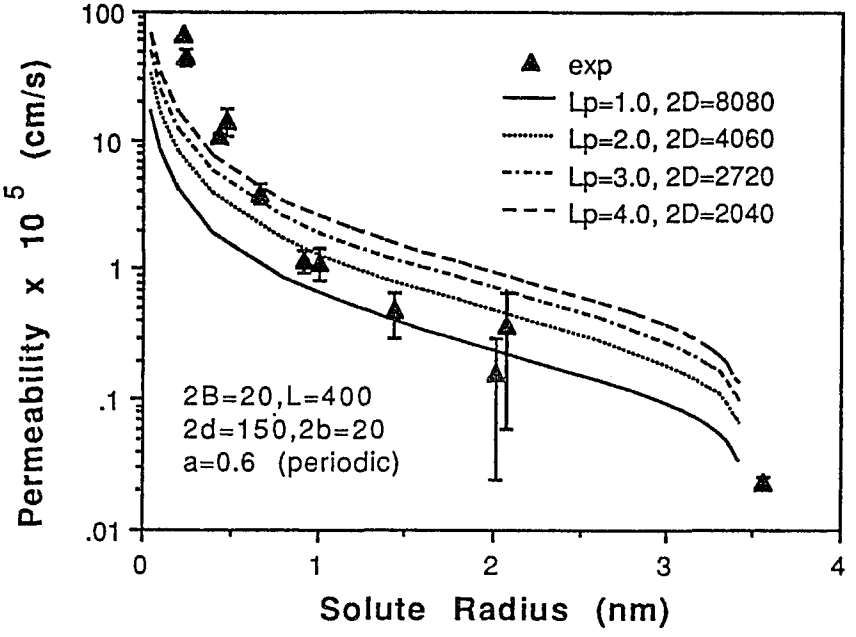

(b)

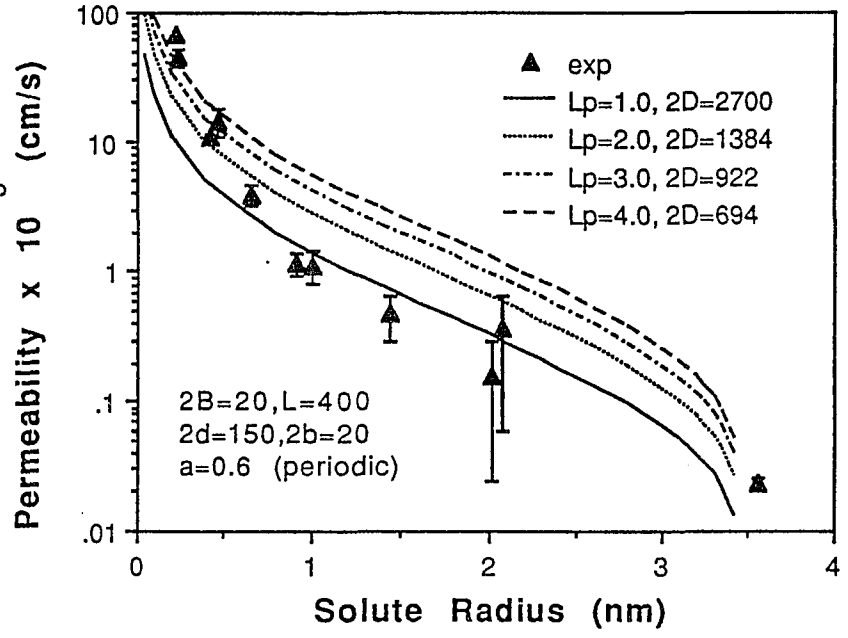

Fig. 2.6 Effect of changing L_p on permeability P for fixed fiber layer thickness L_f. Spacing 2D determined by requiring L_p to satisfy specified values. In **(a)** there is thin fiber entrance layer L_f = 20 nm, whereas in **(b)** matrix fills entire luminal side of cleft $L_f = L_1$. All lengths are in nm and units of L_p = x 10^{-7} cm/s/cm H2O. S_f = 0.017 periodic matrix, $L_1 = L_3$, L_2 = 0.

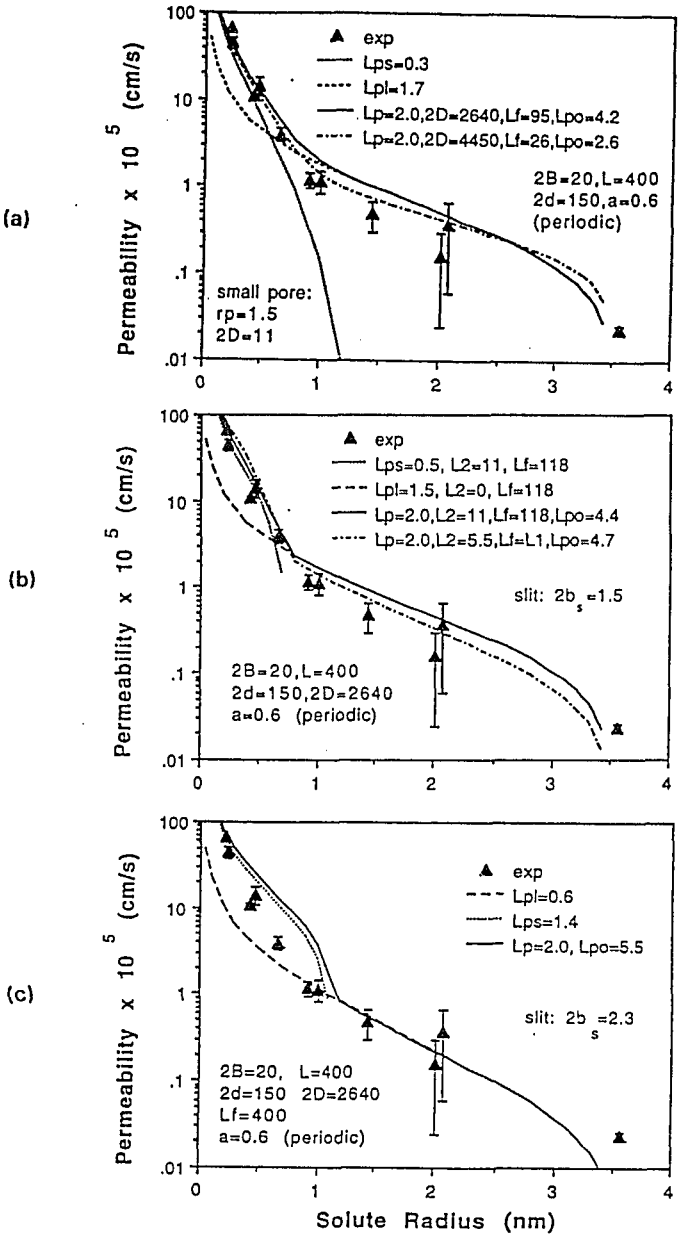

Fig. 2.7 Permeability P as a function of solute radius r_s for a two pore model consisting of large 150 nm x 20 nm orifice pore and (a) small circular pores of radius 1.5 nm spaced 11 nm apart and (b, c) a continuous narrow slit of height 1.5 and 2.3 nm. L_{ps} is the contribution to L_p from small pores and L_{pl} is the contribution from large breaks. The total L_p is fixed at 2.0 x 10^{-7} cm/s/cm H_2O. L_{po} is value without matrix. L_2 = 0 for large 150 nm x 20 nm orifice. **(a)** L_2 = 11 nm for small pore, **(b)** ..., -- and – L_2 = 11 nm for small slit, L_f = 118 nm; -.- L_2 = 5.5 nm for small slit, L_f = L_1, **(c)** L_2 = 11 nm for small slit, L_f = 400 nm. All lengths are in nm and units of L_p = x 10^{-7} cm/s/cm H2O. S_f = 0.017 periodic matrix, L_1 = L_3, L_2 = 0.

CHAPTER 3

A DIFFUSIVE WAKE MODEL FOR TRACER ULTRASTRUCTURE-PERMEABILITY STUDIES IN MICROVESSELS

3.1 INTRODUCTION

Vascular endothelium is the principal barrier to, and regulator of, material exchange between circulating blood and the body tissues. The interendothelial cleft is widely believed to be the principal pathway for water and hydrophilic solute transport through the capillary wall. Direct and indirect evidence summarized in (Weinbaum et al., 1992; Fu et al., 1994) indicates that there are junctional strands with discontinuous leakages and fiber matrix components at the endothelial surface and in the wide portion of the intercellular cleft. This evidence is the basis for the pore, restricted slit and fiber matrix theories which are summarized in (Curry, 1984, 1986; Michel, 1988). The detailed three-dimensional analysis in (Weinbaum et al., 1992) indicates that neither pore, restricted slit nor fiber matrix theory can by itself successfully explain the large body of experimental measurements for the filtration, permeability and selectivity coefficients in isolated capillaries.

Adamson and Michel (1993) in their serial section electron microscopic studies of frog mesentery observed infrequent large breaks of typically 150 nm width and the same gap height as the wide part of the cleft. In contrast to existing views that as much as 80 percent of the cleft might be open to the passage of water and small ions in frog mesentery (Crone, et al., 1984), these serial section studies indicated that only about 6 percent of the junction strand length was discontinuous. These investigators also observed after goniometric tilting, a translucent narrow slit of roughly 2 nm width, which ran along the length of the junctional strand. The patency of this narrow slit is unknown and will be explored in our model. These new experimental results have led Fu et al. (1994) to propose a major modification of the 3-D model in (Weinbaum et

al., 1992). The latter model includes large orifice like junctional breaks, a finite region of fiber matrix components at the entrance of the cleft and at the endothelial surface and very small pores or slits in the continuous part of the strand.

The results of the 3-D model in Fu et al. (1994) strongly suggest that the permeability of small solutes of radius $<$ 1 nm can not be accounted for by the widely spaced 150 nm breaks that have been observed in Adamson and Michel (1993) and that another, previously undetected, family of pores for small solutes very likely exists in parallel with these large interruptions and could account for as much as two thirds of the small solute flux in frog mesentery. It was also predicted that water and small ions followed significantly different pathways with water passing through the large breaks because of their much smaller hydraulic resistance. A fundamental assumption in (Fu et al., 1994) and all previous models of capillary interendothelial clefts is that the tissue can be treated as an infinite reservoir with an effectively vanishing solute concentration at the cleft exit. Predictions of capillary permeability are thus based on a critical simplifying assumption that the transendothelial driving force for solute diffusion is constant over the time course of an experiment.

An important difficulty in reconciling these different views is that the details of the structural features delineating the narrow regions of the junctions lie beyond the resolution of the electron microscope. In this study instead of analyzing the junctional strand pores separately, we have constructed a combined model for the diffusive wake formed by the spreading of small size molecular tracers on the downstream side of the junction strand discontinuities and the 3-D wake in the tissue space surrounding the cleft exit. This approach is analogous to the radar discrimination problem for reentry vehicles where the object itself is hard to visualize, but its wake, a much larger trail of ionized gases, is much easier to detect and analyze.

As noted above, recent serial section studies using lanthanum tracer for short periods

of perfusion (10-15 seconds) demonstrate that only about 6 percent of the junction length is labeled to the abluminal border of the cleft (Adamson and Michel, 1993). In sharp contrast the earlier experiments in (Clough and Michel, 1988) using lanthanum tracer in frog mesentery and random sections revealed that nearly half of all sections labeled to the tissue border. This observation is more consistent with the recent preliminary studies by Dr. Roger Adamson in Dr. Curry's lab (private communication) who observed that after 60 seconds of perfusion lanthanum filled the entire depth of the cleft to the tissue border in nearly all sections.

This marked difference in behavior indicates that the interpretation of tracer studies depends strongly on the experimental design and that both time and the lateral spread of tracer on the tissue side of the junction strand (shape of diffusive wake) must be considered. Furthermore the downstream boundary condition at the cleft exit, which is a critical determinant of the apparent depth of penetration of a lanthanum wake, depends on the time dependent filling of the tissue space and the local concentration and its gradient at the cleft exit. Based on the model in (Fu et al., 1994), one anticipates that regions of the cleft exit near the large 150 nm breaks might label much more rapidly due to the high localized flux density, but that as the overall tissue concentration at the vessel wall rises, all clefts will be labeled. The modeling in this paper provides the basis for the interpretation of these time dependent tracer wake experiments.

An important advance in understanding the role of the tissue space in these tracer experiments is the development of a new experimental technique using the confocal microscope where detailed time dependent tissue concentrations can be measured for the first time in planes perpendicular to the vessel cross-section. The new technique described by Adamson et al. (1995) provides critical information on the distribution of the tracer in a cross-sectional plane, the rate of tracer diffusion into the tissue, and the concentration of the tracer at the capillary

wall as it enters the tissue (cleft exit concentration). Correspondingly, the time dependent models developed in this paper, which are based on the known and postulated structures of the cleft and junction strand, will describe diffusion of small solutes from the cleft exit into the surrounding tissue and the subsequent temporal evolution of these profiles in the tissue space. Comparing these theoretically predicted concentration profiles with the experimentally measured profiles in (Adamson et al., 1995), we can evaluate the proposal, first developed in (Fu et al., 1994), that a second small pore system in parallel with the larger less frequent 150 nm discontinuities, is required to account for the diffusive permeability of solutes of less than 1 nm radius.

3.2 MODEL DESCRIPTION

3.2.1 Model Geometry

Figs. 3.1(a),(b) show the cross-sectional and side views of the junctional leakage sites in a simplified model of our confocal microscopic experiments. A single frog mesenteric capillary of radius $\sim$ 10 μm is perfused with sodium fluorescein. The fluorescent tracers diffuse through the vessel wall into the surrounding tissue space through the large and small pore junctional leakage sites described in Fu et al. (1994) and illustrated in Fig. 3.1. The dimensions of the large breaks (150 nm) and their spacing (2640 nm) are representative of the measurements of frog mesentery microvessels in Adamson and Michel (1993). The dimensions of the small pore, a 1.5 nm slit, are taken from (Fu et al., 1994, as in Chapter 2), where it is shown that a slit height, $2b_s$ = 1.5 nm, provides an optimal fit for small ion permeability. The principal objective of the model is to provide a link between the tracer experiments carried out on the length scale of the electron microscopic observations of the junction strand wakes, region A of Fig. 3.2, and the length scale of the tissue space observed in the confocal microscope

experiments, region C in Fig. 3.2. The transport in regions A and C is coupled by a complicated intermediate region B where there is a time varying, spatially non-uniform cleft exit flux.

Using the idealized geometric model for the cleft described in Fu et al. (1994) (Fig. 2.1 in Chapter 2), we represent the breaks observed by Adamson and Michel (1993) as orifice openings of dimensions 2d x 2b in a zero thickness barrier. The spacing between orifices is 2D and these openings are periodically arranged in the plane of the junction strand. We first consider the basic model for the large junction strand breaks without the small slit pores. In this basic model the junction barrier is impermeable except for the junction orifice. The height 2b of the large orifice breaks is equal to the gap height 2B of the wide portion of the cleft, as observed in (Adamson and Michel, 1993). A fiber layer of thickness L_f is assumed to exist at the luminal front and extend into the entrance region of the cleft as described in (Fu et al., 1994). This basic model will then be modified to include a small continuous slit in the junction strand as shown in Fig. 2.1(b). L_2, the thickness of the junction barrier is neglected in the basic orifice model for the large pore, but this thickness will be considered in determining the resistance of the small slit. L_1 and L_3 are the depths of the cleft on each side of the junction strand. L is the total cleft depth.

3.2.2 Conceptual Model

Fig. 3.2 is a top view of the concentration profiles that one would observe at some instant in time in the mid plane of a cleft and its continuation into the tissue space if one were to traverse the length of the cleft along the plane $z = 0$. The $z = 0$ plane is illustrated in side view in Fig. 3.1(b). The three regions depicted in Fig. 3.2 reveal that there is an inner length scale L (region A, 0.4 μm), which characterizes the development of the detailed concentration

profiles on the abluminal side of junction strand in the cleft proper, an intermediate length scale (region B, 2-5 μm), which characterizes the mixing of the wakes from the individual junction strand discontinuities in the tissue space surrounding the cleft exit, and a far field (region C, 200 μm) where these wakes have merged and the tissue transport satisfies one-dimensional, time dependent diffusion from an integrated source whose total strength varies with time.

The inner cleft region A, is described by the same idealized geometric model for the junction strand and the fiber matrix introduced in (Fu et al., 1994, see Chapter 2) to predict the hydraulic conductivity and the solute permeability of frog mesenteric capillaries. The boundary value problem for the present model on this inner length scale differs fundamentally from Fu et. (1994) in that the concentration at the cleft exit does not vanish, but is an unknown temporally and spatially varying function, C(L,y,t). The Peclet number for the low molecular weight sodium fluorescein and lanthanum tracers used in our experiments is less than 0.2 for all experimental conditions. Therefore, we need to consider only pure diffusion for either the fluorescent or the lanthanum tracer.

The governing equation for unsteady pure diffusion is

$$\frac{\partial C}{\partial t} = D^{(*)}\Delta C \tag{3.1a}$$

where C = C(t,x,y,z) is the concentration distribution and $D^{(*)}$ is the solute diffusivity in region *, the asterisk indicating region A, B or C as the case may be. If we choose T as the typical time scale in the experiment and L^* as the characteristic length of region *, the dimensionless form of Eq. 3.1a is

$$\frac{\partial C}{\partial \bar{t}}\,\epsilon = \bar{\Delta} C \tag{3.1b}$$

where

$$\bar{t} = \frac{t}{T}, \quad \overline{\Delta} = L^{*2}\Delta, \quad \epsilon = \frac{L^{*2}}{D^{(*)}T}$$

The behavior in region * depends on the size of the dimensionless diffusion parameter ϵ. If $\epsilon << 1$, i.e. the time of the experiment $T >> L^{*2}/D^{(*)}$, the characteristic time for the diffusive filling of a region of length scale L^* by solutes of diffusivity $D^{(*)}$, the unsteady term on the left hand side of Eqs. 3.1a,b can be neglected and the behavior in this region is quasi-steady. In this limit the concentration at the boundaries of the region can be treated as slowly varying functions of time, but the instantaneous concentration profiles in the region are the same as for steady state diffusion. If $\epsilon \geq O(1)$, then the unsteady term must be retained since the transient filling of the tissue in region * is important.

For the inner cleft region A, the characteristic length $L^* = 0.4$ μm and $D^{(*)}$ for sodium fluorescein is close to its value in free solution $\sim 5 \times 10^{-6}$ cm^2/s; $L^{*2}/D^{(*)} \sim 3 \times 10^{-4}$ seconds for this inner region. The diffusivity $D^{(*)}$ in the tissue space (regions B and C) is estimated as $\sim 1.5 \times 10^{-6}$ cm^2/s as shown later; therefore, the characteristic times for the intermediate field (region B, 2-5 μm) and far field (region C, 5-200 μm) are $\sim$ 0.2 seconds and $\sim$ 260 seconds, respectively. The shortest time for the measurement of the concentration profiles for our low MW tracers, approximately 5-10 seconds, is thus long compared to the characteristic diffusion times in both regions A and B.

The above asymptotic analysis of the different length scales and characteristic times reveals that important simplifications can be introduced for each region. On the time scale, typically 60 seconds, over which our confocal experiments are performed, the concentration in regions A and B can be treated as time varying, but satisfying a quasi-steady diffusion equation. On the length scale of the intermediate region (2-5 μm) the solute flux at the cleft exit (height 20 nm) can be treated as a time varying line source whose strength varies along its length. The

line integral of this source provides the unknown time dependent source strength for the far field. On the length scale of the far field (200 μm), the intermediate region B can be viewed as the origin $x_t = 0$ (see Fig. 3.2) of a lowest order outer expansion in which the concentration $C_a(t)$ at the outer limits of the intermediate region B serves to define the flux entering the far field. For practical purposes $C_a(t)$ is the wall concentration that we measure in our confocal microscope experiments.

The critical matching condition coupling the local continuity of flux leaving the cleft exit and entering the far field is given by

$$\frac{\partial C}{\partial x} = -\alpha(t)[C(t,L,y) - C_a(t)] \tag{3.2}$$

where $\alpha(t)$ is a time varying function that is determined from the local solution for the line source at the cleft exit in the intermediate region B and $\partial C/\partial x$ is the local gradient at the cleft exit. The results in the following section show that there are large variations in α at early times, $t << 1$ sec., but then α approaches an asymptotic constant that is a function of the gap height 2B and the diffusion coefficient ratio, D_t/D_c, for the diffusivity of the extravascular tissue compared to the cleft. The integral of Eq. 3.2 along $x = L$, the cleft exit plane, provides the time varying source strength for the far field. After a complicated matching procedure which will be described in section 3D, one is able to reduce the overall boundary value problem to an integral equation for the unknown concentration $C_a(t)$, the inner matching condition for the far field and the effective wall concentration in our experiments. Once $C_a(t)$ is determined, the concentration field in all three regions A, B, C can be evaluated from the individual solutions in each region.

3.2.3 Mathematical Formulation

3.2.3A Near field region A; quasi-steady model for the wake of the junction strand

(a) Basic orifice model

For the near field cleft region A, we consider first the basic orifice model with matrix components filling a portion of the wide part of the cleft (see Fig. 2.1(a)). The characteristic time for filling this inner cleft region A of length scale L = 0.4 μm is only 3 x 10^{-4} seconds, as calculated in section 2. Since this is very short compared to the time scale in the experiment, the requirement for neglecting the left hand side of Eqs. 3.1a,b is well satisfied. Furthermore, the channel height 2B << the cleft depths L_1, L_3 on each side of the junction barrier and also the distance between the neighboring breaks 2D. Therefore, the concentration gradients in the x, y directions in the wide part of the cleft will not vary significantly across the cleft height. In view of these two simplifications, the solute concentration in regions 1 and 3 (Fig. 2.1(a)) of near field region A can be approximated by a steady 2-D diffusion equation averaged across the cleft height

$$\Delta C_c^{(i)} = 0 \qquad i = 1, 3 \tag{3.3}$$

where $C_c^{(i)} = C_c^{(i)}(t,x,y)$.

The boundary conditions for solute transport in regions 1 and 3 are

$$C_c^{(1)} = C_L \qquad x = 0, \qquad |y| < D \tag{3.4a}$$

$$\frac{\partial C_c^{(i)}}{\partial y} = 0 \qquad i = 1, 3 \qquad 0 \le x \le L \qquad y = 0, D \tag{3.4b}$$

$$\frac{\partial C_c^{(1)}}{\partial x} = \beta \frac{\partial C_c^{(3)}}{\partial x} \qquad x = L_1 \qquad |y| < d \tag{3.4c}$$

$$C_c^{(1)} = C_c^{(3)} \qquad x = L_1 \qquad |y| < d \tag{3.4d}$$

$$\frac{\partial C_c^{(i)}}{\partial x} = 0 \qquad x = L_1 \qquad d < |y| < D \qquad i = 1, 3 \tag{3.4e}$$

$$\frac{\partial C_c^{(3)}}{\partial x} = -\alpha[C_c^{(3)}(t,L,y) - C_a(t)] \qquad x = L \qquad |y| < D \tag{3.4f}$$

where $\beta = D_c^{(3)}/D_c^{(1)}$ and $D_c^{(1)}$ and $D_c^{(3)}$ are the effective solute diffusivities in regions 1 and 3. The determination of β is discussed below. Boundary condition 3.4a indicates that the solute concentration of the perfusate in the lumen C_L remains constant for the time course of the experiment, while boundary conditions 3.4c,d,e require that junction strand be impermeable except in the pore region $-d < y < d$ for the basic orifice model. Boundary conditions 3.4b are the periodicity and symmetry conditions. Matching condition 3.4f, a restatement of Eq. 3.2, requires that the solute flux entering the tissue at the cleft exit be proportional to the instantaneous local difference between the concentration at the cleft exit and the concentration at the entrance to the far field $C_a(t)$, where $C_a(t)$ is a quasi-steady slowly increasing function of time determined by the coupled boundary value problem linking the three regions. The flux coefficient α is determined from the solution for the intermediate region described in section 3B. As noted earlier, the primary difference between the present boundary value problem in the inner region A and (Fu et al., 1994) is that matching condition 3.4f was replaced by the much simpler boundary condition $C_c^{(3)}(L,y) = 0$. This simplification allowed us to uncouple the boundary value problem for solute diffusing in the cleft from the boundary value problem for the filling of the extravascular tissue space.

In (Fu et al., 1994), the unbounded fiber layer on the lumen surface observed in (Turner et al., 1983; Adamson and Clough, 1992) and the cleft-spanning fibers in the wide part of the cleft were combined and the entire matrix layer were treated as if it existed in the entrance region of the wide part of the cleft. The effective thickness of this combined fiber layer

is given by L_f in Fig. 2.1(a). In (Fu et al., 1994) it is shown that the measured hydraulic conductivity, $L_p = 2 \times 10^{-7}$ cm/s/cm H_2O for the frog mesentery capillary (Adamson, 1990) can be achieved only if a sieving matrix occupies a small fraction of the wide part of the cleft. The model predicts that for the measured average orifice spacing 2D = 2640 nm (Adamson and Michel, 1993), the measured L_p will be achieved if $L_f \sim 100$ nm. The boundary value problem for filtration in Fu et al. (1994) does not suffer from the same limitation as the diffusive problem for small solutes since the hydraulic resistance of the tissue space is small compared to the transendothelial resistance and thus this prediction for L_f is believed to be accurate for the assumed cleft geometry. Following the approach introduced in Chapter 2, we define an average effective diffusivity $D_c^{(1)}$ in region 1, which is an average of $D_{i,eff}$ in the fiber layer and D_{iw} in the fiber free subregion,

$$D_c^{(1)} = \frac{L_1 D_{iw} D_{i,eff}}{D_{iw} L_f + (L_1 - L_f) D_{i,eff}} \tag{3.5}$$

Here D_{iw} is the restricted diffusivity given in (Ganatos et al., 1981) for a sphere diffusing in a channel without matrix, but which includes the hydraulic resistance of the plasmalemma boundaries. $D_{i,eff}$ is given in (Weinbaum et al., 1992). $D_{i,eff}$ accounts for the effect of both the hydraulic resistance and the steric hindrance of the fibers in the matrix entrance layer. Approximation Eq. 3.5, which is the same as Eq. 2.25 in Chapter 2, allows us to reduce the boundary value problem for a cleft with a finite matrix entrance layer from a three region to a two region problem.

It is difficult to solve Eq. 3.3 subject to boundary conditions 3.4a-f, since the split boundary conditions 3.4c,d,e at the junction barrier are of mixed type involving both the concentration and its gradient. For mathematical simplicity, we assume periodically distributed junctional orifices and a functional form for the flux profile at the orifice opening which is a

modified form of the solution obtained in (Fu et al., 1994) for an isolated orifice in a junctional strand. This flux profile is given by

$$\frac{\partial C_c^{(1)}}{\partial x} = \beta \frac{\partial C_c^{(3)}}{\partial x} = \frac{\eta}{\sqrt{\gamma^2 - \cosh^2(\pi \frac{y}{L})}} \qquad x = L_1 \qquad |y| < d \tag{3.6}$$

where

$$\gamma = \cosh(\pi \frac{d}{L})$$

and the unknown coefficient η is determined by satisfying Eq. 3.4d in an integrated average sense over the orifice opening. This very useful approximation will be examined later and shown to be highly accurate.

The solution of the boundary value problem defined by Eqs. 3.3 and 3.4, with matching condition 3.4c given by Eq. 3.6, is for region 1

$$C_c^{(1)}(t, x, y) = C_L + A_0(t)x + \sum_{n=1}^{\infty} A_n(t)\cos(\lambda_n y)\sinh(\lambda_n x) \tag{3.7}$$

and for region 3,

$$C_c^{(3)}(t, x, y) = C_a(t) + B_0(t)(x - L - \frac{1}{\alpha}) + \sum_{n=1}^{\infty} B_n(t)\cos(\lambda_n y)[\exp(-\lambda_n x) + \Omega_n \exp(\lambda_n x)] \tag{3.8}$$

where

$$\lambda_n = \frac{n\pi}{D}$$

$$\Omega_n = \frac{\lambda_n - \alpha}{\lambda_n + \alpha}\exp(-2\lambda_n L)$$

$$A_0(t) = \eta\left[\frac{L}{\pi D\gamma}K((1 - \gamma^{-2})^{\frac{1}{2}})\right] \tag{3.9}$$

$$B_0(t) = \frac{A_0(t)}{\beta}$$

$$A_n(t) = \frac{2\eta}{\lambda_n D\cosh(\lambda_n L_1)}\int_0^d \frac{\cos(\lambda_n y)}{\sqrt{\gamma^2 - \cosh^2(\pi\frac{y}{L})}}dy$$

$$B_n(t) = \frac{2\eta}{\beta\lambda_n D[-\exp(-\lambda_n L_1) + \Omega_n\exp(\lambda_n L_1)]}\int_0^d \frac{\cosh(\lambda_n y)}{\sqrt{\gamma^2 - \cosh^2(\pi\frac{y}{L})}}dy$$

In Eq. 3.9, K is a complete elliptic integral of the first kind. The solution for η obtained by globally satisfying boundary condition 3.4d at the orifice is

$$\eta = \frac{C_a(t) - C_L}{S_0 + \sum_{n=1}^{\infty} S_n\frac{\sin(\lambda_n d)}{\lambda_n d}} \tag{3.10}$$

where

$$S_0 = \frac{L}{\pi D\gamma}K[(1 - \gamma^{-2})^{\frac{1}{2}}][L_1 - \frac{1}{\beta}(L_1 - L - \frac{1}{\alpha})]$$

$$S_n = \frac{2}{\lambda_n D}[\tanh(\lambda_n L_1) - \frac{\exp(-\lambda_n L_1) + \Omega_n \exp(\lambda_n L_1)}{\beta(-\exp(-\lambda_n L_1) + \Omega_n \exp(\lambda_n L_1))}] \int_0^d \frac{\cos(\lambda_n y)}{\sqrt{\gamma^2 - \cosh^2(\pi \frac{y}{L})}} dy \qquad (3.11)$$

(b) Small junctional slit system

If a small pore formed by a continuous narrow slit of gap height $2b_s$ of approximately 1.5 nm is added to the basic orifice openings in the junction strand considered in the previous section, the impermeable boundary condition 3.4e will be changed to

$$\frac{\partial C_c^{(i)}}{\partial x} = \xi^{(i)}[C_c^{(2)}(x = L_1) - C_c^{(2)}(x = L_1 + L_2)], \quad d < |y| < D \quad i = 1, 3 \qquad (3.12)$$

In Eq. 3.12, L_2, the depth of the junction strand in region 2, see Fig. 2.1(a), can not be neglected since there is a significant diffusional resistance across the slit itself. $C_c^{(2)}(t,x)$ are the unknown concentration profiles at the entrance and exit of the small slit opening. It is assumed in Eq. 3.12 that the additional flux through the small slit along the junction strand is proportional to the concentration gradient across the thickness of the junction barrier from its luminal to abluminal sides. The proportionality coefficients $\xi^{(i)}$, i = 1, 3 are determined below using an approximate 1-D model.

The 1.5 nm continuous narrow slit pore is suggested by the goniometric tilting of transmission electron micrographic sections of fused junctional regions of frog mesentery capillaries in (Adamson and Michel, 1993) and the theoretical predictions for small solute permeability in (Fu et al., 1994). Since the fractional length of the large orifice type breaks in frog mesentery is small, < 6 percent, we can neglect their presence for the purpose of estimating the additional contribution to the solute flux through the narrow slit pathway and describe this pathway using a simple one-dimensional model in which a narrow continuous slit

of height $2b_s$ and depth L_2 (region 2) connects regions 1 and 3. The solutions for the concentration distributions in these regions from this 1-D model are

$$C_c^{(i)}(t, x) = a^{(i)}(t)x + b^{(i)}(t) \qquad i = 1, 2, 3 \tag{3.13}$$

where $a^{(i)}(t)$ and $b^{(i)}(t)$, i = 1, 2, 3 are given in Appendix A.

From Eq. 3.13 the concentration difference across the junction strand is proportional to the local concentration difference across the entire cleft from the lumen to the tissue front. The latter difference determines the local instantaneous flux across the cleft in matching condition Eq. 3.4f. From Eqs. 3.4f and 3.13,

$$\begin{aligned} C_c^{(2)}(x=L_1) - C_c^{(2)}(x=L_1+L_2) &= -a^{(2)}(t)L_2 \\ &= \rho[C_L - C_a(t)] \end{aligned} \tag{3.14}$$

where

$$\rho = \frac{L_2}{\frac{D_c^{(2)}}{D_c^{(3)}}\frac{b_s}{b}\left(L+\frac{1}{\alpha}\right) - \left(\frac{D_c^{(2)}}{D_c^{(3)}} - \frac{D_c^{(2)}}{D_c^{(1)}}\right)\frac{b_s}{b}L_1 - \left(\frac{D_c^{(2)}}{D_c^{(3)}}\frac{b_s}{b} - 1\right)L_2}$$

Substituting Eq. 3.14 into Eq. 3.12 gives

$$\frac{\partial C_c^{(i)}}{\partial x} = \zeta^{(i)}[C_L - C_a(t)] \quad x = L_1 \qquad d < |y| < D \qquad i = 1, 3 \tag{3.15}$$

where

$$\zeta^{(i)} = \xi^{(i)}\rho = -\frac{D_c^{(2)}}{D_c^{(i)}}\frac{b_s}{b}\frac{1}{L_2}\rho \qquad i = 1, 3 \tag{3.16}$$

and $D_c^{(i)}$, i = 1, 2, 3 are solute diffusivities in regions 1, 2 and 3. For the basic orifice model without the narrow slit pore, $\zeta^{(i)} = 0$.

Using Eq. 3.15 as the boundary condition at the junction strand instead of Eq. 3.4e,

when the continuous narrow slit is present, one can obtain the solution to the boundary value problem for the two pore model $C^{T(i)}(t,x,y)$, i = 1, 3, using the same procedure as described in the previous section for the basic orifice model. This two pore model solution for regions 1 and 3 is:

$$C_c^{T(1)} = C_L + A_0^T(t)x + \sum_{n=1}^{\infty} A_n^T(t)\cos(\lambda_n y)\sinh(\lambda_n x) \tag{3.17}$$

$$\begin{aligned} C_c^{T(3)} = {} & C_a(t) + B_0^T(t)(x - L - \frac{1}{\alpha}) \\ & + \sum_{n=1}^{\infty} B_n^T(t)\cos(\lambda_n y)[\exp(-\lambda_n x) + \Omega_n \exp(\lambda_n x)] \end{aligned} \tag{3.18}$$

where the coefficients A_n^T and B_n^T are given by

$$A_0^T(t) = \eta^T[\frac{L}{\pi D\gamma}K((1 - \gamma^{-2})^{\frac{1}{2}})] + (1 - \frac{d}{D})\zeta^{(1)}[C_L - C_a(t)]$$

$$A_n^T(t) = \frac{2\eta^T}{\lambda_n D\cosh(\lambda_n L_1)}\int_0^d \frac{\cos(\lambda_n y)}{\sqrt{\gamma^2 - \cosh^2(\pi\frac{y}{L})}}dy - \frac{2\sin(\lambda_n d)}{\lambda_n^2 D\cosh(\lambda_n L_1)}\zeta^{(1)}[C_L - C_a(t)]$$

$$B_0^T(t) = \frac{A_0^T(t)}{\beta} \tag{3.19}$$

$$\begin{aligned} B_n^T(t) = {} & \frac{2\eta^T}{\beta\lambda_n D[-\exp(-\lambda_n L_1) + \Omega_n\exp(\lambda_n L_1)]}\int_0^d \frac{\cosh(\lambda_n y)}{\sqrt{\gamma^2 - \cosh^2(\pi\frac{y}{L})}}dy \\ & - \frac{2\sin(\lambda_n d)}{\lambda_n^2 D[-\exp(-\lambda_n L_1) + \Omega_n\exp(\lambda_n L_1)]}\zeta^{(3)}[C_L - C_a(t)] \end{aligned}$$

Here β, λ_n and Ω_n are the same as in Eqs. 3.4c and 3.9, $\zeta^{(i)}$, i = 1, 3 is in Eq.3.16.

The flux coefficient η, defined in Eq. 3.6, for the two pore model is given by

$$\eta^T = \frac{[C_a(t) - C_L]\Phi}{S_0 + \sum_{n=1}^{\infty} S_n \frac{\sin(\lambda_n d)}{\lambda_n d}} \tag{3.20}$$

where the S_n are defined in Eq. 3.11 and

$$\Phi = 1 + (1 - \frac{d}{D})[L_1 - \frac{1}{\beta}(L_1 - L - \frac{1}{\alpha})]\zeta^{(1)} - \sum_{n=1}^{\infty} \frac{2\sin^2(\lambda_n d)}{\lambda_n^3 dD}[\tanh(\lambda_n L_1) - \frac{\exp(-\lambda_n L_1) + \Omega_n \exp(\lambda_n L_1)}{\beta(-\exp(-\lambda_n L_1) + \Omega_n \exp(\lambda_n L_1))}]\zeta^{(1)} \tag{3.21}$$

One notices from Eq. 3.21 that $\Phi = 1$ when only the large orifice pores are present.

3.2.3B Intermediate field region B; cleft exit jets

(a) Concentration distribution

In this section a simplified model is developed for intermediate region B, the 2-5 μm region shown in Fig. 3.2 surrounding each cleft exit. The distance between the neighboring clefts in Fig. 3.1(a) in the vessel wall is $\sim 10\ \mu$m (Adamson, 1993). The gap height of the wide part of the cleft is merely 20 nm. If one were a tiny observer in the tissue space looking at the cleft exit, one would see a line source of variable strength along the length of the cleft exit in the y direction. On the intermediate length scale of the cylindrical region of 5 μm radius originating at the cleft exit (r = 0, see Fig. 3.2), we can treat the solute flux at the cleft exit as a temporally and spatially varying line source, that spreads radially into a semi-infinite tissue space. Since axial gradients in the y direction near the cleft exit are much smaller than radial gradients, the governing equation, initial and boundary conditions describing the radial decay of this jet are:

$$\frac{\partial C_t}{\partial t} = D_t\left(\frac{\partial^2 C_t}{\partial r^2} + \frac{1}{r}\frac{\partial C_t}{\partial r}\right) \tag{3.22}$$

$$C_t(0, r) = C_a \tag{3.23a}$$

$$D_t\frac{\partial C_t(t, B)}{\partial r}\pi B = q \tag{3.23b}$$

$$C_t(t, \infty) = C_a(t) \tag{3.23c}$$

where q, the source strength per unit length, varies with both y and t. As discussed in section 2, the characteristic diffusion time, L_B^2/D_t, for the intermediate region B in Fig. 3.2 is only about 0.2 seconds. On this time scale, $C_a(t)$ is a slowly changing concentration (quasi-steady function of time) which can be approximated as a constant in the solution of Eq. 3.22 and 3.23a-c. This solution for the concentration distribution in the intermediate region B is obtained by a similarity method which is described in Appendix B. The final result, Eq. 3.B4, is

$$C_t(t, r) = \frac{q}{2\pi D_t}\exp\left(\frac{B^2}{4D_t t}\right)\left[-Ei\left(-\frac{r^2}{4D_t t}\right)\right] + C_a(t) \tag{3.24}$$

where Ei is an exponential integral defined in Appendix B. Since $L_B^2/D_t \sim 0.2$ seconds, and the shortest times in our electron and confocal microscopic experiments are a few seconds, we shall be interested in the behavior of Eq. 3.24 when $t >> L_B^2/D_t$.

(b) Model for α

The solution in Eq. 3.24 for the concentration distribution in the intermediate region B, can be used to determine the exit coefficient α in matching condition Eq. 3.4f.

From Eq. 3.24, the concentration at the cleft exit (r = B) is

$$C_t(t, B) = \frac{q}{2\pi D_t}\exp(\frac{B^2}{4D_t t})[-Ei(-\frac{B^2}{4D_t t})] + C_a(t) \quad (3.25)$$

For B = 10 nm, $D_t \sim 10^{-6}$ cm^2/s and t > 0.2 seconds, $\exp(B^2/4D_t t) \approx 1$ and $B^2/(4D_t t) << 1$. Thus the exponential integral in Eq. 3.25 has the asymptotic form

$$-Ei(-\frac{B^2}{4D_t t}) \approx \ln(\frac{4D_t t}{B^2}) - 0.5772$$

Therefore, for large t, Eq. 3.25 can be written as

$$C_t(t, B) = \frac{q}{4\pi D_t}(\ln\frac{4D_t t}{B^2} - 0.5772) + C_a(t) \quad (3.26)$$

$C_t(t, B)$ in Eq. 3.26 is equal to $C_c^{(3)}(t,L,y)$ in Eq. 3.4f. Eq. 3.26 can, therefore, be rewritten as

$$q(t,y) = \frac{4\pi D_t}{\ln\frac{4D_t t}{B^2} - 0.5772}[C_c^{(3)}(t,L,y) - C_a(t)] \quad (3.27a)$$

However, q can also be expressed in terms of the concentration gradient inside the cleft at the exit plane,

$$q(t,y) = -2BD_c^{(3)}\frac{\partial C_c^{(3)}}{\partial x}\Big|_{x=L} \quad (3.27b)$$

From Eq. 3.4f, Eq. 3.27b can be written as

$$q(t,y) = \alpha 2BD_c^{(3)}[C_c^{(3)}(t,L,y) - C_a(t)] \quad (3.28)$$

Comparing Eqs. 3.27a and 3.28, α is obtained as

$$\alpha = \frac{2\pi}{B}\frac{D_t}{D_c^{(3)}}\frac{1}{\ln\frac{4D_t t}{B^2} - 0.5772} \qquad (3.29)$$

Note that α is a function of time, but we shall show in section 4(c) that for times of interest in our experiment α is nearly constant.

3.2.3C Far field region C; time dependent model for tissue space

As discussed in section 2, the estimated time for the filling of the outer region C in Fig. 3.2 is of the order of 60 seconds. On this time scale the early time behavior ($t < 0.2$ sec.) in the intermediate region B can be neglected. Quasi-steady equilibrium has been achieved in region B and the exit jets from the individual junction orifice discontinuities and adjacent clefts (periodically distributed around the periphery of the vessel wall) have merged with each other and have formed a uniform flux along length of the cleft exit (y direction, see Fig. 3.2). If the mesothelium, top and bottom boundaries of the tissue, is treated as a significantly greater barrier to the solute transport than the tissue space, we can assume that the upper and lower boundaries of the tissue layer are adiabatic and that the far field, defined by region C, can be approximated by one-dimensional, time dependent transport in the x direction. Region C is thus approximated by a 1-D equation averaged across the height of the tissue layer

$$\frac{\partial C_t}{\partial t} = D_t\frac{\partial^2 C_t}{\partial x_t^2} \qquad (3.30)$$

Here $C_t = C_t(t,x_t)$ is the concentration distribution in the tissue space, D_t the solute diffusivity in the tissue and x_t the coordinate in the tissue space in the x direction shown in Fig. 3.2. The origin of the far field coordinate x_t is located at a position which is $\sim 5\ \mu$m from the cleft exit, which on the length scale of the intermediate region B describing the spread of the exit jets at

the cleft exit, is ∞.

The initial and boundary conditions for Eq. 3.30 are

$$C_t(0, x_t) = 0 \tag{3.31a}$$

$$D_t \frac{\partial C_t(t, 0)}{\partial x_t} = Q(t) \tag{3.31b}$$

$$C_t(t, \infty) = 0 \tag{3.31c}$$

Where Q(t) is the total flux integrated along the entire cleft length per unit tissue thickness in the direction of the vessel axis. This integration includes the flux through both the large orifice and narrow slit systems.

If we define $Q_c(t)$ as the integral average flux over y from a single periodic unit of cleft length,

$$Q_c(t) = \frac{\int_{-D}^{D} -D_c^{(3)} \frac{\partial C_c^{T(3)}(t, L, y)}{\partial x} dy}{2D} \tag{3.32}$$

The relationship between the total flux Q(t) and $Q_c(t)$ is

$$Q(t) = \frac{N_c 2B}{H} Q_c(t) \tag{3.33}$$

In Eq. 3.33 N_c is the number of clefts on the half surface of the vessel, see Fig. 3.1, 2B is the width of the cleft and H is the height of the tissue layer.

3.2.3D Procedure for coupling solutions in the cleft and the tissue; solution of integral equation for Q(t)

The concentration at the entrance to the far field in region C, $C_t(t,0)$, is equal to $C_a(t)$

in Eqs. 3.4f and 3.18. To determine $C_a(t)$ we need to develop and solve an integral equation that couples the time varying flux through the clefts Q(t) with the rise in concentration at the vessel wall $C_a(t)$ and the far field more generally. The solutions in regions A and C are linked by the exit coefficient α describing the jet spreading in intermediate region B.

Substituting the solution for $C_c^{T(3)}(t,x,y)$ in Eq. 3.18 into Eq. 3.32, one has

$$Q_c(t) = R[C_L - C_a(t)] \tag{3.34}$$

where R is given by

$$R = \frac{D_c^{(3)}}{\beta}\left[\frac{\Phi\frac{L}{\pi D\gamma}K[(1-\gamma^{-2})^{\frac{1}{2}}]}{S_0 + \sum_{n=1}^{\infty} S_n \frac{\sin(\lambda_n d)}{\lambda_n d}} + (1 - \frac{d}{D})\zeta^{(1)}\right] \tag{3.35}$$

In Eq. 3.35, S_n, $\zeta^{(1)}$ and Φ are given by Eqs. 3.11, 3.16 and 3.21 in that order.

The solution of Eq. 3.30 subject to the boundary and initial conditions (Eq. 3.31a-c) gives the time-dependent concentration distribution in the surrounding tissue in terms of the unknown flux function Q(t). The details of this derivation are given in Appendix C. The final result obtained by taking the inverse Laplace transform of Eq. 3.C4 is

$$C_t(t, x_t) = \frac{1}{\sqrt{\pi D_t}}\int_0^t \frac{Q(\tau)}{\sqrt{t-\tau}}\exp[-\frac{x_t^2}{4D_t(t-\tau)}]d\tau. \tag{3.36}$$

Evaluating Eq. 3.36 at $x_t = 0$ and requiring that $C_a(t) = C_t(t,0)$, one has

$$C_a(t) = \frac{1}{\sqrt{\pi D_t}}\int_0^t \frac{Q(\tau)}{\sqrt{t-\tau}}d\tau \tag{3.37}$$

Substituting Eq. 3.33 and Eq. 3.37 into Eq. 3.34 yields the desired integral equation for the total flux Q(t)

$$Q(t) = \frac{N_c 2B}{H} R[C_L - \frac{1}{\sqrt{\pi D_t}} \int_0^t \frac{Q(\tau)}{\sqrt{t - \tau}} d\tau] \tag{3.38}$$

where R is given by Eq. 3.35.

A closed form analytic solution has been obtained to the integral Eq. 3.38. This solution and the evaluation of the integral in Eq. 3.36 using this expression for Q(t) is given in Appendix D. The final solution for $C_t(t,x_t)$ is obtained from the inverse Laplace transformation of Eq. 3.D2 in Appendix D,

$$C_t(t, x_t) = C_L[-\exp(\frac{\omega}{\sqrt{D_t}} x_t)\exp(\omega^2 t)erfc(\omega\sqrt{t} + \frac{x_t}{\sqrt{4D_t t}}) + erfc(\frac{x_t}{\sqrt{4D_t t}})] \tag{3.39}$$

where

$$\omega = \frac{N_c 2B}{H} \frac{R}{\sqrt{D_t}} \tag{3.40}$$

R is defined in Eq. 3.35.

Eq. 3.39 evaluated at $x_t = 0$ provides the final expression for $C_a(t)$

$$\begin{aligned} C_a(t) &= C_t(t, 0) \\ &= C_L[-\exp(\omega^2 t)erfc(\omega\sqrt{t}) + 1], \end{aligned} \tag{3.41}$$

while the instantaneous total solute flux is obtained from Eqs. 3.33, 3.34 and 3.41.

$$Q(t) = \frac{N_c 2B}{H} R[C_L - C_a(t)] \tag{3.42}$$

Despite the considerable complexity of this three region boundary value problem, one has been able through the use of asymptotic methods to both simplify the formulation and obtain closed form solutions for all the principal results. It would have been a formidable task to solve this,

3-D, three region problem numerically using a large capacity computer.

3.2.4 Parameter Values

(a) Cleft and fiber layer geometry

Figs. 3.1(a),(b) show the idealized model geometry for an individually perfused frog mesentery microvessel. The average measured thickness of the tissue layer is taken to be 25 μm and the characteristic length in the x direction over which measurements are performed is ~200 μm. The average number of the clefts on the half surface of the vessel is 3.5. These values are from Adamson et al. (1995).

The values of the parameters used to describe the cleft geometry are the same as used in (Fu et al., 1994), which were given in Chapter 2 (see Fig. 2.1). These values are: total cleft depth L = 400 nm (Clough and Michel, 1988); height of the cleft 2B = 20 nm (Frokjaer-Jensen, 1991); average large orifice spacing 2D = 2640 nm and opening cross-section, 2b x 2d = 20 x 150 nm (Adamson and Michel, 1993). The predictions in Fu et al. for the width of the small pore or continuous narrow slit along the junction strand that satisfies the measured values for small ion permeability (Curry, 1979) is $2b_s$ = 1.5 nm. Since 2d = 150 nm is much greater than the thickness of the junction strand, L_2 = 11 nm, and the cleft height, 2B = 20 nm, we shall treat the junction strand as a zero thickness barrier for the case of the large orifice. The depth L_2 of the narrow slit is taken as 11 nm. The distance from the lumen front to the junction barrier, L_1, ranges from 100 nm to 250 nm (Adamson and Michel, 1993). We shall present the results for both values of L_1 in our calculations. The depth of the surface fiber layer L_f is ~ 100 nm. This value of L_f was shown in (Fu et al., 1994) to provide very good agreement with the measured values for the hydraulic conductivity L_p and the solute permeability P for small and intermediate size solutes up to albumin (7 nm diameter) in frog

mesenteric capillaries. The predictions of the model in (Fu et al., 1994) also indicate that the fiber layer is ordered and has a gap distance Δ between adjacent fibers of $\sim$ 7 nm, if it is to function as the primary molecular filter. For proteoglycan side chains of 0.6 nm radius, this fiber spacing corresponds to a solid volume fraction $S_f = 0.017$.

(b) Diffusivity in the tissue space D_t

Prior to this study most estimates of D_t have been based on diffusion experiments in which it has been possible to maintain a constant solute flux or a constant concentration at the boundary where the solute is introduced. For this case D_t is easily obtained by matching the solutions for a 1-D time dependent diffusion equation with the tissue concentration profiles. For a constant lumen concentration $Q = C_L P$, where P is the measured solute permeability, and D_t can be simply related to P. In contrast, the confocal microscopic experiments in (Adamson et al., 1995) have shown there is a large rise in $C_a(t)$ as the tissue fills and thus there is a significant decrease in the transendothelial driving force with time. Since Q is now time varying, the measurement of P and the determination of D_t is much more subtle. It requires that we apply the much more complicated solution, Eq. 3.41, for a time varying source, whose strength Q(t), Eq. 3.42, is the solution to the coupled boundary value problem described in this paper.

In view of this difficulty, a novel approach has been developed for determining D_t. As will be shown shortly, the coupling coefficient α, Eq. 3.29, is a sensitive function of the ratio of D_t/D_c describing the relative diffusivities of the solute in the tissue compared to the wide part of the cleft in region 3. The latter for a small solute should be quite close to its free diffusion coefficient. We, therefore, first determine α experimentally by requiring the solution for $C_a(t)$, Eq. 3.41, provide an optimum fit for the rise in the vessel wall concentration with time and then

determine the value of D_t/D_c that corresponds to this experimentally determined using Fig. 3.3. The accuracy of the value of D_t is then confirmed by comparing the predictions of the model for the spread of the tracer with the detailed time dependent concentration profiles measured in the tissue.

(c) Cleft exit coefficient α

The cleft exit coefficient α, Eq. 3.29, is plotted as a function of time in Fig. 3.3 for different values of the ratio D_t/D_c of the diffusivity in the tissue to that in the cleft. As just discussed, D_t could be as small as 0.1 D_c due to the large collagen content of tissue. Results are presented in Fig. 3.3 for D_t/D_c = 1.0, 0.5, 0.3 and 0.1. One notices in Fig. 3.3 that after a rapid initial transient of approximately 0.2 sec. α is almost independent of time. The early time variation of α is due to the rapid initial filling of the tissue space in the intermediate region B. In our model we neglect this initial rapid transient behavior and assume a constant for α given by its asymptotic value at 60 sec.. This estimated asymptotic value of α, will be determined later in Fig. 3.5(a) by curve fitting the measured data for $C_a(t)$.

(d) Solute properties

Two low molecular weight tracers, sodium fluorescein (MW = 367) and lanthanum nitrate (MW = 325) are used in our experiments. The effective hydrodynamic radius of fluorescein is 0.45 nm (Renkin and Curry, 1978) and its free diffusivity in the 25°C aqueous solution is 0.54 x 10^{-5} cm^2/s based on Stokes-Einstein theory (Curry, 1984). The radius of La^{3+} is ~0.2 nm and its free diffusivity is 1.1 x 10^{-5} cm^2/s according to Stokes-Einstein Theory.

3.3 RESULTS

3.3.A Results for Sodium Fluorescein Tracer

Concentration profile at the junction orifice

For mathematical convenience, we introduced a simplifying assumption in Eq. 3.6 for the solute flux profile at the periodically distributed large pore orifices. We assumed that, except for a scaling constant η, this profile was well approximated by the flux profile for an isolated orifice. The continuity of the concentrations on the upstream and the downstream side of the junction orifice in the original boundary condition (Eq. 3.4d) was satisfied only globally over the orifice width. In Fig. 3.4, we examine the accuracy of this assumption by comparing the concentration distributions just above and below the orifice opening for three different locations of the junction barrier, L_1 = 100, 200 and 300 nm. For all three locations, one observes that the concentrations on the upstream and the downstream side of the orifice are almost constant and identical along the entire orifice width except for a narrow region of order 5 nm near the orifice edge. This provides a strong justification as to the suitability of the assumed form of the solute flux profile at the junction orifice in Eq. 3.6.

Rise in tissue concentration and total flux at vessel wall

The average concentration at the vessel wall $C_a(t)$, Eq. 3.41, which is also the concentration at the origin $x_t = 0$ of the far field region C is plotted as a function of time in Fig. 3.5(a) for three different asymptotic values of α, which correspond to the most likely range of D_t/D_c, 0.2, 0.3 and 0.4, see Fig. 3.3. The contribution to the total concentration from the infrequent large pore orifice is less than one half of the total contribution for the entire time course of the experiment for all three values of α or D_t/D_c. The combined two pore model, which has large pores of width 150 nm and a 1.5 nm continuous narrow slit provides the best agreement with the experimental measurements of $C_a(t)$ for all times when α = 0.011 and

D_t/D_c = 0.3. We also examined the effect of the junction strand position, L_1, on $C_a(t)$ and found that there was almost no difference in the predicted $C_a(t)$ curves for L_1 = 100, 200 and 250 nm. The dot-dash-dot curve in Fig. 3.5(a) is the result for L_1 = 100 nm. All the other curves are for L_1 = 200 nm.

In Fig. 3.5(b), we have plotted the time dependent total flux Q(t) into the tissue space from both the large and small pore systems. Fig. 3.5(b) reveals that the flux from the basic large orifice decreases slowly with time as $C_a(t)$ increases. The solute flux through the large pore decreases by roughly 25 percent over the first 100 seconds. In contrast, the flux through the small slit pore decreases rapidly during the first 20 seconds and at 100 sec., is a factor of 2.5 less than its initial value. This indicates that the wake concentration profiles within the cleft change substantially over the first 20 seconds and that the cleft exit concentration profiles change significantly during this time interval.

Time dependent profiles in the surrounding tissue

The predictions of the two pore model, Eq. 3.39, for the time dependent concentration profiles in the tissue space are presented and compared with our confocal experimental measurements in Fig. 3.6. The two pore model predictions provide remarkably good agreement with the measured data for all times: t = 11, 23, 35, 58 seconds. This complete solution obtained by matching the solutions for the inner cleft region A, the intermediate region B and the far field region C takes account of the time variation of the total flux Q(t) from the cleft exit. The accurate prediction for the spread of the solute confirms that the predicted value for D_t obtained from our estimated value of α in Fig. 3.5(a) is reliable.

3.3.B Results for Lanthanum Tracers

Concentration distribution along the cleft exit

Figs. 3.7(a),(b) show the predicted concentration distribution of lanthanum tracer along the length of the cleft exit for t = 5, 10, 20 and 60 seconds for both the large break and the combined large and small pore models for L_1 = 100 and 250 nm. A comparison of the curves for L_1 = 100 and 250 nm shows that if only the large pore is present the location of the junction strand within the cleft has a significant effect on the shape of the cleft exit profiles especially at early times. As one might anticipate when the junction strand is located closer to the tissue side of the cleft there is a narrow region, $|y| < 200$ nm, wherein the cleft exit concentration is locally elevated in the vicinity of the large pore for all times. When L_1 = 100 nm the two-dimensional spread of tracer within the cleft is much broader and the elevation in concentration at the cleft exit opposite the leakage site is much more subdued. In contrast to these predictions for the model in which only the large 150 nm breaks are present, the two pore model predicts cleft exit concentration profiles that are nearly uniform along the length of the cleft exit whose level is nearly independent of the location of the junction strand within the cleft. Numerical results not shown indicate that the average value of C(L, y, t) along the length of the cleft exit is slightly higher than the average wall concentration $C_a(t)$. These predictions assume that the small 1.5 nm slit pore is uniformly distributed along the entire length of the junction strand.

3.4 DISCUSSION

Although the importance of extracellular accumulation of solute as a factor leading to the underestimate of measured solute permeability coefficients in the capillary wall has long been recognized, the importance of the time dependent filling of the extravascular space has not previously been considered in the interpretation of electronmicroscopic studies of cleft structure

using low molecular weight tracers. The interpretation of these studies have been based on the assumption that the presence or absence of tracer deposits indicated the local conductivity of the junctional strand to the test solute in an all-or-none mode and neglected the compounding effects of changing tracer concentration in the tissue which was assumed to be low and time invariant. The underlying premise in these investigations was that the tissue space can be treated as an infinite reservoir of relatively low resistance. The recently published time dependent confocal microscopic images in a plane perpendicular to the axes of individually perfused frog mesentery microvessels using sodium fluorescein as a tracer (Adamson et al., 1995), and the theoretical predictions reported in this study critically challenge this premise. Tracer wall concentrations on the tissue side of the microvessel wall in excess of 50 percent of the lumen concentration are predicted after one minute of perfusion and a particularly rapid rise in cleft exit concentration is found during the first 20 seconds of labeling. These results are similar to those measured using confocal microscopy. If anything, the measured extravascular concentration is a lower bound since the excluded volume for the tracer concentration is not considered in the confocal microscopic measurements. The important implications of these results are discussed below.

In Fu. et al. (1994) a three-dimensional junction orifice-fiber entrance layer model was developed to predict the large body of data for the hydraulic conductivity, solute permeability and selectivity of single perfused frog mesentery microvessels. The results of this model suggested that, to account for small ion permeability and the permeability of solutes of up to 1.5 nm diameter, a population of small pores is required to exist in parallel with the infrequent large 150 nm breaks observed in the serial section studies of Adamson and Michel (1993). An optimum fit of the permeability data could be achieved for a continuous 1.5 nm slit or frequently spaced 1.5 nm radius circular pore. The extension of this model, taking into account

the time dependent filling of the tissue space adds further support to this concept and indicates the types of new physiological experiments which are necessary to systematically test this hypothesis. As observed in Fig. 3.5(a), the large 150 nm breaks in the junctional strand by themselves underpredicted by at least a factor of two the measured rise in extravascular concentration at the vessel wall. Furthermore, this prediction is insensitive to the precise value of the ratio of D_t/D_c used in the model. One observed in Fig. 3.5(a) that the large pore breaks by themselves are unable to explain the rapid filling of the extracellular space for all values of D_t/D_c in the physiological range 0.1 to 0.4. The importance of the time dependent filling of the tissue space in measuring permeability is illustrated further for sodium fluorescein in Fig. 3.5(b). Large variations in solute flux are particularly evident over the first 20 seconds of perfusion. It is, therefore, clear that the tracer concentration in the cleft and tissue are far from time invariant during the first minute of the experiment and this must be taken into account when interpreting tracer data.

The cleft exit concentration profiles in Figs. 3.7(a),(b) provide important new information for interpreting the results of labeled tracer studies using low molecular weight solutes. In contrast to the confocal microscopic measurements which provide an integrated average tissue concentration at the vessel wall, the interendothelial cleft profiles depend critically on the instantaneous local concentration at the cleft exit. If this tracer concentration exceeds the threshold for detection in the electron microscope, then the cleft should label along its entire depth. One observes in Figs. 3.7(a),(b) that there is characteristically different cleft exit profile for a junction strand with only large discontinuous breaks compared with a two pore model in which there is significant leakage along the entire length of the junction strand in addition to the large breaks. In the former case one should observe localized wakes around the large breaks for short labeling periods ($<$ 20 seconds) whose widths depend primarily on the

location (depth) of the break within the cleft. For the two pore model the cleft exit concentration increases nearly uniformly with time and the wake of the large break would be difficult to distinguish from the background if the continuous small slit pore is permeable along its entire length. The two pore model should, therefore, exhibit an all or nothing behavior in which all sections would appear to simultaneously label to the cleft exit as soon as the cleft exit concentration exceeds some threshold value for tracer detection.

These considerations directly apply to studies using low molecular weight electron dense tracers which are being carried out in several laboratories. For example, Adamson and Michel (1993) observed the penetration of lanthanum beyond the junction strand 10-15 seconds after tracer was introduced and concluded that about 6 percent of the cleft length was labeled to the margins of the cleft exit profiles shown in the lower portions of Figs. 3.7(a),(b) where the predictions for a single pore system with large breaks is illustrated. However, earlier experiments by Clough and Michel (1988) using lanthanum ions and the more recent experiments by Roger Adamson (private communication) have indicated a significantly different behavior. The labeling period in the Clough and Michel experiments was not specified and the perfusion could have been as long as 30 seconds. Approximately half of all random sections labeled to the tissue border of the cleft. In Adamson's most recent experiments he observed that after short perfusion (10 seconds) little tracer is observed on the tissue side of the junction strand, whereas after 60 seconds nearly all clefts were labeled beyond the junctional constriction to the abluminal border. The resolution of these results appears to lie in the interpretation of the local tracer concentration not as simply a all-or-none indication of the local penetratibility of the junctional strand by the tracer, but as an indication of the development of the lanthanum tracer diffusion wake behind the strand in both time and space. Furthermore, detection of the tracer as an electron dense deposit appears to occur only when its local concentration exceeds

some threshold concentration. These observations point to the need for new information about the factors determining this threshold.

Another factor which might effect the labeling pattern of the wake on the tissue side of the junction strand is the effective size of the lanthanum ions. Lange's Handbook of Chemistry (1985) reports an effective radius for lanthanum after hydration in aqueous solution of 0.9 nm. This is more than four times the non-hydrated value (0.2 nm) used in the calculations in this paper. If the hydrated value were used, we predict that the lanthanum would not easily penetrate the small pore population. This behavior is contrary to the experimental observations and the predictions shown in Figs. 3.7(a),(b). Nevertheless studies using probes with a range of sizes may be needed to appropriately interpret the time dependent tracer changes in terms of the ultrastructure of the junctional strand between adjacent endothelial cells. An extension of the approach to intermediate sized solutes and macromolecule may also provide new ways to investigate transcapillary pathways for these solutes.

The present model also provides improvement in the methods to estimate both permeability coefficients and tissue diffusion coefficients. It should be possible to devise a method to measure solute permeability coefficients taking into account the time averaged concentration difference across the microvessel wall which is significantly less than the instantaneous time varying concentration observed in the confocal microscopic experiments of Adamson et al. (1995). This problem has limited the application of optical methods to measure small ion and solute permeability coefficients. These were measured previously using an osmotic transient method to estimate the transcapillary concentration difference (Curry, 1979). A simpler version of the present theoretical model is currently being devised to account for the apparent change in permeability with time that results from the decreasing transvascular driving force for the solute.

The theoretical model has also provided a novel new approach for predicting tissue diffusivity for fluorescent solutes. Frog mesentery has a large collagen content and thus the solute diffusivity is significantly less than the free diffusion coefficient, but difficult to measure by traditional methods because of its thin two-dimensional geometry. If the geometry of the tissue layer is known, the time dependent increase in extravascular vessel wall concentration $C_a(t)$ provides a means of determining D_t if the time dependent source strength can be predicted by the theoretical model. The only unknown in the model is D_t/D_c and as shown in Fig. 3.5(a) this ratio can be determined by requiring an optimal fit of the measured data for $C_a(t)$. The ability of the predicted value of D_t to predict the slope of the concentration profiles in the tissue, as shown in Fig. 3.6, provides an independent check on the accuracy of the predicted value for D_t and the internal consistency of the wall to tissue transport model described herein.

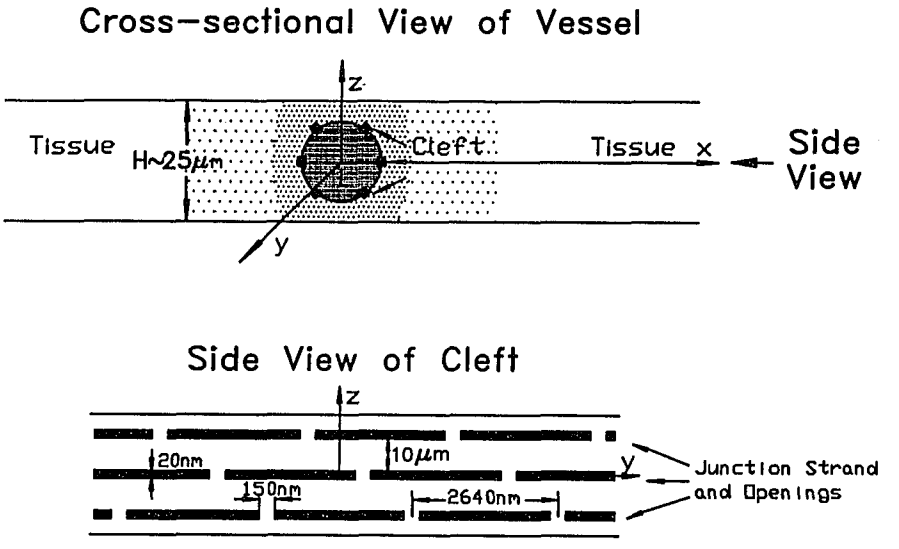

Fig. 3.1 Schematic of model for confocal microscopy. **(a)** cross-sectional view of frog mesenteric microvessel with several clefts distributed around perimeter of vessel wall. Shading indicates decreasing concentration of fluorescent probe as one proceeds into tissue. **(b)** side view looking into cleft along length of junction strand. Three clefts shown with periodically spaced large pore junction strand breaks.

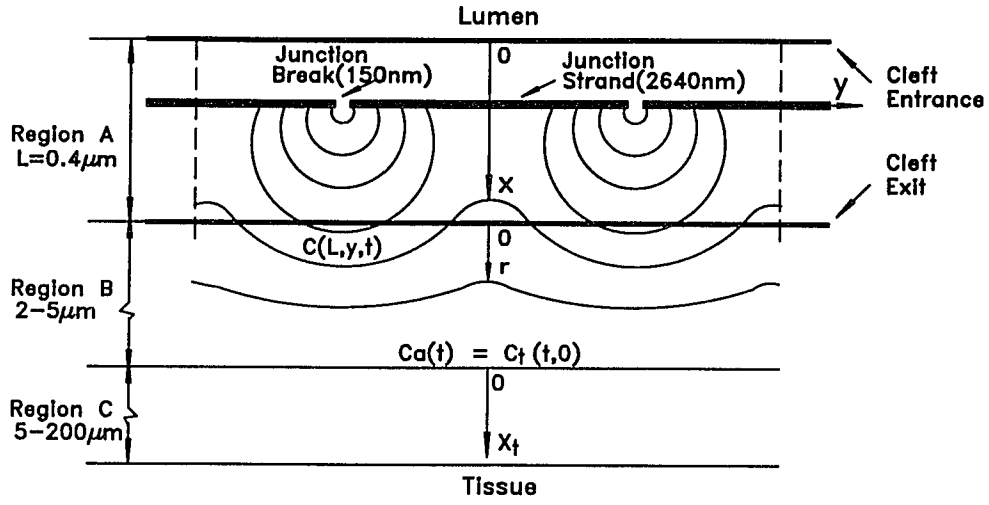

Fig. 3.2 Schematic of mathematical model for predicting concentration profiles in the interendothelial cleft beyond junction strand breaks and in the surrounding tissue space. Model based on three regions with different characteristic length scales whose typical lengths are shown in figure. Region A is the cleft area. Region B is where the solute flux from the individual cleft merges each other, r = 0 is its origin. Region C is the tissue space, x_t = 0 is its beginning.

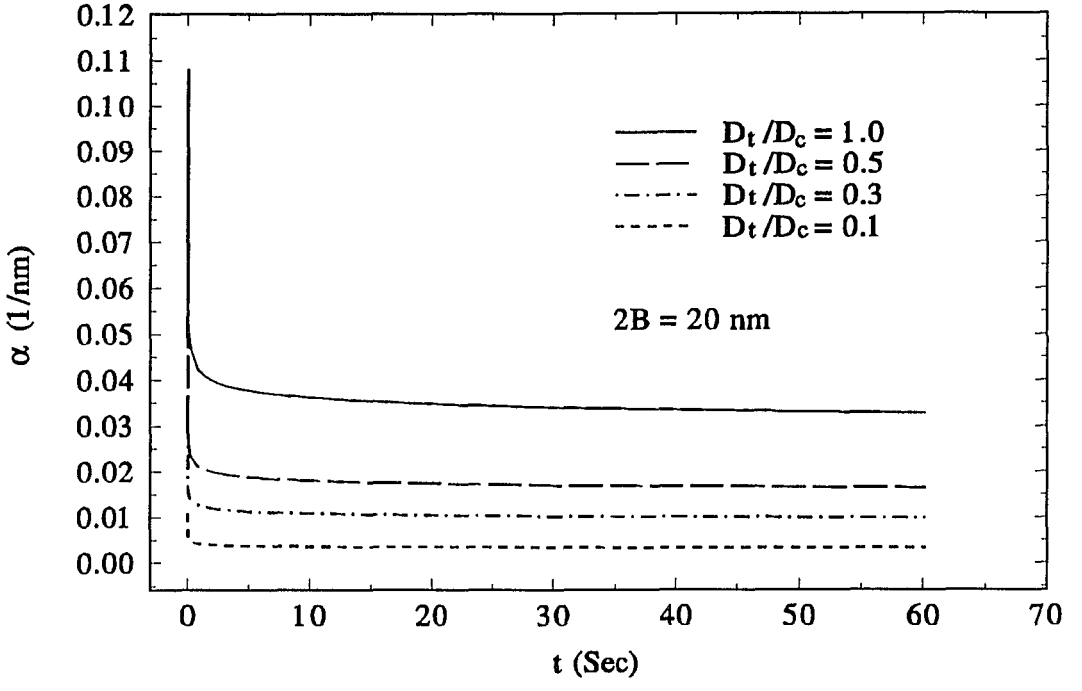

Fig. 3.3 Cleft exit coefficient α as a function of time and the ratio of the solute diffusivity in the tissue D_t to that in the cleft D_c. B is the half width of the cleft.

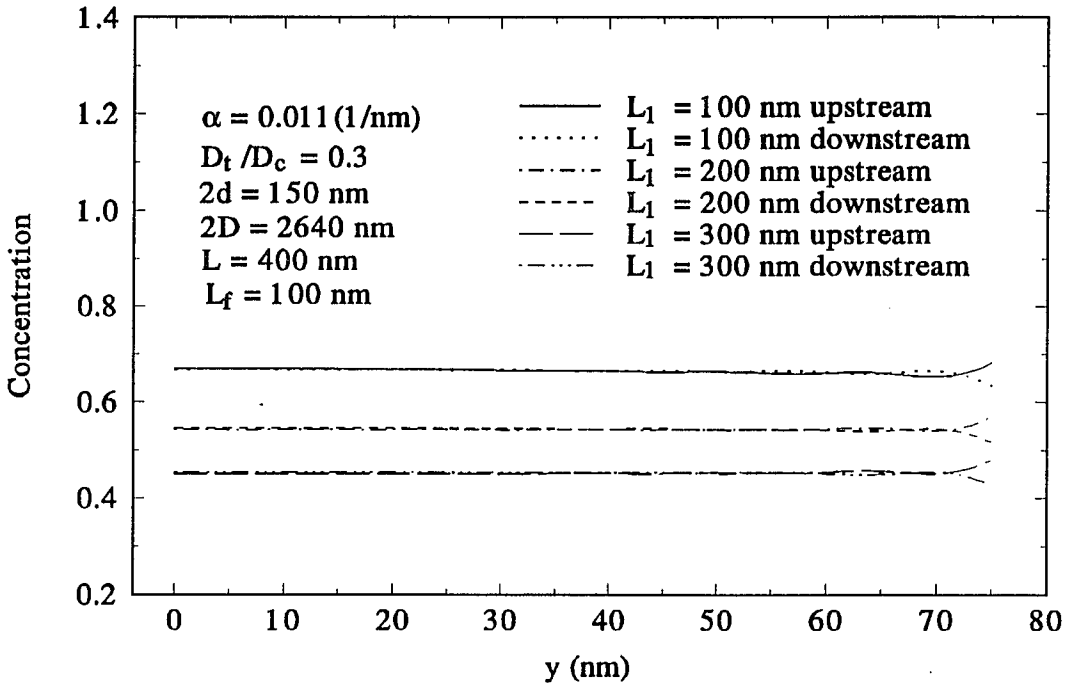

Fig. 3.4 Concentration profiles at the junction orifice for different L_1. Solid and dotted lines are concentrations on the upstream and downstream side of the orifice when L_1 = 100 nm. Dash-dot-dash and short dash lines are for L_1 = 200 nm. Long dash and dash-dot-dot lines are for L_1 = 300 nm. Large pore only and the depth of the fiber layer at the entrance of the cleft L_f = 100 nm. The cleft exit coefficient α = 0.011 nm^{-1}. D_t, D_c are the solute diffusivities in the tissue and in the cleft, respectively.

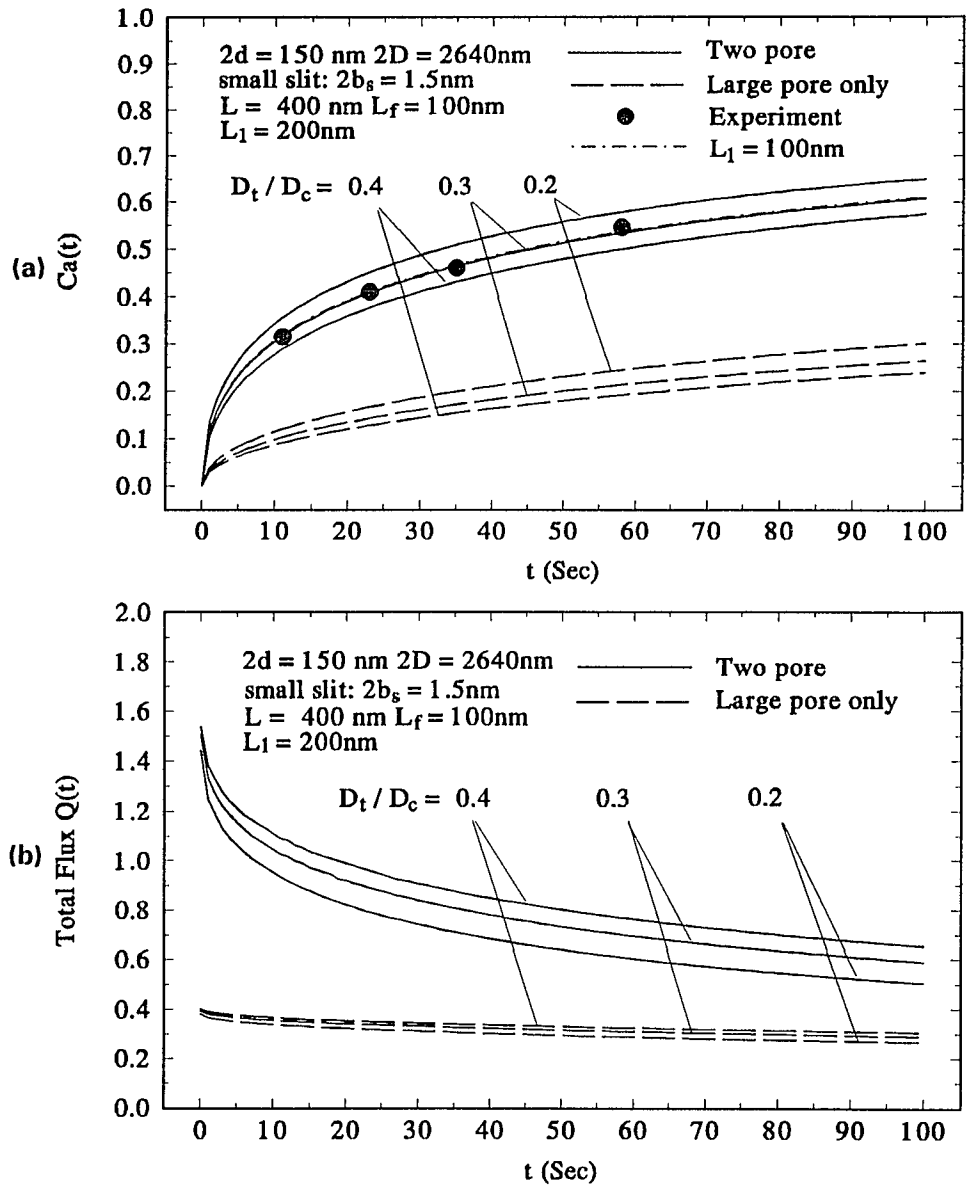

Fig. 3.5 **(a)** The tissue concentration at vessel wall $C_a(t)$ as a function of time for different values of D_t/D_c(Based on data published in Adamson et al., 1994). L_f is the depth of the fiber layer on the surface of endothelium and at the entrance region of the cleft. Dashed lines are results from the basic 150 nm x 20 nm orifice model and solid lines are results from a two pore model consisting of large 150 nm x 20 nm orifice pore and a continuous narrow slit of width 1.5 nm. Solid circles are the data from the experiment. Dot-dash-dot line is for L_1 = 100 nm. All others are for L_1 = 200 nm. **(b)** The total flux Q(t) from the cleft leakages as a function of time for different values of D_t/D_c. Dashed lines are for large orifice only model, solid lines for two pore model. L_1 = 200 nm, L_f = 100 nm.

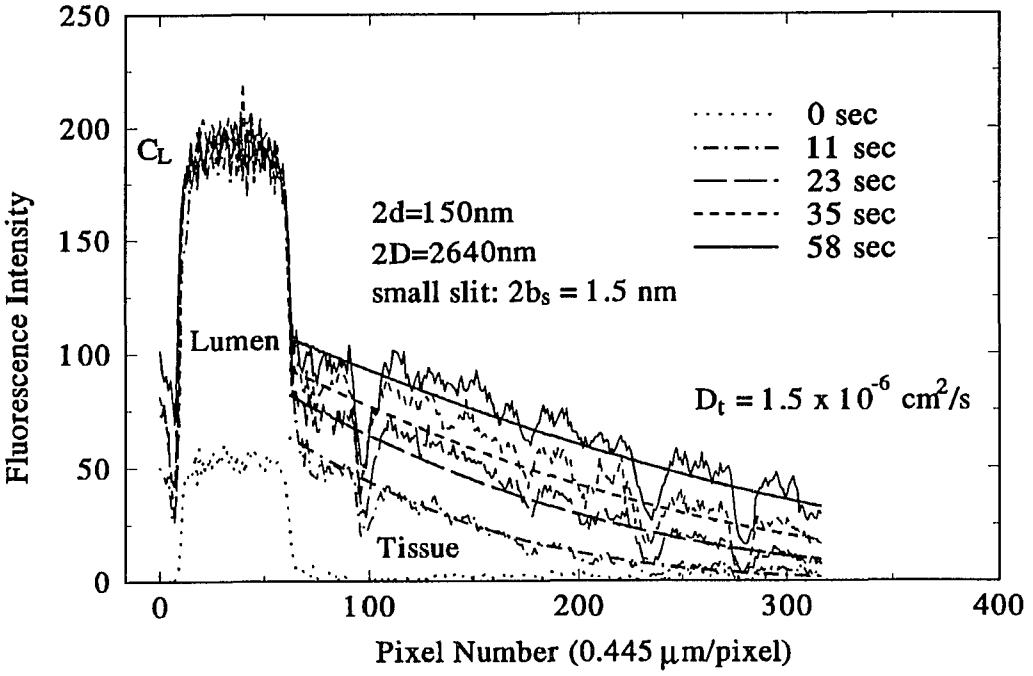

Fig. 3.6 Two pore model results for time dependent concentration distributions in the surrounding tissue. Parameters used are the same as in Figs. 3.5(a), (b). D_t is the optimum fit diffusivity in the tissue. Experimental data courtesy of R. Adamson.

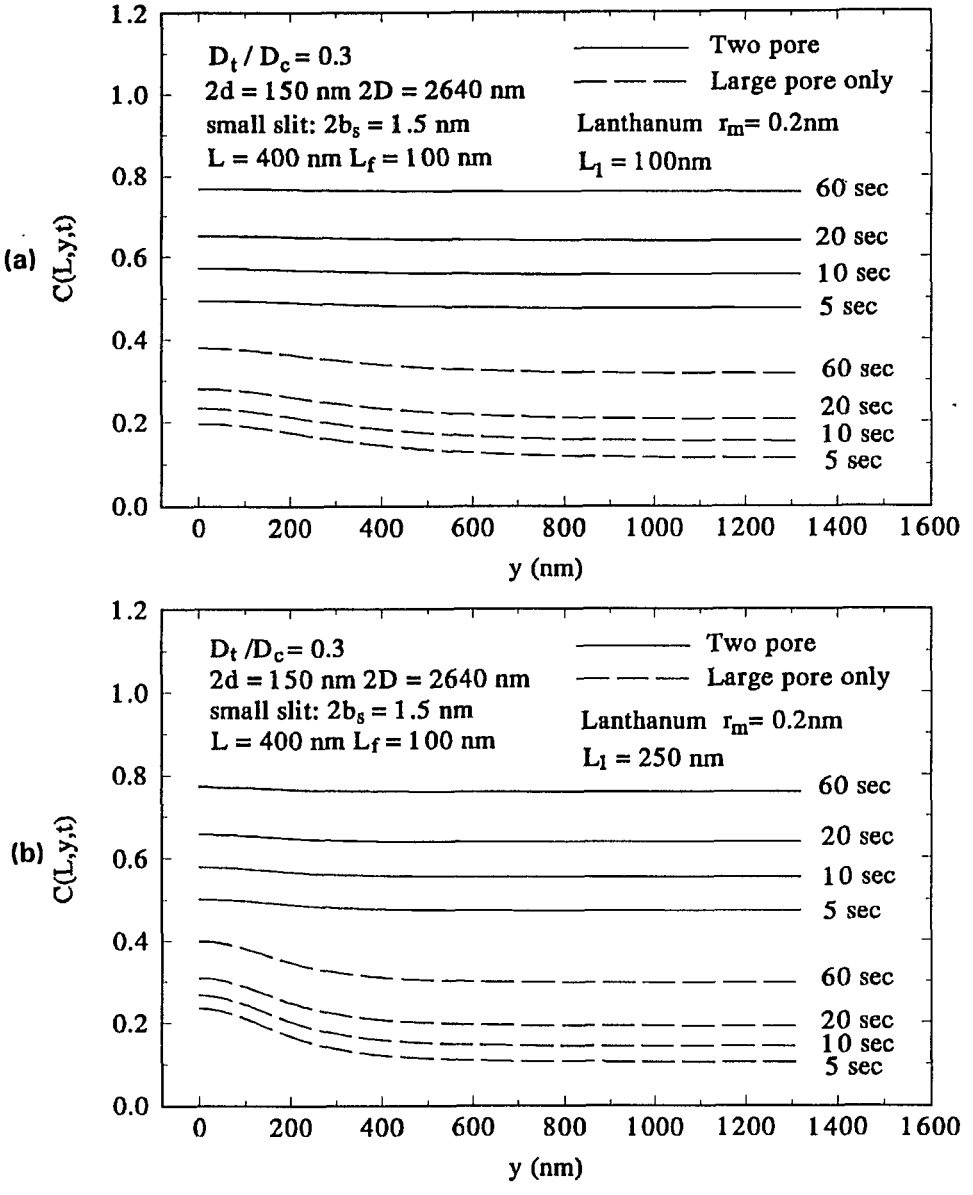

Fig. 3.7 The time dependent concentration distribution at the cleft exit for lanthanum tracers. Dashed lines for large 150 x 20 nm pore only model and solid lines for two pore model. The ratio of diffusivity in the tissue and in the cleft D_t/D_c = 0.3. The thickness of fiber entrance layer L_f = 100 nm. r_m = 0.2 nm is the radius of la^{3+}. **(a)** The distance between the junction strand and the cleft front at the lumen side L_1 = 100 nm; **(b)** L_1 = 250 nm.

CHAPTER 4

A CONVECTIVE-DIFFUSION MODEL FOR INTERPRETING THE LABELING OF INTERENDOTHELIAL CLEFTS BY HIGH MOLECULAR WEIGHT TRACERS

4.1 INTRODUCTION

In this chapter a time dependent convective-diffusion model will be developed to analyze the two-dimensional wake formed by the spreading of high molecular weight tracers downstream of junction strand discontinuities in the interendothelial cleft and the standing gradient flow upstream of the junction strand barrier in the fiber entrance region of the cleft. This model, in conjunction with related experiments which are currently in progress, is designed to evaluate the relative contribution of structures associated with the junctional strand and the fiber matrix to the molecular filter at the microvessel wall.

As stated in previous two chapters, the interendothelial cleft is widely believed to be the principal pathway for water and hydrophilic solute transport through the capillary wall. Freeze fracture studies and ultrathin serial sections have demonstrated that endothelial cells are joined by an array of junctional strands which are interrupted at intervals allowing for the passage of water and solutes whereas cytochemical studies have indicated that the endothelial surface and portions of the wide part of the cleft contain matrix components. There has been a long-standing controversy as to the relative importance of these structures in modulating capillary permeability and which structure determines the selectivity of the microvessel wall.

Important difficulties in reconciling these different approaches are (i) the details of the structural features delineating the narrow regions of the junctions lie beyond the resolution of the electron microscope and (ii) matrix structures in the wide part of the cleft are difficult to visualize directly in electron microscopic studies, Firth et al. (1983) and Shulze and Firth

(1992). In Fu et al. (1995) a multi-region, time dependent diffusion model for the spread of low molecular tracers in the cleft and surrounding tissue space of frog mesentery capillaries was developed (see Chapter 3). It was proposed that, instead of observing the junctional strand structure directly, we should attempt to construct a detailed picture of the junction strands as a transport barrier from a combined two-dimensional theoretical and experimental analysis of the relatively larger wake formed by the time dependent spreading of different size molecular tracers on the downstream side of the junction strand discontinuities. In this study this approach is extended to larger size tracers, such as HRP, where both convection and molecular sieving effects are important. These effects will be shown to significantly alter the tracer wake profiles on the tissue side of the junction strand, at high filtration flow rates, Peclet numbers $P_e > 1$.

Two alternative hypotheses have been formulated to describe the size selective structures that determine capillary permeability. One hypothesis proposes that the molecular filter lies within small pores or constricted slits in the strand of molecules forming the junctional complex between adjacent endothelial cells (Crone and Levitt, 1984). The second hypothesis also proposes that the breaks in the junctional strand determine small solute permeability, but assumes that the primary molecular filter is a fibrous network associated with the cell surface and/or the wide part of the junctional cleft, Curry and Michel (1980), Michel (1988). In Weinbaum et al. (1992) a three-dimensional model was developed to quantitatively evaluate these two hypotheses using a combined model that allowed for junction pores of different cross-section and a sieving matrix that was distributed throughout the wide part of the cleft. The results of the model predicted that a sieving matrix which occupied the entire depth of the cleft offered too much hydraulic resistance and that the measured permeability for intermediate size solute was best fit by infrequent large pores that occupied a small fraction of the junction length.

The recent serial section electron microscopic studies of frog mesentery by Adamson and Michel (1993) have provided strong evidence in support of the predictions in Weinbaum et al. (1992) and the matrix being the molecular filter. These investigators observed infrequent large breaks of typically 150 nm width, but whose gap height (20 nm) was the same as the wide part of the cleft. These observations supported earlier, less definitive studies on rat heart capillaries, Bungaard (1984), which found shorter breaks of a single section thickness (40-50 nm) whose gap height was also nearly the same as the wide part of the cleft. While such large pores could not serve as a molecular filter for intermediate size solutes up to the size of albumin (7 nm dia.), it did not rule out the possibility of smaller pores or slits in the junction strand. Structures suggestive of such smaller pores have been observed in ultrathin (12-15 nm) serial sections, Bungaard (1984), and in sections that have been subject to goniometric tilting, Adamson and Michel (1993). The study by Adamson and Michel (1993) was also important in that it provided the first reliable bounds on the frequency (spacing) of the large breaks. This spacing ranged from 2140 nm based on serial sectioning to 4400 nm (frequency of lanthanum wake leakage sites that penetrated to the tissue border of the cleft) with an average spacing between breaks of both types of 2640 nm.

These experimental results and the theoretical predictions in Weinbaum et al. (1992) led Fu et al. (1994) to propose a combined model with infrequent large orifice like junctional breaks, a finite region of fiber matrix components at the entrance of the cleft and at the endothelial surface and very small pores or slits in the continuous part of the strand (see Chapter 2). Three important quantitative predictions were obtained from this model. First, the measured hydraulic conductivity for frog mesentery could be achieved if the total thickness of the sieving layer was ~ 100 nm and thus about one-quarter of the cleft depth. Second, the permeability of solutes > 1.5 nm diameter up to the size of albumin could be accounted for by

the large 150 nm orifice like breaks which occupied only about 5 percent of the junction length. Third, the infrequent 150 nm junction strand discontinuities could only account for about 1/3 of the measured permeability for small ions and a second family of very small pores, was required for solutes < 1.5 nm diameter. Goniometric tilting of sections in Adamson and Michel (1993) suggested that a narrow ~ 2 nm continuous slit in the uninterrupted part of the strand might be a candidate fo. these pores and the theoretical predictions in Fu et al. (1994) confirmed the quantitative feasibility of this hypothesis. The results of this combined 3-D model for frog mesentery provide very good agreement with measured data for both hydraulic conductivity and permeability for solutes of size ranging from as small as potassium to as large as albumin. This model is also able to account for the measured change in hydraulic conductivity of frog mesenteric capillary after the enzymatic degradation of the surface glycocalyx, Adamson (1990).

The principal motivation for the development of the two-dimensional convective-diffusion wake model proposed in this study is to design experiments that can test for the location of the molecular filter. Whereas the wake of a small electron dense tracer on the abluminal side of the junctional strand provides information about the size and frequency of the discontinuities which can be easily penetrated by small solutes, the distribution of larger molecular weight solutes on the luminal side of the junction barrier will help us determine the location of the molecular sieve. If the breaks in the junctional strand are the primary molecular filter, the present model shows that there will be a large asymmetry in the tracer concentration and its distribution fore and aft of the strand at the sites of small solute leakage due to convective effects at high flow rates. On the other hand, if the accumulation of the tracer is near the entrance of the cleft or the tracer concentration decreases with increasing depth into the cleft towards the junctional strand, this would suggest that the fiber matrix is the principal molecular

sieve. The models for the ultrafiltration of solute at the junction strand or by matrix components in the wide part of the cleft will examine these possibilities.

In the model developed in this chapter, we shall first obtain the solutions for the pressure and velocity fields by extending the model in Fu et al. (1994) (see Chapter 2) for the filtration flow through an isolated orifice to that for a periodic array of orifices. The solution for this velocity field is then used as an input in the convective-diffusion model for the wake concentration profiles on the abluminal side of the junction strand. A fundamental assumption in Fu et al. (1994) and all previous models of capillary interendothelial clefts is that the tissue can be treated as an infinite reservoir with an effectively vanishing solute concentration at the cleft exit. Predictions of capillary permeability are thus based on a critical simplifying assumption that the transendothelial driving force for solute diffusion is constant over the time course of an experiment. However, recent confocal microscopic studies using the low molecular weight tracer, sodium fluorescein, by Adamson et al. (1995) and the corresponding theoretical model in Fu et al. (1995) (see Chapter 3) indicate that the interpretation of tracer studies depends strongly on the tissue concentration at the cleft exit. This exit concentration, in turn, depends on the time dependent spread of tracer in the tissue space. The labeling of the cleft is, thus, intimately coupled to the transport of the tracer in the tissue surrounding the vessel wall. The solute flux at the cleft exit varies both with the distribution of pores along the length of the junction strand and with time as the tissue concentration increases. The more realistic boundary condition at the cleft exit proposed in Fu et al. (1995) for diffusion will be extended in this paper to explore the convective-diffusive wake of large molecular weight tracers.

The theoretical predictions in Fu et al. (1995) indicate that the rapid rise in tissue concentration surrounding the vessel wall measured in Adamson et al. (1995) requires the presence of a distributed family of small pores which serve as the primary pathway for low

molecular weight solutes. In particular, it is shown that the 1.5 nm continuous slit proposed in Fu et al. (1994) has the right permeability-area properties to account for the time dependent sodium fluorescein profiles measured in our confocal microscope experiments. This small pore pathway allows the passage of water and, thus, in the case of high molecular weight tracers, leads to an unstirred layer on the luminal side of the junction strand whose detailed concentration profile will depend on the properties of the matrix layer in the entrance region of the cleft. An ultrafiltration model will also be developed to examine the structure of this unstirred layer and the effect of matrix components.

The solution of the coupled 3-D boundary value problem linking the water and solute transport in the cleft with that in the surrounding tissue would be a formidable task even for a large capacity latest generation computer. Asymptotic techniques are used to greatly simplify the mathematical formulation. Rather surprisingly, we have been able to obtain closed form solutions for the concentration profiles in the cleft despite the complexity of the water flow streamlines and the presence of matrix components. This has been made possible by a now seldom used potential flow transformation, first proposed by Boussinesque, which allows us to both greatly simplify the boundary conditions and reduce the convective-diffusion equation for solute transport into a constant coefficient equation that can be solved analytically.

4.2 MATHEMATICAL MODELS

4.2.1 Model Geometry

We shall use the same geometry for the three dimensional simplified structure of the intercellular cleft as proposed in Fu et al. (1994), see Figs. 2.1(a),(b) in Chapter 2. In this model the junction strand is idealized as a barrier with periodically spaced large pore breaks and a continuous narrow slit which is impermeable to solutes $>$ 1.5 nm diameter. Region 1, $0 <$

$x < L_1$ and region 3, $L_1+L_2 < x < L_1+L_2+L_3$, are the wide portions of the cleft on the lumen and tissue sides of the junction strand. Region 2, $L_1 < x < L_1+L_2$ represents the depth of the pores in the junctional strand. In our model the periodic large pores can be viewed as rectangular slits with cross-section 2d x 2b, where 2b = 2B. Here 2B is the height of the wide part of the cleft and 2d is the length of the discontinuity in the junctional strand. The distance between two adjacent pores is 2D. The measured average values of the large pore cross-section in frog mesentery is 150 nm x 20 nm and the average pore spacing 2D = 2640 nm (Adamson and Michel, 1993). Since the thickness of the junction strand, ~ 10 nm, is small compared to 2d and 2D, the breaks can be treated as zero thickness orifices. The 1.5 nm continuous narrow slit is required to account for the diffusive permeability of solutes less than 1.5 nm diameter. The hydraulic conductivity of this narrow slit is, however, small compared to the large pore orifices. In our model, we only consider molecules with diameter greater than 1.5 nm and, therefore, can ignore this small pore system unless we wish to study the ultrafiltration profiles upstream of the junction strand.

L_f in Fig. 2.1(a) is the depth of the fiber entrance layer in the cleft. This entrance layer includes both the 60 nm thick surface matrix observed in Adamson and Clough (1992) and an entrance layer at the mouth of the cleft. As hypothesized in Michel (1988) the fibers are assumed to form a periodic array. As shown in Fu et al. (1994) the ordered fiber array provides more realistic predictions for hydraulic conductivity than the random array (see Figs. 2.4 in Chapter 2). The fiber diameter is 2a and the average open spacing between fibers is Δ. The volume fraction of the fiber matrix is S_f. The hydrodynamic theory for predicting the added hydraulic and diffusive resistances of this bounded perpendicular fiber array is presented in Weinbaum et al. (1992). This theory also accounts for the steric exclusion of the fibers.

4.2.2 Model Description

Fig. 3.2 is a top view of the concentration profiles that one would observe at some instant in time in the mid-plane of a cleft and its continuation into the tissue space if one were to traverse the length of the cleft along the plane z = 0 in Fig. 3.1(b). The three region model sketched in Fig. 3.2 was first proposed in Fu et al. (1995) (see Chapter 3). The inner region A of length scale L (0.4 μm) characterizes the detailed concentration profiles on the abluminal side of junction strand in the cleft proper. The intermediate region B of length scale 2-5 μm characterizes the mixing of the wakes from the individual junction strand discontinuities in the tissue space immediately surrounding the cleft exit. The far field, region C of length scale 200 μm, describes the tissue profiles that one would observe in the confocal microscope. These tissue profiles satisfy one-dimensional, time dependent diffusion from an integrated source whose total strength is the sum of the exit jets from all the orifice breaks sketched in the side view of Fig. 3.1(b).

The inner cleft region A, is described by the idealized geometric model for the junction strand and the fiber matrix introduced in Fig. 2.1 (see Chapter 2). The boundary value problem for the present model on this inner length scale differs from Fu et al. (1995) in that the governing equation and the boundary conditions consider convection as well as diffusion.

The governing equation for unsteady convective-diffusion is

$$\frac{\partial \tilde{C}}{\partial \tilde{t}} = \tilde{D}^{(*)}\tilde{\Delta}\tilde{C} - \tilde{V}_s \cdot \tilde{\nabla}\tilde{C} \qquad (4.1a)$$

where $\tilde{C} = \tilde{C}(\tilde{t}, \tilde{x}, \tilde{y}, \tilde{z})$ is the concentration distribution and $\tilde{V}_s$ is the solute velocity. $\tilde{D}^{(*)}$ is the solute diffusivity in region *, the asterisk indicating region A, B or C as the case may be. If we choose $\tilde{T}$ as the typical time scale in the experiment, and choose $\tilde{L}^*$ and $\tilde{V}_0^*$ as the characteristic length and velocity in region *, one can write Eq. 4.1a in the dimensionless form

$$\frac{\partial C}{\partial t}\,\epsilon = \Delta C - Pe^{(*)} v C \qquad (4.1b)$$

where

$$C = \frac{\tilde{C}}{\tilde{C}_L}, \quad t = \frac{\tilde{t}}{\tilde{T}}, \quad \Delta = \tilde{L}^{*2}\tilde{\Delta}, \quad \epsilon = \frac{\tilde{L}^{*2}}{\tilde{D}^{(*)}\tilde{T}}, \quad v = \frac{\tilde{V}}{\tilde{V}_0^*}, \quad Pe^{(*)} = \frac{\tilde{V}_0^*\tilde{L}^*}{\tilde{D}^{(*)}}$$

Here $\tilde{C}_L$ is the concentration in the lumen. The behavior in region * depends on the size of the dimensionless diffusion parameter ϵ. If $\epsilon << 1$, i.e. the time of the experiment $\tilde{T} >> \tilde{L}^{*2}/\tilde{D}^{(*)}$, the characteristic time for the filling of a region of length scale $\tilde{L}^*$ by solutes of diffusivity $\tilde{D}^{(*)}$, the unsteady term on the left hand side of Eqs. 4.1a,b can be neglected and the behavior in this region treated as quasi-steady. In this limit the concentration at the boundaries of the region can be treated as slowly varying functions of time, but the instantaneous concentration profiles in the region are the same as for steady state diffusion. If $\epsilon \geq O(1)$, then the unsteady term must be retained since the transient filling of the tissue in region * is important. Another important parameter in Eq. 4.1b is the Peclet number $Pe^{(*)}$ in region *. If $Pe^{(*)} << 1$, convective-diffusion (second term on the right hand side of Eqs. 4.1a,b) in region * can be ignored and Eq. 4.1a or 4.1b reduced to a pure diffusion problem. Otherwise if $Pe^{(*)} \geq O(1)$, the convective effect must be considered.

For the inner cleft region A, the characteristic length $\tilde{L}^* = 0.4$ μm and $\tilde{D}^{(*)}$ for HRP is $\sim 3.5 \times 10^{-7}$ cm^2/s; $\tilde{L}^{*2}/\tilde{D}^{(*)}$ is 4.6×10^{-3} seconds for this inner region. The diffusivity $\tilde{D}^{(*)}$ in the tissue space (regions B and C) is estimated as $\sim 1.1 \times 10^{-7}$ cm^2/s as shown later; therefore, the characteristic times for the intermediate field (region B, 2-5 μm) and far field (region C, 5-200 μm) are $\sim$ 2.3 seconds and $\sim$ 60 minutes, respectively. The typical time for the measurement of the concentration profiles for our high MW tracers, approximately 10-60 seconds, is thus long compared to the characteristic diffusion times in both regions A and B.

The above asymptotic analysis of the different length scales and characteristic times reveals that important simplifications can be introduced for each region. On the time scale, typically 60 seconds, over which our experiments are performed, the concentration in regions A and B can be treated as time varying, but satisfying a quasi-steady diffusion equation. On the length scale of the intermediate region (2-5 μm) the solute flux at the cleft exit (height 20 nm) can be treated as a time varying line source whose strength varies along its length. The line integral of this source provides the unknown time dependent source strength for the far field. On the length scale of the far field (200 μm), the intermediate region B can be viewed as the origin $x_t = 0$ (see Fig. 3.2) of a lowest order outer expansion in which the concentration $C_a(t)$ at the outer limits of the intermediate region B serves to define the flux entering the far field.

The critical matching condition coupling the local continuity of flux leaving the cleft exit and entering the far field is given by

$$-\frac{\partial C}{\partial x} + Pe^{(3)}u_0(L,y)C = \alpha(t)[C(t,L,y) - C_a(t)] \tag{4.2}$$

where $\alpha(t)$ is a time varying function that is determined from the local solution for the line source at the cleft exit in the intermediate region B. $\partial C/\partial x$ is the local gradient at the cleft exit, $Pe^{(3)}$ is the Peclet number in region 3 and $u_0(L, y)$ is the water velocity in the midplane of the cleft exit. It is shown in Appendix that for our model geometry and typical values of the transcapillary driving pressure, the solute transport in the tissue space can be approximated as a pure diffusion process and thus $\alpha(t)$ is obtained through the same procedure as in Fu et al. (1995) (see Chapter 3). The results in Fu et al. (1995) show that there are large variations in α at early times, $t << 1$ sec., but then α approaches an asymptotic constant that is a function of the gap height 2B and the diffusion coefficient ratio, $\tilde{D}_t/\tilde{D}_c$, for the diffusivity of the extravascular tissue compared to the extracellular channel within the cleft. The integral of Eq.

4.2 along x = L, the cleft exit plane, provides the time varying source strength for the far field. Using an iterative matching procedure, which will be described later, one is able to find a solution for the time dependent concentration distribution in the cleft which couples the transport in region A with the filling of the tissue space in regions B and C.

4.2.3 Mathematical Formulation

1. Pressure and velocity field in cleft

(A) Hele-Shaw flow in the cleft

Before considering the convective-diffusion problem, we first need to determine the velocity field for the flow geometry in Fig. 2.1. We assume a steady pressure and velocity field in our model. Since the height of the cleft 2B is small compared to both the average distance between the pores 2D, and the depths L_1 and L_3 of the cleft, the water flow in the wide part of the cleft in regions 1 and 3 can be approximated by a Hele-Shaw flow. To describe this filtration flow we introduce the following dimensionless variables and parameters

$$V=\frac{\tilde{V}}{\tilde{V}_a}, \quad p=\frac{\tilde{p}}{\tilde{p}_L-\tilde{p}_A} \tag{4.3a}$$

$$\phi=\frac{\tilde{\phi}}{\tilde{V}_a\tilde{L}}, \quad \psi=\frac{\tilde{\psi}}{\tilde{V}_a\tilde{L}} \tag{4.3b}$$

$$\mu=\frac{\tilde{V}_a\tilde{\mu}}{(\tilde{p}_L-\tilde{p}_A)\tilde{L}} \tag{4.3c}$$

Here $\tilde{V}=(\tilde{U}, \tilde{V}, \tilde{W})$ is the local water velocity, $\tilde{V}_a = \tilde{Q}_w/4\tilde{B}\tilde{d}$ is the averaged velocity in the junction orifices (this is the velocity scale $\tilde{V}_0^*$ in the cleft), and $\tilde{Q}_w$ is the volume flow rate through the orifice. $\tilde{p}_L$ and $\tilde{p}_A$ are the pressures at the lumen and tissue fronts of the cleft, $\tilde{L}$

is the depth of the entire cleft, $\tilde{\mu}$ is the fluid viscosity, and $\tilde{\phi}$ and $\tilde{\psi}$ are the velocity potential and the stream function. The dimensionless continuity and momentum equation for this flow are

$$\frac{\partial u}{\partial x} + \frac{\partial v}{\partial y} = 0 \tag{4.4}$$

$$\nabla p = \mu \frac{\partial^2 V}{\partial z^2} \qquad V = ui + vj + 0k \tag{4.5}$$

Here p = p(x, y) is the pressure, V = (u, v, w) is the flow velocity, w = 0 is the approximation for Hele-Shaw flow and μ is defined in (4.3c).

The no-slip boundary conditions are satisfied on the surface of the plasmalemma membranes of the cleft

$$u = v = 0 \qquad z = \pm B \tag{4.6}$$

The solution of Eq. 4.5 which satisfies Eq. 4.6 is

$$V = V_0 \left(1 - \frac{z^2}{B^2}\right) \tag{4.7}$$

where

$$V_0 = -\frac{B^2}{2\mu} \nabla p \qquad V_0 = u_0 i + v_0 j \tag{4.8}$$

is the velocity in the center plane (z = 0) of the cleft. If a fiber matrix exists in the wide portion of the cleft, it is shown in Tsay and Weinbaum (1991), that Eq. 4.5 can be replaced by a Brinkman equation. The latter equation when solved subject to non-slip boundary conditions at z = $\pm$B enables one to define an effective viscosity μ_{eff}

$$\mu_{eff} = \frac{(\frac{B}{\sqrt{K_P}})^3}{3(\frac{B}{\sqrt{K_p}} - \tanh(\frac{B}{\sqrt{K_p}}))}\mu \qquad (4.9)$$

which can be used to replace μ in (4.8). Here K_p is the Darcy permeability. μ_{eff} describes the additional hydraulic resistance due to the viscous fiber interaction with the plasmalemma boundaries of the cleft. Since the fiber fills only the entrance region of the wide part of the cleft, one would need to solve a three region problem to obtain the nonuniform pressure and concentration profiles at the interface $x = L_f$ between the fiber and non fiber regions. A reasonable approximation proposed in Fu et al. (1994) (see Chapter 2), however, is to assume an average effective viscosity in region 1, $\mu^{(1)}$, which is an average of μ_{eff} in the fiber layer and μ in the fiber free subregion, which is proportional to the relative depth of each region. Thus,

$$\mu^{(1)} = \frac{\mu_{eff}L_f + (L_1 - L_f)\mu}{L_1} \qquad (4.10)$$

(B) Boundary value problem for Pressure

The x, y components of the center plane velocity satisfy the irrotationality condition for two-dimensional potential flow. Combining Eqs. 4.7 and 4.8 and substituting into Eq. 4.4, one obtains

$$\frac{\partial^2 p}{\partial x^2} + \frac{\partial^2 p}{\partial y^2} = 0 \qquad (4.11)$$

Since the velocity in the x, y plane satisfies the potential flow equation, the non-slip boundary conditions can not be satisfied in the x, y plane if Eq. 4.5 is used as the approximate momentum equation. The boundary conditions for Eq. 4.11 in regions 1 and 3 are

$$p^{(1)} = p_L \qquad x = 0, \qquad |y| < D \tag{4.12a}$$

$$\frac{\partial p^{(i)}}{\partial y} = 0 \qquad i = 1,\ 3 \qquad 0 \le x \le L \qquad y = 0,\ D \tag{4.12b}$$

$$p^{(1)} = p^{(3)} \qquad x = L_1 \qquad |y| < d \tag{4.12c}$$

$$-\frac{B^2}{2\mu^{(1)}}\frac{\partial p^{(1)}}{\partial x} = -\frac{B^2}{2\mu^{(3)}}\frac{\partial p^{(3)}}{\partial x} \qquad x = L_1 \qquad |y| < d \tag{4.12d}$$

$$\frac{\partial p^{(i)}}{\partial x} = 0 \qquad i = 1,\ 3 \qquad x = L_1 \qquad d < |y| < D \tag{4.12e}$$

$$p^{(3)} = p_A \qquad x = L \qquad |y| < D \tag{4.12f}$$

where $\mu^{(1)}$ and $\mu^{(3)}$ are the effective viscosities in regions 1 and 3.

It is difficult to obtain a closed form solution to Eq. 4.11 subject to boundary conditions 4.12a-f, since the split boundary conditions 4.12c,d,e at the junction barrier are of mixed type involving both the pressure and its gradient. To eliminate this difficulty, we assume periodically distributed junctional orifices and prescribe a functional form for the velocity profile at the orifice opening, which is a modified form of the solution obtained in Fu et al. (1994) (see Eq. 2.17b in Chapter 2) for an isolated orifice in a junction strand. This velocity is given by

$$\begin{aligned} -\frac{B^2}{2\mu^{(1)}}\frac{\partial p^{(1)}}{\partial x} &= -\frac{B^2}{2\mu^{(3)}}\frac{\partial p^{(3)}}{\partial x} \\ &= \frac{\eta}{\sqrt{\gamma^2 - \cosh^2(\pi y)}} \qquad x = L_1 \qquad |y| < d \end{aligned} \tag{4.13}$$

where

$$\gamma = \cosh(\pi d)$$

The velocity profiles used in (4.13) differ from the isolated orifice in that an unknown

coefficient η is introduced. η is determined by satisfying Eq. 4.12c in an integrated average sense over the orifice opening. This very useful approximation will be examined later and shown to be highly accurate.

(C) Solution for pressure

The solution of the boundary value problem defined by Eqs. 4.11 and 4.12a-f, with matching condition 4.12d given by Eq. 4.13, is for region 1

$$p^{(1)}(x,y) = p_L + A_0 x + \sum_{n=1}^{\infty} A_n \cos(\lambda_n y)\sinh(\lambda_n x) \qquad 0<x<L_1 \tag{4.14}$$

and for region 3,

$$p^{(3)}(x,y) = p_A + B_0(x-L) + \sum_{n=1}^{\infty} B_n \cos(\lambda_n y)\sinh[\lambda_n(x-L)] \qquad L_1<x<L \tag{4.15}$$

where

$$\lambda_n = \frac{n\pi}{D}$$

$$A_0 = [-\frac{2\mu^{(1)}}{B^2}\frac{1}{\pi D\gamma}K(\sqrt{1-\gamma^{-2}})]\ \eta$$

$$B_0 = \frac{\mu^{(3)}}{\mu^{(1)}} A_0$$

$$A_n = -\frac{2\mu^{(1)}}{B^2}\frac{2\eta}{\lambda_n D\cosh(\lambda_n L_1)}\int_0^d \frac{\cos(\lambda_n y)}{\sqrt{\gamma^2-\cosh^2(\pi y)}}dy \tag{4.16}$$

$$B_n = \frac{\mu^{(3)}}{\mu^{(1)}} \frac{\cosh(\lambda_n L_1)}{\cosh(\lambda_n L_3)} A_n \qquad L_3 = L - L_1$$

in Eq. 4.16, K is a complete elliptic integral of the first kind. The solution for η obtained by satisfying condition (4.12c) in an integrated average sense at the orifice is

$$\eta = \frac{B^2}{2\mu^{(1)}} \frac{\pi D\gamma}{SK(\sqrt{1-\gamma^{-2}})} (p_L - p_A) \tag{4.17}$$

where

$$S = L_1 + \frac{\mu^{(3)}}{\mu^{(1)}} L_3 + \sum_{n=1}^{\infty} t(n) \frac{\sin(\lambda_n d)}{\lambda_n{}^2 d} [\tanh(\lambda_n L_1) + \frac{\mu^{(3)}}{\mu^{(1)}} \tanh(\lambda_n L_3)] \tag{4.18}$$

$$t(n) = \frac{2\pi\gamma}{K[(1-\gamma^{-2})^{\frac{1}{2}}]} \int_0^d \frac{\cos(\lambda_n y)}{\sqrt{\gamma^2 - \cosh^2(\pi y)}} dy$$

The average water velocity $\tilde{V}_a$ at the orifice is

$$\tilde{V}_a = \frac{\tilde{B}^2}{2\tilde{\mu}^{(1)}} \frac{2}{3} \frac{\tilde{D}}{\tilde{d}} \frac{(\tilde{p}_L - \tilde{p}_A)}{\pi S \tilde{L}} \tag{4.19}$$

and the velocity field is obtained by substituting the analytic solutions for p, Eqs. 4.14 and 4.15, in Eq. 4.8.

2. Concentration field in cleft

(A) Quasi-steady convective-diffusion model in cleft region A

Since the characteristic time for the diffusive equilibration of the inner cleft region A of length scale 0.4 μm is only 4.6 x 10^{-3} sec. (see Model Description). This is very short compared to the time scale of the experiment, the condition for neglecting the time derivative

term on the left hand side of Eq. 4.1b is well satisfied. Furthermore, since the channel height $2B << L$, the concentration gradients in the x, y directions in the wide part of the cleft, where the flow is of Hele-Shaw type, will not vary significantly across the height of the cleft. The governing equation for solute conservation in these regions can be approximated by a steady 2-D convective-diffusion equation averaged across the cleft height,

$$\nabla^2 C^{(i)} - Pe^{(i)} \mathbf{V}_0 \cdot \nabla C^{(i)} = 0 \qquad i = 1, 3 \tag{4.20}$$

where $C^{(i)} = C^{(i)}(t, x, y)$, $i = 1, 3$ are the actual concentrations in the available volume in regions 1 and 3 and $\mathbf{V}_0 = \mathbf{V}_0(x, y)$ is the water velocity in the center plane $z = 0$. $Pe^{(i)}$, $i = 1, 3$ are Peclet numbers defined as

$$Pe^{(i)} = \frac{2}{3} \frac{\chi^{(i)} \tilde{L} \tilde{V}_a}{\tilde{D}^{(i)}} \qquad i = 1, 3 \tag{4.21}$$

Here $\tilde{V}_a$ is given in Eq. 4.19, $\tilde{D}^{(i)}$, $i = 1, 3$ are the effective solute diffusivities in regions 1 and 3 and $\chi^{(i)}$ is the retardation coefficient describing the slip between the solute and the solvent. The factor 2/3 appears in Eq. 4.21 since the average velocity for the profile (4.7) is 2/3 of the centerline velocity. Since the Hele-Shaw velocity profile is parabolic across the channel height of the cleft, this is a convective enhancement due to Taylor dispersion in the z direction. The convection to $\tilde{D}^{(i)}$ from Taylor dispersion is $2/105(dB/DL)^2 P_e^{(i)2} \tilde{D}^{(i)}$ (Mauri, 1995). Here $P_e^{(i)}$ defined in Eq. 4.21 is ≤ 20, $dB/DL \sim 0.002$ and the enhancement due to convection is of order 10^{-5}. Thus, the Taylor dispersion effect is negligible.

The boundary conditions for solute transport described by Eq. 4.20 are

$$C^{(1)} = C_L \qquad x = 0 \qquad |y| < D \tag{4.22a}$$

$$\frac{\partial C}{\partial y} = 0 \qquad 0<x<L \qquad y=0,\ D \tag{4.22b}$$

$$C^{(1)} = C^{(3)} \qquad x = L_1 \qquad |y|<d \tag{4.22c}$$

$$-\frac{\partial C^{(1)}}{\partial x} + Pe^{(1)} u_0 C^{(1)} = \beta\left(-\frac{\partial C^{(3)}}{\partial x} + Pe^{(3)} u_0 C^{(3)}\right) \qquad x = L_1 \qquad |y|<d \tag{4.22d}$$

$$-\frac{\partial C^{(1)}}{\partial x} + Pe^{(1)} u_0 C^{(1)} = 0 \qquad x = L_1 \qquad d<|y|<D \tag{4.22e}$$

$$-\frac{\partial C^{(3)}}{\partial x} + Pe^{(3)} u_0 C^{(3)} = \alpha\left(C^{(3)} - C_a(t)\right) \qquad x = L \qquad |y|<D \tag{4.22f}$$

where $\beta = \tilde{D}^{(3)}/\tilde{D}^{(1)}$. Boundary condition (4.22a) indicates that the solute concentration of the perfusate in the lumen $\tilde{C}_L$ remains constant. Boundary conditions (4.22b) are the periodicity and symmetry conditions. Boundary conditions (4.22c-e) require that the junctional strand be impermeable except for the pore region $-d < y < d$. Matching condition (4.22f), a restatement of Eq. 4.2, requires that the solute flux entering the tissue at the cleft exit be proportional to the instantaneous local difference between the concentration at the cleft exit and the concentration at the entrance to the far field $C_a(t)$, where $C_a(t)$ is a quasi-steady slowly increasing function of time determined by the solution to the coupled boundary value problem linking the three regions. The flux coefficient α is determined from the solution for the intermediate region B described in appendix. This solution is subtle since one needs to carefully analyze the convective transport surrounding the cleft exit. The final result for α

$$\alpha = \frac{2\pi}{B}\frac{\tilde{D}_t}{\tilde{D}^{(3)}}\frac{1}{\ln\frac{4t}{B^2} - 0.5772} \tag{4.23}$$

turns out to be the same as Fu et al. (1995) (see Eq. 3.29 in Chapter 3) for low molecular

weight solutes where only diffusion in the intermediate region B, Fig. 3.2, was considered.

Using the same approach described in defining an average effective viscosity $\mu^{(1)}$ for region 1, Eq. 4.10, we define an average effective diffusivity $\tilde{D}^{(1)}$ in region 1, which is an average of $\tilde{D}_{i,eff}$ in the fiber layer and $\tilde{D}_{iw}$ in the fiber free subregion,

$$\tilde{D}^{(1)} = \frac{L_1 \tilde{D}_{iw} \tilde{D}_{i,eff}}{\tilde{D}_{iw} L_f + (L_1 - L_f)\tilde{D}_{i,eff}} \tag{4.24}$$

Here $\tilde{D}_{iw}$ is the restricted diffusivity given in Ganatos et al. (1981) for a sphere diffusing in a channel without matrix, but which includes the hydraulic resistance of the plasmalemma boundaries. $\tilde{D}_{i,eff}$ is given in Weinbaum et al. (1992). $\tilde{D}_{i,eff}$ accounts for the effect of both the hydraulic resistance and the steric hindrance of the fibers in the matrix entrance layer. Approximation (4.24) allows us to reduce the boundary value problem for a cleft with a finite matrix entrance layer from a three region to a two region problem.

The retardation coefficient $\chi^{(i)}$ appearing in Eq. 4.21 can be related to the reflection coefficient $\sigma^{(i)}$ in region i, i=1, 3. For region 1 composed of fiber and fiber free layers, the effective reflection coefficient $\sigma^{(1)}$ is given as (Kedem and Katchalsky, 1962)

$$\sigma^{(1)} = \frac{P^{(1)}}{P_{i,eff}} \sigma_{i,eff} + \frac{P^{(1)}}{P_{iw}} \sigma_{iw} \tag{4.25a}$$

where σ_{iw} and $\sigma_{i,eff}$ are the reflection coefficients for a solute in a restricted channel and in an infinite fiber matrix respectively. σ_{iw} and $\sigma_{i,eff}$ are given in Curry (1984). $P^{(1)}$ is the effective permeability in region 1, P_{iw} is the permeability in the fiber free region and $P_{i,eff}$ in the fiber filled region. Eq. 4.25a is derived from the Kedem-Katchalsky equations for the water and solute flux in the limit where the volume flux vanishes and the pressure and osmotic driving forces just balance one another. In this limit the permeability coefficients are related by the

expression for two resistances in series

$$\frac{1}{P^{(1)}} = \frac{1}{P_{i,eff}} + \frac{1}{P_{iw}} \tag{4.25b}$$

Since the permeability here is proportional to D^*/L^*, where D^* is the diffusivity in region * and L^* is the length of region *, Eq. 4.25a can be rewritten as

$$\sigma^{(1)} = \frac{L_f \tilde{D}_{iw} \sigma_{i,eff} + (L_1 - L_f)\tilde{D}_{i,eff}\sigma_{iw}}{\tilde{D}_{iw} L_f + (L_1 - L_f)\tilde{D}_{i,eff}} \tag{4.25c}$$

Here $\tilde{D}_{iw}$ and $\tilde{D}_{i,eff}$ are the same as in Eq. 4.24. The effective retardation coefficient in region 1 is approximately given by $\chi^{(1)} = 1 - \sigma^{(1)}$. This relationship between χ and σ is strictly valid only in the limit of high Pe.

(B) Boussinesque transformation

Despite the complexity of the solutions for $\mathbf{V}_0(x, y)$, an elegant analytical solution to the boundary value problem defined by Eq. 4.20 and Eqs. 4.22a-f can be obtained because of the potential character of the velocity field in the x, y plane. This is due to an extraordinary transformation first developed by Boussinesque in which the physical x, y plane is mapped onto the ϕ, ψ plane, where ϕ is the potential function, and ψ is the stream function, see Figs. 4.1(a),(b). In the ϕ, ψ plane Eq. 4.20 is reduced to a constant coefficient equation

$$\left(\frac{\partial^2 C^{(i)}}{\partial \phi^2} + \frac{\partial^2 C^{(i)}}{\partial \psi^2}\right) - Pe^{(i)}\left(\frac{\partial C^{(i)}}{\partial \phi}\right) = 0 \qquad i = 1, 3 \tag{4.26}$$

The solution of (4.26) is greatly simplified in the ϕ, ψ plane because the boundary abce is a streamline along which $\partial C/\partial \psi = 0$. Furthermore, the pore opening cd is nearly an isobar. To show this we shall first derive expressions for the constant ϕ lines and show they are

isobars.

(C) Boundary value problem for the concentration in ϕ, ψ plane

Since $V_0(x,y)$ describes a potential flow, it can be written as

$$V_0 = \nabla\phi \tag{4.27}$$

Comparing Eqs. 4.27 and 4.8, one notes there is a simple relationship between the potential function $\phi^{(i)}$ and the pressure $p^{(i)}$ for the Hele-Shaw flow in regions 1 and 3,

$$\phi^{(i)}(x, y) = -\frac{B^2}{2\mu^{(i)}} p^{(i)}(x, y) + s^{(i)} \qquad i = 1, 3 \tag{4.28}$$

where $s^{(i)}$ are arbitrary constants to be determined. Eq. 4.28 shows that isobars are isopotential lines.

Since the pressures at the cleft entrance and exit, p_L and p_A, are assumed constant, these boundaries are isobars. Furthermore, we shall assume that the non-uniformity of the pressure obtained from the Hele-Shaw solutions in regions 1 and 3 at the entrance/exit for the rectangular junctional pore is small. For the orifice profiles (4.13), we shall show later in Fig. 4.2 that this approximation is highly accurate. If one assumes that the potential at the entrance of the cleft ($x = 0$, $|y| < D$) is 0, the $s^{(i)}$ in (4.28) are given by

$$s^{(1)} = \frac{B^2}{2\mu^{(1)}} p_L \tag{4.29a}$$

$$s^{(3)} = \frac{B^2}{2} \frac{p_L - p_A}{\mu^{(1)}L_1 + \mu^{(3)}(1 - L_1)} + \frac{B^2}{2\mu^{(3)}} p_A \tag{4.29b}$$

Therefore the potential functions in regions 1 and 3 are

$$\phi^{(1)}(x, y) = \frac{3}{2}\frac{d}{D}[x + \sum_{n=1}^{\infty} \frac{t(n)}{\lambda_n \cosh(\lambda_n L_1)} \cos(\lambda_n y) \sinh(\lambda_n x)] \tag{4.30}$$

$$\phi^{(3)}(x,y) = \frac{3}{2}\frac{d}{D}[(x-L) + \sum_{n=1}^{\infty} \frac{t(n)}{\lambda_n \cosh(\lambda_n L_3)} \cos(\lambda_n y) \sinh(\lambda_n (x-L))] + \phi_L \tag{4.31}$$

Here λ_n and t(n) are defined in (4.16) and (4.18), and ϕ_L, the potential at x = L, is

$$\phi_L = \frac{3}{2}\frac{d}{D}\frac{S}{L_1 + \frac{\mu^{(1)}}{\mu^{(3)}} L_3} \tag{4.32a}$$

where S is also defined in (4.18). ϕ_{L_1}, the potential at $x = L_1$, is

$$\phi_{L_1} = L_1 \phi_L \tag{4.32b}$$

For 2-D potential flow,

$$\frac{\partial \phi}{\partial x} = \frac{\partial \psi}{\partial y}, \qquad \frac{\partial \phi}{\partial y} = -\frac{\partial \psi}{\partial x} \tag{4.33}$$

Thus, Eqs. 4.30, 4.31 and 4.33 give

$$\psi^{(1)}(x, y) = \frac{3}{2}\frac{d}{D}[y + \sum_{n=1}^{\infty} \frac{t(n)}{\lambda_n \cosh(\lambda_n L_1)} \sin(\lambda_n y) \cosh(\lambda_n x)] \tag{4.34}$$

$$\psi^{(3)}(x, y) = \frac{3}{2}\frac{d}{D}[y + \sum_{n=1}^{\infty} \frac{t(n)}{\lambda_n \cosh(\lambda_n L_3)} \sin(\lambda_n y) \cosh(\lambda_n (x-L))] \tag{4.35}$$

and at y = 0, D,

$$\psi_0 = 0 \qquad \psi_D = \frac{3}{2} d \tag{4.36}$$

As shown in Fig. 4.1(b), the complex boundary shape abce and its mirror image below

the x axis transform to the straight lines $\psi = \pm\psi_D$. In summary, boundary conditions (4.22a-f) in the ϕ, ψ plane can be written as

$$C^{(1)} = C_L \qquad \phi = 0 \qquad |\psi| < \psi_D \tag{4.37a}$$

$$\frac{\partial C}{\partial \psi} = 0 \qquad 0 < \phi < \phi_L \qquad \psi = 0, \pm\psi_D \tag{4.37b}$$

$$C^{(1)} = C^{(3)} \qquad \phi = \phi_{L_1} \qquad |\psi| < \psi_D \tag{4.37c}$$

$$-\frac{\partial C^{(1)}}{\partial \phi} + Pe^{(1)}C^{(1)} = \beta\left(-\frac{\partial C^{(3)}}{\partial \phi} + Pe^{(3)}C^{(3)}\right) \quad \phi = \phi_{L_1} \quad |\psi| < \psi_D \tag{4.37d}$$

$$\left[-\frac{\partial C^{(3)}}{\partial \phi} + Pe^{(3)}C^{(3)}\right] u_0(L,y) = \alpha\,[C^{(3)} - C_a(t)] \quad \phi = \phi_L \quad |\psi| < \psi_D \tag{4.37e}$$

Note that boundary conditions (4.22d,e) at $x = L_1$ in the x, y plane have been significantly simplified in (4.37d) at $\phi = \phi_{L1}$ since $u_0(L_1, y)$ cancels out in the ϕ, ψ plane.

(D) Solution for concentration in the cleft

The solutions of Eq. 4.26 satisfying boundary conditions 4.37a-d in regions 1 and 3 are

$$\begin{aligned} C^{(1)} &= a_0 + (1 - a_0)\exp(Pe^{(1)}\phi) \\ &\quad + \sum_{k=1}^{\infty} \cos(\omega_k \psi) a_k [\exp(\beta_{1k}\phi) - \exp(\beta_{2k}\phi)] \qquad 0 < \phi < \phi_{L_1} \end{aligned} \tag{4.38}$$

$$\begin{aligned} C^{(3)} &= b_0 + c_0\exp(Pe^{(3)}\phi) \\ &\quad + \sum_{k=1}^{\infty} \cos(\omega_k \psi)[b_k\exp(\gamma_{1k}\phi) + c_k\exp(\gamma_{2k}\phi)] \qquad \phi_{L_1} < \phi < \phi_L \end{aligned} \tag{4.39}$$

$$\omega_k = \frac{k\pi}{\psi_D}$$

$$\beta_{1,\,2k} = \frac{Pe^{(1)} \pm \sqrt{Pe^{(1)2} + 4\omega_k^{\,2}}}{2}, \qquad \gamma_{1,\,2k} = \frac{Pe^{(3)} \pm \sqrt{Pe^{(3)2} + 4\omega_k^{\,2}}}{2}$$

$$b_0 = \frac{\tilde{D}^{(1)}}{\tilde{D}^{(3)}} \frac{Pe^{(1)}}{Pe^{(3)}} a_0$$

$$c_0 = g_0 a_0 + g_1$$

$$g_0 = \frac{1 - \exp(Pe^{(1)}\phi_{L_1}) - \dfrac{\tilde{D}^{(1)}}{\tilde{D}^{(3)}} \dfrac{Pe^{(1)}}{Pe^{(3)}}}{\exp(Pe^{(3)}\phi_{L_1})}$$

$$g_1 = \exp[(Pe^{(1)} - Pe^{(3)})\phi_{L_1}]$$

$$b_k = h_{1k}\, a_k, \qquad c_k = h_{2k}\, a_k \tag{4.40}$$

$$h_{1k} = \frac{\exp[(\beta_{1k}-\gamma_{1k})\phi_{L_1}]\ (\rho - \dfrac{\tilde{D}^{(1)}}{\tilde{D}^{(3)}}\beta_{1k}+\gamma_{2k}) + \exp[(\beta_{2k}-\gamma_{1k})\phi_{L_1}]\ (-\rho + \dfrac{\tilde{D}^{(1)}}{\tilde{D}^{(3)}}\beta_{2k}-\gamma_{2k})}{\gamma_{2k} - \gamma_{1k}}$$

$$h_{2k} = \frac{\exp[(\beta_{1k}-\gamma_{2k})\phi_{L_1}]\ (-\rho + \dfrac{\tilde{D}^{(1)}}{\tilde{D}^{(3)}}\beta_{1k}-\gamma_{1k}) + \exp[(\beta_{2k}-\gamma_{2k})\phi_{L_1}]\ (\rho - \dfrac{\tilde{D}^{(1)}}{\tilde{D}^{(3)}}\beta_{2k}+\gamma_{1k})}{\gamma_{2k} - \gamma_{1k}}$$

$$\rho = \frac{\tilde{D}^{(1)}}{\tilde{D}^{(3)}} Pe^{(1)} - Pe^{(3)}$$

Here ψ_D is given in Eq. 4.36 and $Pe^{(i)}$, i = 1, 3 is defined in Eq. 4.21.

The only unknowns in Eqs. 4.38, 4.39 are the a_k coefficients. They can be determined by satisfying the last remaining boundary condition 4.37e. Substituting Eqs. 4.38, 4.39, and 4.40 into (4.37e), we obtain

$$f_0(y)\, a_0 + \sum_{k=1}^{\infty} f_k(y)\, \cos[\omega_k \psi^{(3)}(L,y)]\, a_k = R \tag{4.41}$$

$$f_0(y) = -\alpha\, g_0 \exp(Pe^{(3)}\phi_L) - [\alpha + Pe^{(3)} u_0(L,y)]\, \frac{\tilde{D}^{(1)}}{\tilde{D}^{(3)}}\, \frac{Pe^{(1)}}{Pe^{(3)}}$$

$$f_k(y) = h_{1k}\exp(\gamma_{1k}\phi_L)[(\gamma_{1k} - Pe^{(3)})u_0(L,y) - \alpha] + h_{2k}\exp(\gamma_{2k}\phi_L)\, [(\gamma_{2k} - Pe^{(3)})u_0(L,y) - \alpha]$$

$$R = \alpha\, [\exp(Pe^{(3)}\phi_L) g_1 - C_a(t)]$$

Here g_0, g_1, h_{1k}, h_{2k} are the same as in Eq. 4.40. The velocity at the cleft exit $u_0(L, y)$ is obtained from Eqs. 4.8 and 4.15. It is given by

$$u_0(L,y) = \frac{3}{2}\, \frac{d}{D}\, [1 + \sum_{n=1}^{\infty} \frac{t(n)}{\cosh(\lambda_n L_3)} \cos(\lambda_n y)] \tag{4.42}$$

where λ_n and t(n) are defined in (4.16) and (4.18).

The a_k coefficients in Eq. 4.41 can not be evaluated analytically. A boundary collocation method is thus employed in which Eq. 4.41 is satisfied at N+1 collocation points. By simultaneously solving these N+1 linear equations, one can obtain the unknown coefficients a_k

in the solution for the concentration field. In this manner solutions are obtained for the first N+1 coefficients and the infinite series solutions for the concentration, Eqs. 4.38, 4.39, are truncated at the N^{th} term. The collocation points were chosen to be equally spaced on the boundary $\phi = \phi_L$, $0 < \psi < \psi_D$ in the ϕ, ψ plane.

(E) Ultrafiltration in continuous narrow slit pores

The presence of the continuous narrow slit of height $2b_s$, which allows the passage of solvent and low molecular weight solutes but excludes solutes of radius $> b_s$, creates an unstirred layer on the luminal side of the junction strand. Except for the region near the large pores, one can treat this layer using a simple 1-D convective-diffusion approximation in which region 1 is divided into two layers, one with and one without fibers. The solution for the concentration is straightforward. We give only the final results for the concentration in the unstirred layer in region 1:

$$C^{(1f)} = C_L \exp\left[Pe^{(1f)} \frac{b_s}{B} x\right] \qquad 0 < x < L_f \tag{4.43}$$

$$C^{(1w)} = C_L \exp\left[\left(Pe^{(1f)} - Pe^{(1w)}\right) \frac{b_s}{B} L_f\right] \exp\left[Pe^{(1w)} \frac{b_s}{B} x\right] \qquad L_f < x < L_1 \tag{4.44}$$

Here $Pe^{(1w)}$, $Pe^{(1f)}$ are Peclet numbers in the fiber free and fiber filled subregions, which are given by

$$Pe^{(i)} = \frac{2}{3} \frac{\chi^{(i)} \tilde{V}_{01d} \tilde{L}}{\tilde{D}^{(i)}} \qquad i = 1f,\ 1w$$

where

$$\tilde{V}_{01d} = \frac{\tilde{b}_s^2}{2\tilde{\mu}^{(2)}} \frac{\tilde{p}_L - \tilde{p}_A}{\tilde{L}_f \frac{\tilde{\mu}^{(1f)}}{\tilde{\mu}^{(2)}} \frac{\tilde{b}_s^3}{\tilde{B}^3} + (\tilde{L}_1 - \tilde{L}_f) \frac{\tilde{\mu}^{(1w)}}{\tilde{\mu}^{(2)}} \frac{\tilde{b}_s^3}{\tilde{B}^3} + \tilde{L}_2 + \tilde{L}_3 \frac{\tilde{\mu}^{(3)}}{\tilde{\mu}^{(2)}} \frac{\tilde{b}_s^3}{\tilde{B}^3}}$$

Here $\tilde{\mu}^{(1f)}$, $\tilde{\mu}^{(1w)}$ are effective viscosities in the fiber filled and fiber free layers in region 1, $\tilde{\mu}^{(2)}$ is the viscosity in the narrow slit and $\tilde{\mu}^{(3)}$ is the viscosity in region 3.

(F) Approximate 1-D solution for the tissue space and the determination of C_a (t)

As noted earlier in Eq. 4.22f the concentration at the entrance to the far field $C_a(t)$ is a quasi-steady slowly increasing function of time determined by the coupling of the solute transport in regions A and C in Fig. 3.2. In Fu et al. (1995), where only diffusion was considered, it was possible to derive an integral equation for $C_a(t)$ that could be solved analytically. The increase in $C_a(t)$ is related to the integral of the instantaneous total flux Q(t) entering the tissue at each instant in time. For pure diffusion Q(t) can be simply related to the instantaneous value of $C_a(t)$ and an integral equation for $C_a(t)$ obtained without much effort. The author has attempted without success to derive an equivalent integral equation when convection is present. The complexity of the expression for Q(t) has prevented us from doing this analytically. Instead we have developed a rapidly converging iteration procedure that enables us to solve this final step of the coupled boundary value problem linking the cleft and tissue regions numerically. We first consider the boundary value problem for the far field in region C.

Appendix shows that the convective effect of solute transport can be neglected in the tissue space due to the rapid decay of the solvent velocity once it enters the tissue. Furthermore, as discussed earlier in the model description, the estimated time for the filling of the outer region C in Fig. 3.2 is of the order of 60 minutes. On this time scale the early time behavior

($t < 2.5$ sec.) in the intermediate region B can be neglected. Quasi-steady equilibrium has been achieved in region B and the exit jets from the individual junction orifice discontinuities and adjacent clefts (periodically distributed around the periphery of the vessel wall) have merged with each other and have formed a uniform flux along the length of the cleft exit (y direction, see Fig. 3.2). If the mesothelium, top and bottom boundaries of the tissue, is treated as a significantly greater barrier to the solute transport than the tissue space, we can assume that the upper and lower boundaries of the tissue layer are adiabatic and that the far field, defined by region C, can be approximated by one-dimensional, time dependent transport in the x direction. Region C is thus approximated by a 1-D equation averaged across the height of the tissue layer. This dimensionless equation is

$$\frac{\partial C_t}{\partial t} = \frac{\partial^2 C_t}{\partial x_t^2} \tag{4.45}$$

Here $C_t = C_t(t, x_t)$ is the concentration distribution in the tissue space, $t = \tilde{t}\tilde{D}_t/\tilde{L}^2$ is the dimensionless time and $\tilde{D}_t$ the solute diffusivity in the tissue. x_t is the coordinate in the tissue space in the x direction shown in Fig. 3.2. The origin of the far field coordinate x_t is located at a position which is $\sim 5\ \mu$m from the cleft exit which, on the length scale of the intermediate region B describing the spread of the exit jets at the cleft exit, is ∞.

The initial and boundary conditions for Eq. 4.45 are

$$C_t(0, x_t) = 0 \tag{4.46a}$$

$$\frac{\partial C_t(t, 0)}{\partial x_t} = Q(t) \tag{4.46b}$$

$$C_t(t, \infty) = 0 \tag{4.46c}$$

where Q(t) is the total flux integrated along the entire cleft length per unit tissue thickness in the direction of the vessel axis. To obtain an expression for Q(t) we define $Q_c(t)$ as the integral average flux over y from a single periodic unit of cleft length 2D,

$$Q_c(t) = \frac{\int_{-D}^{D} [-\frac{\partial C^{(3)}(t, L, y)}{\partial x} + Pe^{(3)} u_0(L,y) C^{(3)}] \, dy}{2D} \tag{4.47}$$

The relationship between the total flux Q(t) and $Q_c(t)$ is obtained by summing over all the periodic units per unit length of vessel cross-section in the half plane $x > 0$, see Fig. 3.1(b).

$$Q(t) = \frac{\tilde{D}^{(3)}}{\tilde{D}_t} \frac{N_c 2B}{H} Q_c(t) \tag{4.48}$$

In Eq. 4.48 N_c is the number of clefts on the half surface of the vessel, 2B is the width of the cleft and H is the height of the tissue layer.

In Fu et al. (1995) Laplace transforms are used to derive a solution to (4.45) which satisfies boundary and initial conditions (4.46a,b,c). This solution is an integral of the flux Q(t) (see Chapter 3)

$$C_t(t, x_t) = \frac{1}{\sqrt{\pi}} \int_0^t \frac{Q(\tau)}{\sqrt{t - \tau}} \exp[-\frac{x_t^2}{4(t - \tau)}] d\tau \tag{4.49}$$

Eq. 4.49 evaluated at $x_t = 0$ provides an expression for $C_a(t)$

$$C_a(t) = \frac{1}{\sqrt{\pi}} \int_0^t \frac{Q(\tau)}{\sqrt{t - \tau}} d\tau \tag{4.50}$$

in terms of the unknown flux Q(t). Combining (4.47), (4.48) and (4.22f), one obtains a second

relationship between Q(t) and $C_a(t)$

$$Q(t) = \frac{\tilde{D}^{(3)}}{\tilde{D}_t} \frac{N_c B\alpha}{HD} \int_{-D}^{D} [C^{(3)}(t,L,y) - C_a(t)]dy \qquad (4.51)$$

Eqs. 4.50 and 4.51 are now solved by iteration. For the initial guess one assumes that $C_a(t) = 0$ and evaluates the lowest order iteration $Q(t) = Q_0(t)$ using (4.51). This $Q_0(t)$ is now substituted in (4.50) and the lowest order iteration for $C_a(t)$, $C_{a0}(t)$, obtained. For the next iteration one substituted $C_{a0}(t)$ in (4.51) to calculate $Q_1(t)$. $Q_1(t)$ is now substituted in (4.50) and $C_{a1}(t)$ determined. This process is repeated for N iterations until both $C_{aN}(t)$ and $Q_N(t)$ have converged to the desired accuracy.

4.2.4 Model Parameters

1. Cleft and fiber layer geometry

The values of the parameters used to describe the cleft geometry in Figs. 2.1(a),(b) (see Chapter 2) are the same as used in Fu et al. (1994, 1995). These values are: total cleft depth L = 400 nm (Clough and Michel, 1988); height of the cleft 2B = 20 nm (Frokjaer-Jensen, 1991); average large orifice spacing 2D = 2640 nm and opening cross-section, 2b x 2d = 20 x 150 nm (Adamson and Michel, 1993). The predictions in Fu et al. (1994) for the width of the small pore or continuous narrow slit along the junction strand that satisfies the measured values for small ion permeability (Curry, 1979) is $2b_s$ = 1.5 nm. Since 2d = 150 nm is much greater than the thickness of the junction strand, L_2 = 11 nm, and the cleft height, 2B = 20 nm, we shall treat the junction strand as a zero thickness barrier for the case of the large orifice. The average distance from the lumen front to the junction barrier, L_1 = 200 nm (Adamson and Michel, 1993). The depth of the surface fiber layer L_f is ~ 100 nm. This value of L_f was shown in Fu et al. (1994) to provide very good agreement with the measured values

for the hydraulic conductivity and the solute permeability for small and intermediate size solutes up to albumin (7 nm diameter) in frog mesenteric capillaries. The predictions of the model in Fu et al. (1994) also indicate that the fiber layer is ordered and has a gap distance Δ between adjacent fibers of $\sim$ 7 nm, if it is to function as the primary molecular filter. For proteoglycan side chains of 0.6 nm radius, this fiber spacing corresponds to a solid volume fraction S_f = 0.017.

Figs. 3.1(a),(b) (see Chapter 3) show the idealized model geometry for an individually perfused frog mesentery microvessel which was first proposed in Fu et al. (1995). The average measured thickness of the tissue layer is taken to be 25 μm and the characteristic length in the x direction over which measurements are performed is $\sim$200 μm. The average number of the clefts on the half surface of the vessel is 3.5. All values of these geometry parameters are from Adamson et al. (1995).

2. Diffusivity in the tissue space D_t and cleft exit coefficient α

In Fu et al. (1995), the ratio of the diffusivity in the tissue to the free diffusivity $\tilde{D}_t/\tilde{D}_{free}$ for low molecular weight tracer, sodium fluorescein (MW = 367), is determined as 0.3. This value is determined by applying a time dependent model with $\tilde{D}_t/\tilde{D}_{free}$ chosen to obtain an optimum fit for the measured rise in the vessel wall concentration. The accuracy of the value of $\tilde{D}_t$ is then confirmed by comparing the predictions of the model for the spread of the tracer with the detailed time dependent concentration profiles measured in the tissue.

The significant difference between $\tilde{D}_t$ and $\tilde{D}_{free}$ is due to the large collagen content of the tissue. As discussed in Curry (1984) and Weinbaum et al. (1992), the fiber matrix provides both diffusive and steric resistance to the solute transport. The hydrodynamic theory in Weinbaum et al. (1992) predicts that for collagen fibers of radius 40 nm, $\tilde{D}_t/\tilde{D}_{free}$ = 0.3 for

sodium fluorescein when the volume fraction $S_f = 0.48$. These values of a and S_f are then used as input parameters to calculate $\tilde{D}_t/\tilde{D}_{free}$ for the larger HRP molecule. Using the theory in Weinbaum et al. (1992), one finds that $\tilde{D}_t/\tilde{D}_{free} = 0.155$ for HRP tracers (MW = 18,000) of Stokes radius a = 3.0 nm. The free diffusivity $\tilde{D}_{free}$ for HRP in 25°C aqueous solution is 7 x 10^{-7} cm^2/s; thus, $\tilde{D}_t = 1.1 \times 10^{-7}$ cm^2/s. This value of $\tilde{D}_t/\tilde{D}_{free}$ is quite close to the measured value of 0.14 for Dextran-FITC (MW = 19,100, Stokes radius a = 3.12 nm) in the rat mesentery (Fox and Wayland, 1979). Once $\tilde{D}_t/\tilde{D}_{free}$ is determined, the cleft exit coefficient α can be easily obtained from Eq. 4.23. This result for α for HRP is 2.3.

4.3 RESULTS

Pressure Distribution at the Orifice

For mathematical convenience, we introduced a simplifying assumption in Eq. 4.13 for the velocity profile at the periodically distributed large pore orifices. We assumed that, except for a scaling constant η, this profile was well approximated by the velocity profile for an isolated orifice. The continuity of the pressures on the upstream and the downstream side of the junction orifice in the original boundary condition (Eq. 4.12c) was satisfied only globally over the orifice width. In Fig. 4.2, we examine the accuracy of this assumption by comparing the pressure distributions just above and below the orifice opening when the fiber matrix is either present or absent in the cleft. For both cases, one observes that the pressures on the upstream and the downstream side of the orifice are almost constant and identical along the entire orifice width except for a narrow region of order 5 nm near the orifice edge. This provides a strong justification as to the suitability of the assumed form of the velocity profile at the junction orifice in Eq. 4.13, and our assumption that the orifice opening is an isobar or isopotential line.

Peclet Number

Before discussing the concentration distribution, we first examine the anticipated range of Peclet numbers for different size solutes, where P_e is defined in Eq. 4.21. In this expression for P_e, $\tilde{D}^{(i)}$ is obtained from Eq. 4.24, and $\chi^{(i)}=1-\sigma^{(i)}$, $\sigma^{(i)}$ is calculated from Eq. 4.25c. The values of P_e shown in Fig. 4.3 are for a maximum transmural ΔP of 30 cm H_2O.

The solid line in Fig. 4.3 is for a cleft without matrix. When matrix is present on the luminal side of the junction strand there is a discontinuity in P_e across the orifice due to the change in $\tilde{D}^{(i)}$ and $\chi^{(i)}$. The dot-dash-dot line is the Peclet number for solutes on the luminal side, while the dashed line is P_e on the abluminal side of the cleft. One concludes from Fig. 4.3 that for HRP (3.0 nm radius), P_e varies between 1 and 5. Convection should, therefore, play an important role in determining HRP wake profiles.

Concentration Distribution

1. Concentration distribution along the centerline

Figs. 4.4(a) and 4.4(b) show the concentration profiles along the centerline $y = 0$ in the mid-plane $z = 0$ of the cleft from the lumen front, $x = 0$, to the tissue front, $x = L$, for HRP tracers when pressure gradient across the vessel wall is 0 and 30 cm H_2O. Solid lines are for the cleft without matrix and dashed lines for the cleft with matrix on its luminal side. The depth of the fiber layer $L_f = 100$ nm $< L_1 = 200$ nm, the depth of the wide portion of the cleft on the luminal side. Note that while the magnitude of the concentration drop on the tissue side of the junction strand is accurately predicted by the model, the detailed profiles in region 1 are not preserved since the resistance of the matrix is distributed over the entire depth L_1 rather than confined to the depth L_f, Eqs. 4.24 and 4.25.

In Fig. 4.4(a) the HRP concentration profiles are plotted for $\Delta P = 0$ for $t = 0$, 30, and

60 seconds. For this pure diffusion transport, the time varying solute concentration in the extravascular tissue space $C_a(t)$, which appears in cleft exit condition Eq. 4.22f, has only a small influence on the concentration distribution along the center line in the cleft since the curves in Fig. 4.4(a) do not change significantly with time when matrix is either present or absent. When matrix is present on the luminal side, there is a nearly linear drop in concentration along the cleft center line from the lumen front, $x = 0$, to the junction orifice, $x = L_1$. In contrast, one observes in Fig. 4.4(b) that when $\Delta P = 30$ cm H_2O, $C_a(t)$ increases significantly with time, especially for the cleft without matrix. When the matrix is present on the luminal side of the junction strand there is a large non-linear decreasing gradient in concentration upstream of the opening and a low HRP concentration in the wake. This important observation and the fact that the model does not preserve the details of the upstream profiles will be discussed more fully later.

2. Lateral spreading of HRP tracers

Figs. 4.5(a),(b) show the concentration profiles for HRP on the front and back sides of the junction barrier. The solid curves in Figs. 4.5(a),(b) are for a cleft without fiber matrix and dashed curves are for a cleft in which there is matrix in the luminal side of the cleft. Again, the concentration profiles on the upstream side of the junction strand are correct in magnitude, but inaccurate in their shape because of the distributed resistance approximation that has been used in region 1. In Fig. 4.5(a), where the pressure gradient $\Delta P = 0$, the solutions are nearly symmetric across the junction strand when there is no matrix in the cleft, but there is a large asymmetry when matrix is present on the luminal side. In contrast to Fig. 4.5(a), where $\Delta P =$ 30 cm H_2O in Fig. 4.5(b), there is a large asymmetry due to convection even in the absence of the fiber matrix. In addition, the concentration profiles on the back side of the junction

barrier exhibit a more significant change with time especially for the case where there is no matrix in the cleft. If the detectable concentration level for HRP is 30% of the perfusate concentration, the width of the observable region of the lateral spreading of HRP tracers in the abluminal side of the junction strand when $\Delta P = 30$ cm H_2O is 335 x 2, 475 x 2, 570 x 2 nm at $t = 0$, 30, 60 sec., which is 4.5, 6.3, and 7.6 times the pore width of 150 nm, when the matrix is absent. However, if matrix is present on the luminal side of the cleft, the width of the detectable region is greatly reduced and the apparent wake width is only 1.2, 1.3, and 1.5 times the pore width at $t = 0$, 30, 60 sec.. On the other hand, if $\Delta P = 0$ and the threshold for detection is 30% there would be no observable wakes on the tissue side of the junction strand since $C < 0.2$ everywhere.

3. Concentration distribution along the cleft exit

The fundamental improvement in this model is that boundary condition Eq. 4.22f is used for the concentration field at the cleft exit instead of the vanishing tissue concentration exit condition used in previous models. In Figs. 4.6(a),(b), we plot these predicted non-zero cleft exit concentration profiles as a function of distance from the center line of the cleft for $t = 0$, 30 and 60 seconds. $\Delta P = 0$ in Fig. 4.6(a) and 30 cm H_2O in Fig. 4.6(b). Solid lines are for a cleft without matrix and dashed lines for a cleft with matrix on its luminal side. Fig. 4.6(a) indicates that if the detectable HRP threshold is 0.3, no HRP wake will be observed to penetrate to the cleft exit. for a cleft with or without matrix when $\Delta P = 0$. In contrast, if convection is present, $\Delta P = 30$ cm H_2O, Fig. 4.6(b), there is a substantial increase in the HRP tracer concentration at the cleft exit. The width of the visible region is 245 x 2, 385 x 2, and 485 x 2 nm at $t = 0$, 30, and 60 seconds when there is no fiber matrix in the cleft. But for the case where fiber matrix is present, the wake induced by the convection at the cleft exit is still below

the level of visibility although the concentration levels are times the $\Delta P = 0$ results in Fig. 4.6(a).

4. Ultrafiltration through small pores

Fig. 4.7 shows the HRP concentration distribution along the centerline on the luminal side of the junctional barrier when there is ultrafiltration. The 1.5 nm wide narrow slit allows only the passage of water or solutes of diameter < 1.5 nm and would have a reflection coefficient of unity for HRP molecules (3.0 nm in radius). For pure diffusion, the concentration is uniform everywhere on the luminal side for a cleft with or without fibers. When $\Delta P = 30$ cm H_2O, there is a linear increase in C when fiber matrix entrance layer is absent. The total increase from the cleft entrance to the junction barrier is less than 2.5 percent, but there is a 7.5 percent increase when matrix is present. In addition, the increase is steeper in the fiber filled region than fiber free region. The presence of the matrix increases the Peclet number nearly ten fold due to the decrease in the diffusion coefficient, whereas there is little decrease in hydraulic conductivity since this small slit provides a much greater portion of the hydraulic resistance than the matrix. A significant unstirred filter layer for larger molecules will only be observed if a matrix is present on the luminal side of the junction barrier.

4.4 DISCUSSION

The results presented in Figs. 4.4-4.7 can be used to develop new experimental strategies for the design of experiments to determine the distribution of fiber matrix components and the location of structural elements that form the primary molecular sieve.

While the wake of low molecular weight tracers can help us determine the size and frequency of the junction pores as proposed in Fu et al. (1995), the important insights into the

distribution of matrix components and the effect of filtration can be obtained by examining the concentration profiles for a larger tracer molecule, such as HRP. In contrast to low molecular weight tracers, large changes in HRP concentration will occur across the cleft in response to a superimposed convective flow, whether or not matrix components are present for the 150 nm wide break. In Figs. 4.4(a),(b) it is observed that there are striking differences in the concentration distribution of HRP for the 150 nm break, depending upon whether matrix components are present on the luminal side of the cleft. These differences are particularly evident at high filtration flow rates, $\Delta P = 30$ cm H_2O. One observes that if no matrix components are present at high flow rates, HRP will label the cleft to the tissue side and the exit concentration should be significantly above threshold in the vicinity of the large breaks. In contrast, if matrix is present, there will be a large drop in concentration in front of the orifice opening and very little tracer will be detected on the abluminal side of the cleft. Thus the only condition where HRP is likely to be detected on the abluminal side of the cleft is in the case where matrix is absent. It is important to note that, for pure diffusion, the concentration of HRP on the abluminal side of the junctional strand and at the cleft exit will be significantly reduced if matrix is present (see Figs. 4.5(a) and 4.6(a)). The presence of matrix is best indicated by the apparent inability of HRP to penetrate the cleft in a region where there appears to be a break in the junctional barrier. This important unintuitive result is in sharp contrast to the low molecular weight tracer labeling described in Fu et al. (1995) where a distinct wake is predicted downstream of a junction strand discontinuity.

At present, no experiments have been specifically designed to investigate HRP wakes under well defined conditions of high and low Peclet number. However, because most experiments to study HRP distribution have been performed without albumin in the perfusate (which tends to increase filtration rate) and with microvascular pressure elevated to carry out

perfusion fixation, it is likely that experimental conditions approach those expected at high Peclet numbers. It is notable that under these conditions there is little likelihood of detecting HRP tracer on the abluminal side of the junctional strand even at the location of a large orifice junctional strand discontinuity if there is matrix layer on the luminal side of the junction strand. In fact, when this matrix layer is present there is very little difference in the HRP distribution at the cleft exit when there is a large orifice break or if the strand is continuous. In both cases HRP might be below the level of detectability in the entire region 3 on the abluminal side of the junction. Thus, the absence of HRP labeling on the abluminal side of the junction strand cannot be taken as definitive evidence that there are no breaks in the junctional strand if a sieving matrix is present on the luminal side of the junction strand. This observation places important limitations on the interpretation of all studies using large molecular weight tracers that have been performed to date.

It is evident from Fig. 4.5(b) that there should be a distinct difference in HRP labeling on the lumen side of the junction barrier depending on whether or not sieving matrix components are present in the wide part of the cleft on the lumen side of the junction strand. Without matrix one should observe a nearly uniform labeling of HRP on the lumen side of the junction strand at high filtration flows even in front of a large orifice break. In contrast, if matrix is present in the upstream cleft there will be a sharp drop in concentration upstream of a large orifice opening. The details of these upstream profiles require a more sophisticated model than presently used in which separate solutions are obtained for both fiber and fiber free layers in region 1.

An issue which is not specifically addressed in this paper is the effect of sieving at cleft entrance on the appearance of tracer concentrations in the junction relative to tracer concentrations in the lumen of the microvessel. Partitioning of the solute should result in a step

change in concentration between the tracer concentration in the lumen and tracer within a matrix at the cleft entrance. This effect was not included in the present paper because of the additional mathematical complexity associated with describing the transport of tracer across such a discontinuity. Our solutions for HRP describe gradients relative to the concentration in the available volume just inside the cleft. This simplification does not significantly reduce the usefulness of the solutions presented herein, because, in practice the interpretation of tracer distribution along a cleft, is based on changes relative to that at the entrance of the cleft rather than changes relative to those in the bulk of the microvessel, since the tracer is not usually retained in the vessel lumen. The steric exclusion of low molecular weight tracers by matrix components is small, but this correction for HRP is significant and should be considered in calculating the solution concentration at the cleft entrance.

Finally, the presence of a tiny continuous slit is not easily detected in ultrafiltration experiments since the magnitude of the unstirred layer in the wide part of the cleft is likely to be small even if matrix is present upstream of the junction strand barrier, see Fig. 4.7. The best indication of such pores would appear to be the labeling of a small sized tracer on the downstream side of the junction barrier in a region where the opposing junction strands appear tight. In the simpler 1-D convective-diffusion model the fiber and fiber free layers could be treated separately and, as one observes in Fig. 4.7 there is a discontinuity in concentration gradient at $x = L_f$, the trailing edge of the matrix layer. The magnitude of this discontinuity in gradient would change in the vicinity of a large orifice break.

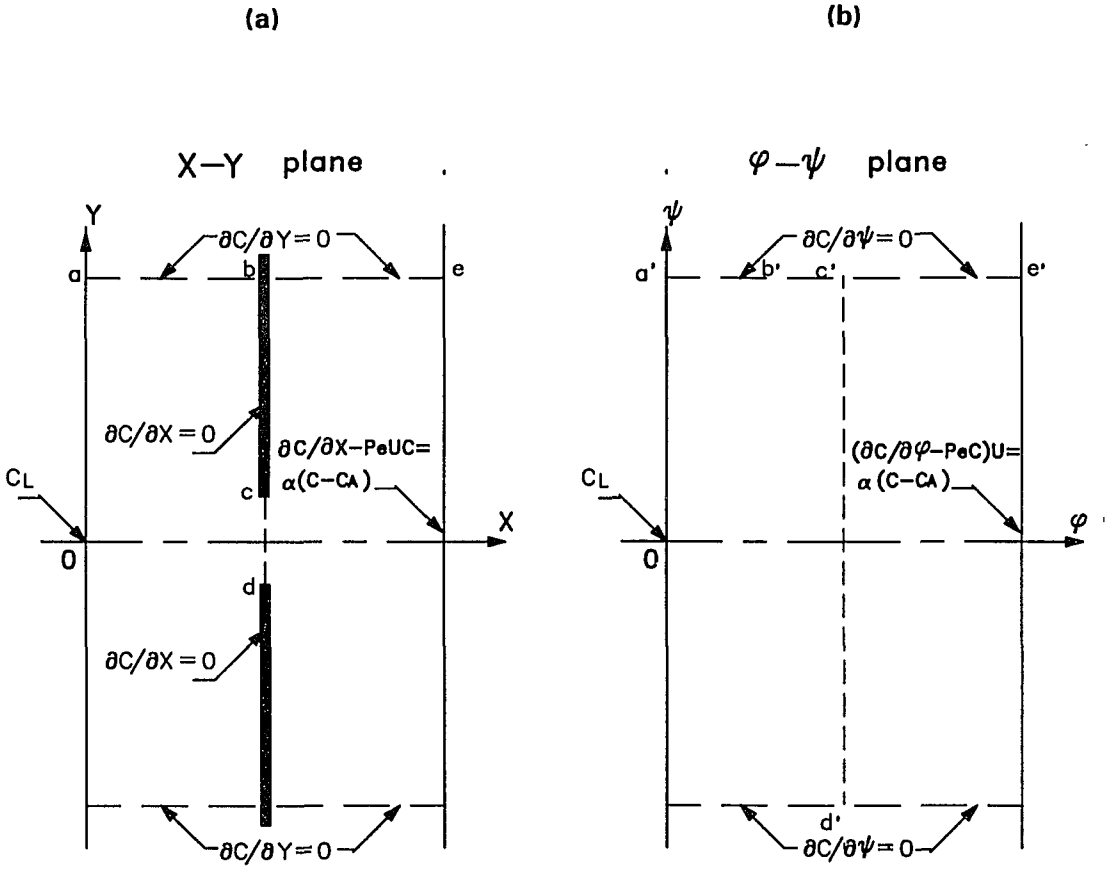

Fig. 4.1 **(a)** The structure of the cleft in the z = 0 plane and the boundary conditions for the concentration distribution. on the lumen front: x = 0, -D < y < D, concentration C_L is constant and on the tissue front, the solute flux is assumed to be proportional to the concentration difference between those at the cleft exit and in the tissue. **(b)** The corresponding boundaries and boundary conditions in the ϕ, ψ plane for concentration distribution, which are transferred from the physical x, y plane shown in (a).

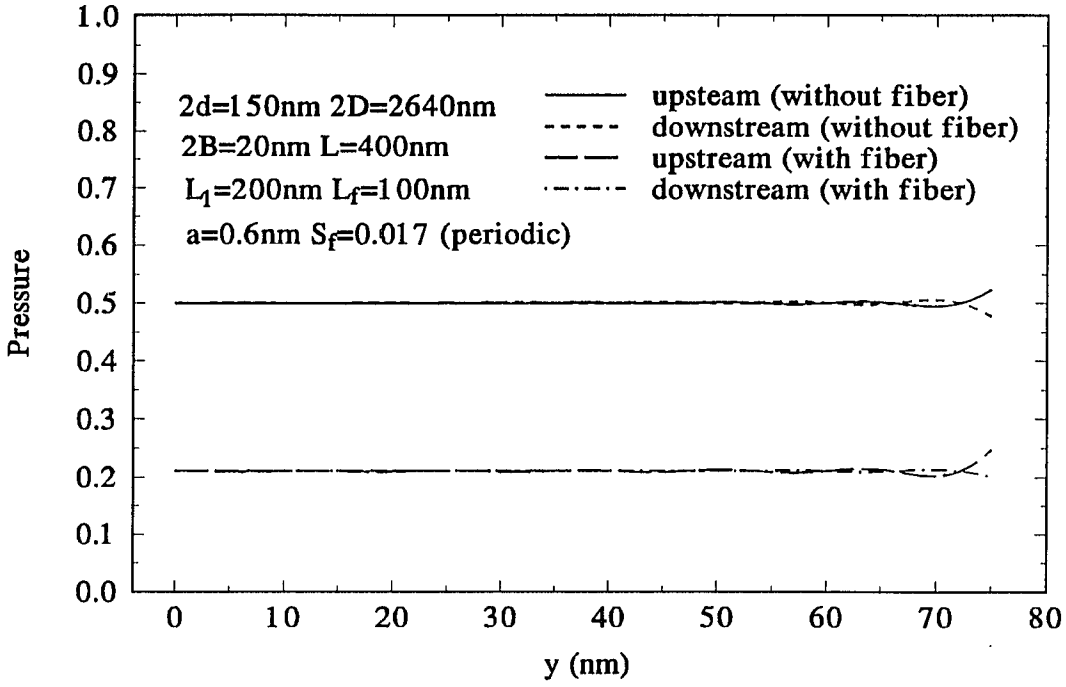

Fig. 4.2 Pressure profiles on the upstream and downstream sides of 150 nm junction orifice when the cleft without matrix and matrix in the luminal side. a is the fiber radius, S_f is the fiber solid volume and L_f is the depth of the fiber entrance layer.

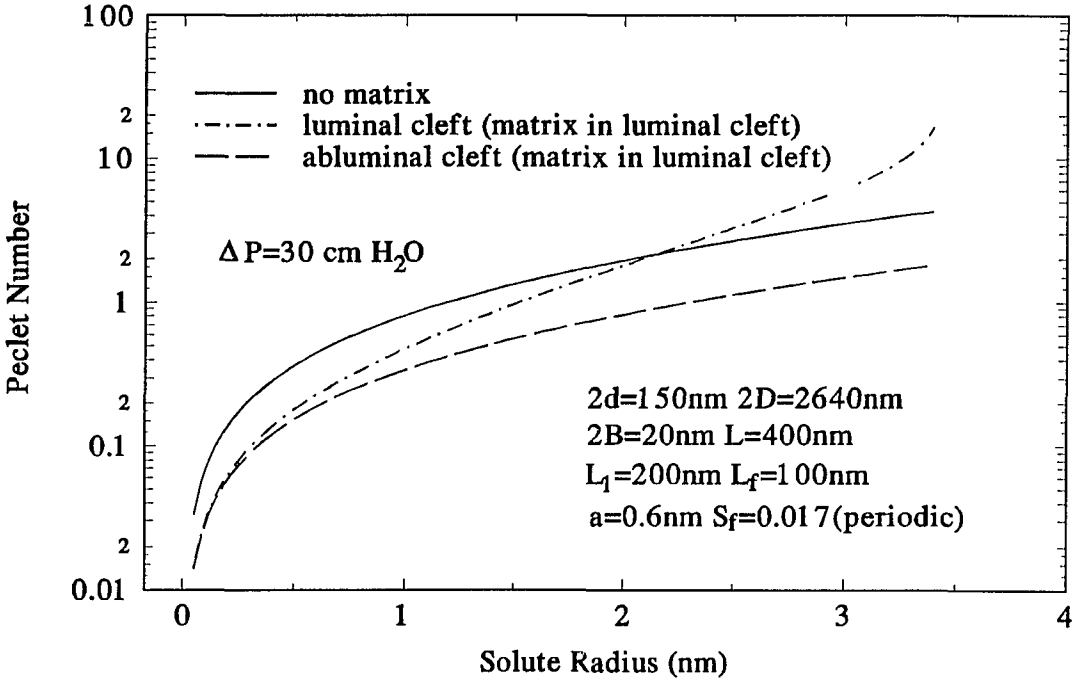

Fig. 4.3 Peclet Number as a function of solute radius. ΔP is the pressure gradient across the vessel wall. (-) in the cleft without matrix; (.-.) in the luminal side and (--) in the abluminal side when the matrix fills 100 nm of the cleft in the luminal side.

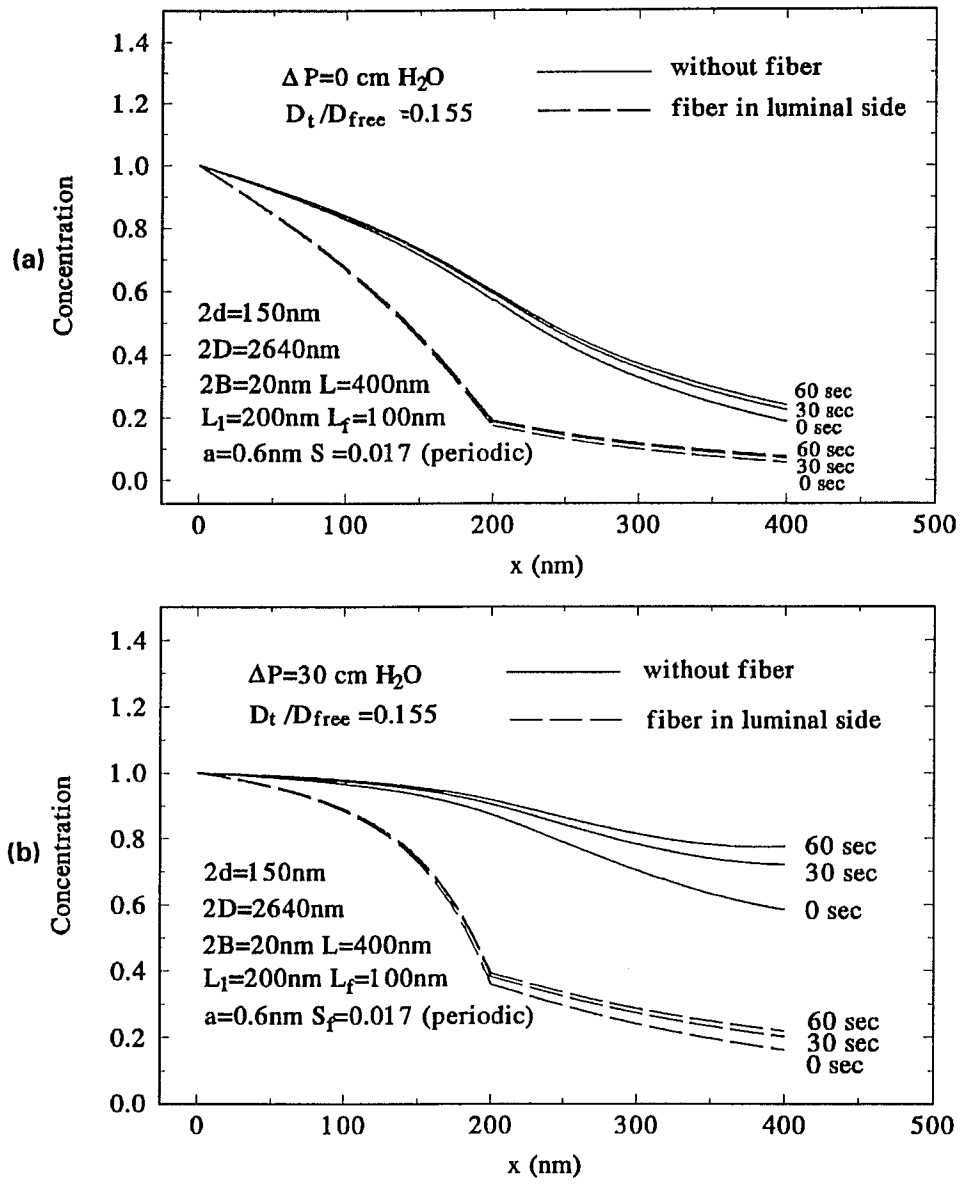

Fig. 4.4 Concentration distribution along the center line in the middle plane of the cleft from the lumen to the tissue at different time instant. (-) in the cleft without matrix and (--) matrix fills 100 nm of the cleft on the luminal side. **(a)** pressure gradient across the vessel wall $\Delta P = 0$; **(b)** $\Delta P = 30$ cm H_2O.

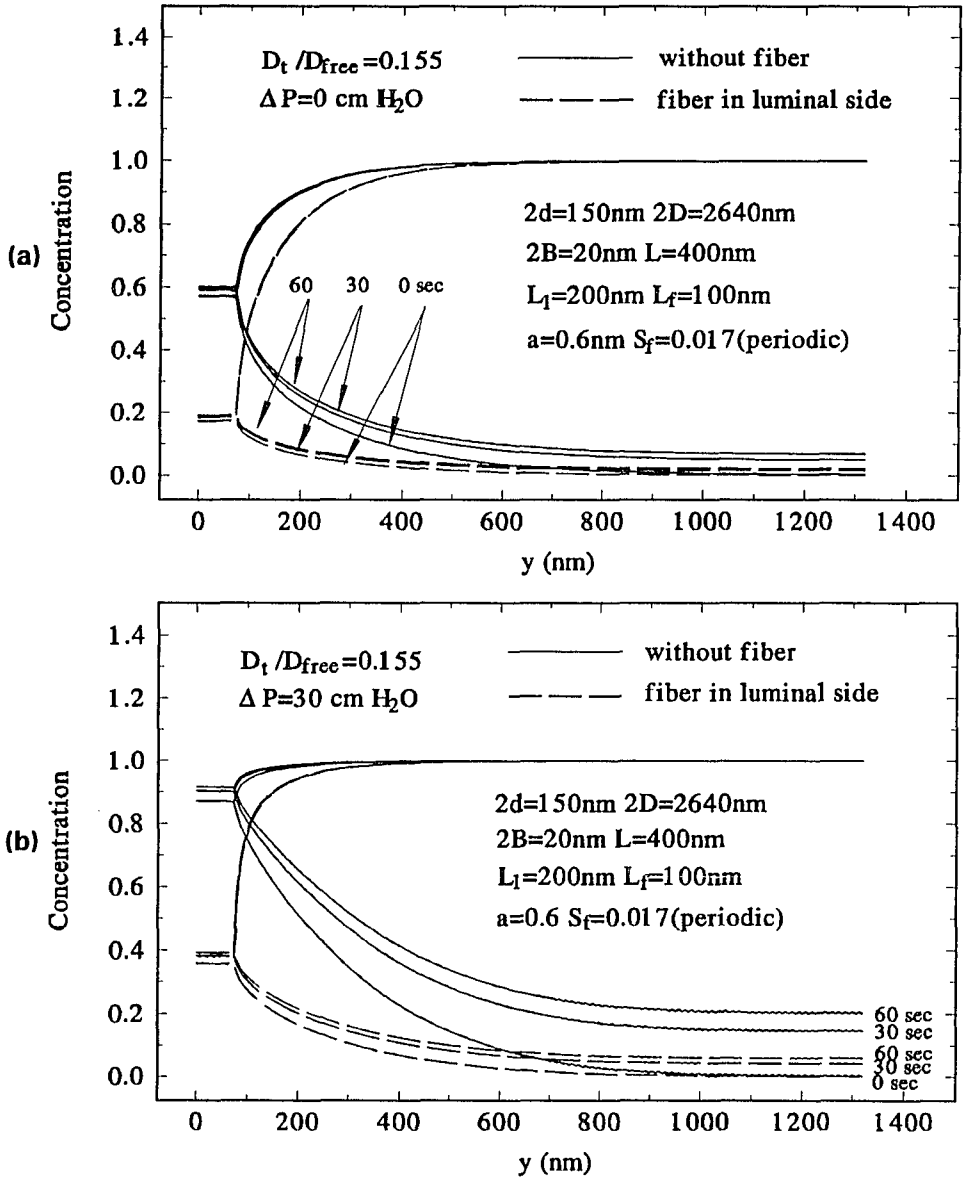

Fig. 4.5 The lateral spreading of HRP tracers on the luminal and abluminal sides of the junction barrier at different time instant. (-) in the cleft without matrix and (--) matrix fills 100 nm of the cleft on the luminal side. **(a)** pressure gradient across the vessel wall $\Delta P = 0$; **(b)** $\Delta P = 30$ cm H_2O.

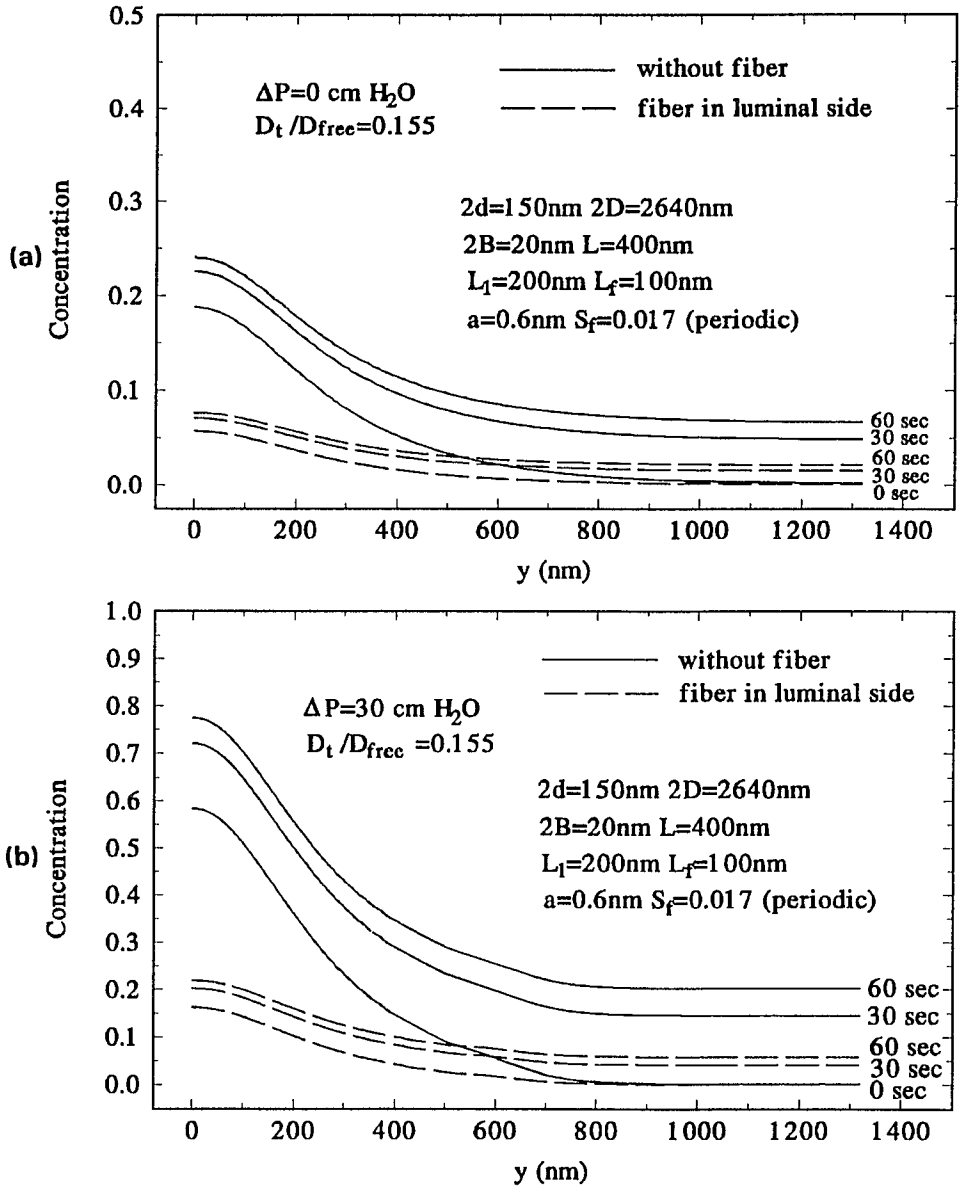

Fig. 4.6 Concentration distribution at the cleft exit at different time instant. (-) in the cleft without matrix and (--) matrix fills 100 nm of the cleft on the luminal side. **(a)** pressure gradient across the vessel wall ΔP = 0; **(b)** ΔP = 30 cm H_2O.

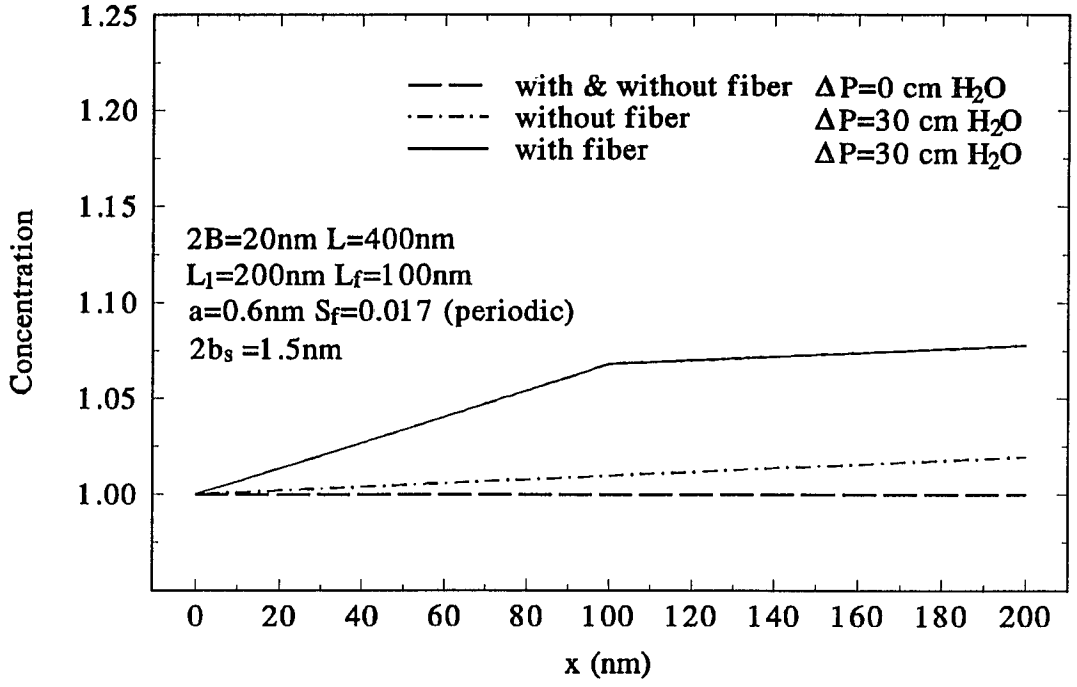

Fig. 4.7 Ultrafiltration of HRP tracers through 1.5 nm wide continuous narrow slit along the junction strand. (--) pure diffusion in the cleft with and without matrix; (.-.) in the cleft without matrix, ΔP = 30 cm H_2O; (-) matrix fills 100 nm of the cleft in the luminal side, ΔP = 30 cm H_2O.

CHAPTER 5

SUMMARY

SUMMARY AND FUTURE STUDIES

The recent serial section electron microscopic studies by Adamson and Michel (1993) of frog mesentery have revealed that the large pores in the junction strand of the interendothelial cleft are widely separated 150 nm wide orifice-like breaks whose gap height 20 nm is the same as the wide part of the cleft. A translucent narrow continuous ~ 2 nm slit along the outer leaflets in the tight junction was also revealed on a tilting stage in their study. In chapter 2 of this study a modified version of the model in Weinbaum et al. (1992) is first developed in which this orifice structure is explored in combination with a random or ordered fiber matrix layer that is both at the luminal surface and occupies a fraction of the wide part of the cleft. This basic orifice model predicts that for the measured L_p to be achieved the fiber layer must be confined to a relatively narrow region at the entrance to the cleft where it serves as the primary molecular filter. The predicted thickness of this entrance layer is roughly 100 nm for a periodic array, and about one quarter of this thickness for a random array, if the spacing between adjacent junction discontinuities is in the range of the experimental data in Adamson and Michel (1993). The observed thickness of the surface glycocalyx portion of this layer is only about 60 nm (Adamson and Clough, 1992), suggesting that the matrix penetrates almost an equivalent depth into the wide portion of the cleft.

The present model with large orifice breaks provides a much better fit of the permeability data for intermediate size solutes between 1 and 2 nm radius than the previous model in Weinbaum et al. (1992) where the junction strand breaks were treated as finite depth circular or rectangular pores, but like the previous model significantly underestimates P for

small ions of radius < 0.5 nm by a factor > 3. However, it is shown that if a small frequent pore of 1.5 nm radius with characteristic spacing comparable to the diameter of the junction proteins or a continuous narrow slit of approximately 1.5 to 2.3 nm gap height is also present in the continuous part of the junction strand, small ion permeability can also be satisfied. The 1.5 nm radius pore does not significantly change L_p, whereas the continuous narrow slit provides a contribution to L_p that is comparable to, or in the case of the 2.3 nm slit, greater than the widely spaced 150 nm orifices. Thus, for the narrow slit the contribution to L_p from the orifices can be as low as 1.0×10^{-7} cm/s/cm H_2O and it is also possible to satisfy the 2.5 fold increase in L_p that occurs when the matrix is enzymatically removed from the luminal side of the cleft, Adamson (1990).

In chapter 3, we developed a time dependent diffusion model for analyzing the concentration profiles of low molecular weight tracers in the interendothelial clefts of the capillary wall, which takes into account the three-dimensional, time dependent filling of the surrounding tissue space. The model provides a critical connecting link between two methods to investigate transvascular exchange: electron microscopic experiments to study the time dependent wake formed by low molecular weight tracers (such as lanthanum nitrate) on the tissue side of the junction strand discontinuities in the inter-endothelial cleft of frog mesentery capillaries (Adamson and Michel, 1993) and confocal microscope experiments to measure the spread of low molecular weight fluorescent tracers in the tissue space surrounding these microvessels (Adamson et al., 1995). We show that the interpretation of the presence of tracer as an all-or-none indication of a pathway across the junctional strand is likely to be incorrect for small solutes. Large pore pathways in which the local tracer flux densities are high reach a threshold concentration for detection and are likely to be detected after relatively short perfusion times whereas distributed small pore pathways may not be detected until the tissue

concentrations surrounding the entire vessel approach threshold concentrations. The analysis using this approach supports the hypothesis advanced in chapter 2 that the principal pathways for water and solutes < 1.5 nm diameter across the interendothelial cleft may be different and suggests new experiments to test this hypothesis.

In chapter 4 of the present study, a time dependent convective-diffusion model is developed to analyze the two-dimensional wake formed by the spreading of high molecular weight tracers (such as HRP) downstream of junction strand discontinuities in the interendothelial cleft and the standing gradient flow upstream of the junction strand barrier in the fiber entrance region of the cleft. This model, in conjunction with related experiments which are currently in progress, is designed to evaluate the relative contribution of structures associated with the junctional strand and the fiber matrix to the molecular filter at the microvessel wall. In contrast to low molecular weight tracers, large changes in HRP concentration will occur across the cleft in response to a superimposed convective flow. It is observed that there are striking differences in the concentration distribution of HRP for the large 150 nm breaks, depending upon whether or not matrix components are present on the luminal side of the cleft. If no matrix components are present at high flow rates, HRP will label the cleft to the tissue side and the exit concentration should be significantly above threshold. In contrast, if matrix is present, there will be a large drop in concentration in front of the orifice opening and low levels of tracer will be detected on the abluminal side of the cleft. The presence of matrix is thus best indicated by the apparent inability of HRP to penetrate the cleft in a region where there appears to be a break in the junctional barrier. Thus, the lack of HRP tracer on the abluminal side of the junction strand cannot be taken as definitive evidence that there are no breaks in the junctional strand. This observation places important limitations on the interpretation of all studies using large molecular weight tracers that have been performed

to date. The second prediction is that there should be a distinct difference in HRP labeling on the lumen side of the junction barrier depending on whether or not sieving matrix components are present in the wide part of the cleft on the lumen side of the junction strand. Without matrix one should observe a nearly uniform labeling of HRP on the lumen side of the junction strand at high filtration flows even in front of a large orifice break. In contrast, if matrix is present in the upstream cleft there will be a sharp drop in concentration upstream of a large orifice opening.

Two important simplifications have been used in the present models. First, we have assumed an average effective viscosity, diffusivity and retardation coefficient for the region on the lumen side of the junction strand, which is an average of the properties in the fiber layer and in the fiber free subregion. This approximation reduces a complicated three region boundary value problem to an analytically solvable two region problem, but sacrifices the detailed concentration profiles in the fiber entrance layer where the molecular selectivity occurs. Numerical methods are probably required to more adequately treat the fiber entrance layer. This is particularly important for the model in Chapter 4 for the convective-diffusive transport of HRP.

Second, the present theory for the effective solute diffusivity and the reflection coefficient in a restricted channel filled with matrix does not properly take into account the near field interaction between the solute and the fibers. A more rigorous theory which can describe the hydrodynamic interaction of a finite size solute with ordered matrix fibers in the entrance region of the cleft is needed to more properly describe the sieving of large solutes in the fiber entrance region of the cleft .

Chapter 2 has appeared as a paper entitled " A Junction-orifice-fiber entrance layer

model for capillary permeability: application to frog mesenteric capillaries" in the Journal of Biomechanical Engineering, **116**, 502-513. Chapter 3 has been accepted for publication in the American Journal of Physiology. The title of this paper is "A diffusion wake model for tracer ultrastructure-permeability studies in microvessels". The material in Chapter 4 will shortly be submitted for publication in Microvascular Research.

APPENDIX

1. APPENDIX IN CHAPTER 2

The dimensionless pressure and the length can be defined as

$$\bar{p}(\bar{x}, \bar{y}) = \frac{p(x, y) - p_A}{p_L - p_A}, \qquad \bar{x} = \frac{x}{L}, \qquad \bar{y} = \frac{y}{L} \tag{2.A1}$$

The solution for a Hele-Shaw flow through a single orifice in a channel of depth L is significantly simplified when the junction barrier is located in the middle of the cleft because of the linearity of the Hele-Shaw flow equation (2.3) in the paper and the symmetric geometry about the junction barrier $\bar{x} = 1/2$. Therefore the potential pressure distribution in region 3 has the following relationship with that in region 1

$$\bar{p}^{(3)}(\bar{x}, \bar{y}) = C_1[1 - \bar{p}^{(1)}(1 - \bar{x}, \bar{y})] \qquad \frac{1}{2} \le \bar{x} \le 1, \qquad \bar{y} \ge 0 \tag{2.A2}$$

At the orifice, the pressure and the velocity should be continuous

$$\bar{p}^{(1)} = \bar{p}^{(3)} \tag{2.A3}$$

$$-\frac{B^2}{2\mu^{(1)}}\frac{\partial \bar{p}^{(1)}}{\partial x} = -\frac{B^2}{2\mu^{(3)}}\frac{\partial \bar{p}^{(3)}}{\partial x} \tag{2.A4}$$

$$-\frac{B^2}{2\mu^{(1)}}\frac{\partial \bar{p}^{(1)}}{\partial y} = -\frac{B^2}{2\mu^{(3)}}\frac{\partial \bar{p}^{(3)}}{\partial y} \tag{2.A5}$$

Substituting (2.A2) into (2.A4), the constant C_1 is obtained as

$$C_1 = \frac{\mu^{(3)}}{\mu^{(1)}} \tag{2.A6}$$

One can also show from (2.A2) and (2.A5) that

$$\frac{\partial \bar{p}^{(1)}}{\partial y} = \frac{\partial \bar{p}^{(3)}}{\partial y} = 0 \qquad \bar{x} = \frac{1}{2}, \quad 0 \le \bar{y} \le \frac{d}{L} \tag{2.A7}$$

(2.A7) indicates that the pressure is uniform along the orifice and the value at the orifice can be obtained from (2.A2), (2.A3) and (2.A6)

$$p^{(2)} = \frac{\mu^{(3)} p_L + \mu^{(1)} p_A}{\mu^{(1)} + \mu^{(3)}} \qquad \bar{x} = \frac{1}{2}, \qquad 0 \le \bar{y} \le \frac{d}{L} \tag{2.A8}$$

2. APPENDIX IN CHAPTER 3

Appendix A

This appendix gives the expressions for the coefficients in Eq. 3.13. For region 1:

$$a^{(1)}(t) = \frac{C_L - C_a(t)}{(\frac{D_c^{(1)}}{D_c^{(3)}} - 1)L_1 + (\frac{D_c^{(1)}}{D_c^{(3)}} - \frac{D_c^{(1)}}{D_c^{(2)}}\frac{b}{b_s})L_2 - \frac{D_c^{(1)}}{D_c^{(3)}}(L + \frac{1}{\alpha})}$$

$$b^{(1)}(t) = C_L,$$

For region 2:

$$a^{(2)}(t) = \frac{C_L - C_a(t)}{(\frac{D_c^{(2)}}{D_c^{(3)}} - \frac{D_c^{(2)}}{D_c^{(1)}})\frac{b_s}{b}L_1 + (\frac{D_c^{(2)}}{D_C^{(3)}}\frac{b_s}{b} - 1)L_2 - \frac{D_c^{(2)}}{D_C^{(3)}}\frac{b_s}{b}(L + \frac{1}{\alpha})}$$

$$b^{(2)}(t) = \frac{(\frac{D_c^{(2)}}{D_c^{(1)}}\frac{b_s}{b} - 1)[C_L - C_a(t)]}{(\frac{D_c^{(2)}}{D_c^{(3)}} - \frac{D_c^{(2)}}{D_c^{(1)}})\frac{b_s}{b} + (\frac{D_c^{(2)}}{D_C^{(3)}}\frac{b_s}{b} - 1)\frac{L_2}{L_1} - \frac{D_c^{(2)}}{D_C^{(3)}}\frac{b_s}{b}(\frac{L}{L_1} + \frac{1}{L_1\alpha})} + C_L,$$

For region 3

$$a^{(3)}(t) = \frac{C_L - C_a(t)}{(1 - \frac{D_c^{(3)}}{D_c^{(1)}})L_1 + (1 - \frac{D_c^{(3)}}{D_c^{(2)}}\frac{b}{b_s})L_2 - (L + \frac{1}{\alpha})}$$

$$b^{(3)}(t) = C_a(t) - \frac{C_L - C_a(t)}{(1 - \frac{D_c^{(3)}}{D_c^{(1)}})\frac{\alpha L_1}{1+\alpha L} + (1 - \frac{D_c^{(3)}}{D_c^{(2)}}\frac{b}{b_s})\frac{\alpha L_2}{1+\alpha L} - 1}$$

Appendix B

The solution of Eq. 3.22 subject to initial and boundary conditions Eqs. 3.23a-c can be obtained by introducing the similarity variable

$$Y = \frac{r}{\sqrt{4D_t t}} \tag{3.B1}$$

into the partial differential equation Eq. 3.22. The governing equation 3.22 is transformed into an ordinary differential equation in the new variable Y

$$\frac{d^2C_t}{dY^2} + \frac{(1 + 2Y^2)}{Y}\frac{dC_t}{dY} = 0. \tag{3.B2}$$

The initial and boundary conditions 3.23a-c become

$$\frac{dC_t}{dY} = \frac{2q}{\pi B}\sqrt{\frac{t}{D_t}} \qquad Y = \frac{B}{\sqrt{4D_t t}} \tag{3.B3a}$$

$$C_t = C_a \qquad Y = \infty \tag{3.B3b}$$

The solution of Eq. 3.B2 subject to boundary conditions Eqs. 3.B3a, b is

$$C_t(Y) = \frac{q}{2\pi D_t}\exp(\frac{B^2}{4D_t t})[-Ei(-Y)] + C_a \qquad (3.B4)$$

Eq. 3.B4 is the result in Eq. 3.24 in the main text. Ei(Y), the exponential integral function,

$$-Ei(-Y) = \int_1^\infty \frac{e^{-Y\tau}}{\tau} d\tau \qquad (Y > 0) \qquad (3.B5)$$

can be computed from the formula

$$E_i(Y) = \Gamma + \ln(-Y) + \sum_{k=1}^{\infty} \frac{Y^k}{k.k!} \qquad (Y < 0) \qquad (3.B6)$$

where $\Gamma = 0.5772...$ is Euler's constant.

Appendix C

This appendix summaries the analytical solution of Eq. 3.30 subject to boundary and initial conditions 3.31a-c for the concentration distribution in the far field $C_t(t,x_t)$. Following the method used in (Weinbaum et al.,1992), we take the Laplace transform of Eqs. 3.30 and 3.31a-c

$$D_t \frac{\partial^2 \hat{C}_t}{\partial x_t^2} = s\hat{c}_t \qquad (3.C1)$$

$$D_t \frac{\partial \hat{C}_t(s, 0)}{\partial x_t} = -\hat{Q}(s) \qquad (3.C2a)$$

$$\hat{C}_t(s, \infty) = 0 \qquad (3.C2b)$$

where the carot (^) indicates the Laplace transform

$$\hat{C}_t(s, x_t) = \int_0^\infty C_t(t, x_t) e^{-st} dt \tag{3.C3}$$

and s is the transform variable. The solution of Eq. 3.C1 subject to boundary conditions Eqs. 3.C2a, b is

$$\hat{C}_t(s, x_t) = \frac{\hat{Q}(s)}{\sqrt{D_t s}} \exp\left(-\sqrt{\frac{s}{D_t}} x_t\right) \tag{3.C4}$$

The inverse Laplace transform of Eq. 3.C4 is given in (Abramowitz and Stegun, 1970). This inversion yields the integral equation Eq. 3.36 in the main text.

Appendix D

In this appendix, we give the key steps in the solution of the integral equation 3.38 for Q(t) and the evaluation of Eq. 3.36 for $C_t(t,x_t)$.

Eq. 3.38 is readily solved in transform space by evaluating the Laplace integral if its right hand side. This transform solution is

$$\hat{Q}(s) = \frac{C_L \sqrt{D_t} \omega}{\sqrt{s}(\sqrt{s} + \omega)} \tag{3.D1}$$

where ω is given by Eq. 3.40 in main text. Substituting (3.D1) into (3.C4), one obtains

$$\hat{C}_t(s, x_t) = \frac{C_L \omega}{s(\sqrt{s} + \omega)} \exp\left(-\sqrt{\frac{s}{D_t}} x_t\right) \tag{3.D2}$$

The inverse Laplace transformations of (3.D1) and (3.D2) are found in (Abramowitz and Stegun, 1970). These inversions lead to results in Eqs. 3.39 and 3.42 in main text.

4. APPENDIX IN CHAPTER 4

In this appendix a simplified model is developed for intermediate region B, the 2-5 μm region shown in Fig. 3.2 surrounding each cleft exit. This model is then used to determine the cleft exit coefficient α appearing in Eqs. 4.2, 4.22f and 4.37e. The distance between the neighboring clefts in the vessel wall is ~ 10 μm (Adamson, 1994). The gap height of the wide part of the cleft is merely 20 nm. If one were a tiny observer in the tissue space looking at the cleft exit, one would see a line source of variable strength along the length of the cleft exit in the y direction. On the intermediate length scale of the cylindrical region of 5 μm radius originating at the cleft exit (r = 0, see Fig. 3.2), we can treat the solute flux at the cleft exit as a time and spatially varying line source, that spreads radially into a semi-infinite tissue space. Since axial gradients in the y direction near the cleft exit are much smaller than radial gradients, the governing equation, initial and boundary conditions describing the radial decay of this jet are:

$$\frac{\partial C_t}{\partial t} = \frac{\partial^2 C_t}{\partial r^2} + \frac{1}{r}\frac{\partial C_t}{\partial r} - Pe^{(t)} v_r \frac{\partial C_t}{\partial r} \tag{4.A1}$$

$$C_t(0, r) = C_a(0) \tag{4.A2a}$$

$$\left[-\frac{\partial C_t}{\partial r} + Pe^{(t)} v_r C_t\right] \pi B = q \qquad r = B \tag{4.A2b}$$

$$C_t(t, \infty) = C_a(t) \tag{4.A2c}$$

where q, the source strength per unit length, varies with both y and t. As discussed in the model description in the main text, the characteristic diffusion time, $\tilde{L}_B^2/\tilde{D}_t$, for the intermediate region B in Fig. 3.2 is only about 2 seconds. On this time scale, $C_a(t)$ is a slowly changing concentration (quasi-steady function of time) which can be approximated as a constant in the

solution of Eqs. 4.20 and 4.22a-f. $Pe^{(t)}$ is the Peclet number in the tissue given later in this appendix. From simple continuity arguments, one can show that the radial velocity in the intermediate region B $\tilde{v}_r$ must decay as 1/r.

$$\tilde{v}_r = \left(\frac{2B}{\pi}\frac{d}{D}\tilde{V}_a\right)\frac{1}{r} \tag{4.A3}$$

Here $\tilde{V}_a$ is the average velocity through the junction orifices as defined in Eq. 4.19 in main text. If we choose velocity scale $\tilde{V}_B$ defined by

$$\tilde{V}_B = \frac{2B}{\pi}\frac{d}{D}\tilde{V}_a$$

to nondimensionlize $\tilde{v}_r$ in Eq. 4.A3, we obtain $v_r = 1/r$ in Eq. 4.A1. $Pe^{(t)}$ is thus

$$Pe^{(t)} = \frac{\chi_t \tilde{L}}{\tilde{D}_t}\tilde{V}_B \tag{4.A4}$$

where χ_t is the solute retardation coefficient in the tissue. Substituting Eqs. 4.A3 and 4.A4 into Eq. 4.A1, one has

$$\frac{\partial C_t}{\partial t} = \frac{\partial^2 C_t}{\partial r^2} + \frac{1}{r}\left(1 - Pe^{(t)}\right)\frac{\partial C_t}{\partial r} \tag{4.A5}$$

In Fig. 4.A, we have plotted $Pe^{(t)}$ as a function of the transcapillary pressure gradient in the physiological range. One concludes from Fig. 4.A that even at the highest value of ΔP, $Pe^{(t)} \leq 0.012$. Thus the second term in the parenthesis in Eq. 4.A5, which represents the convective transport, can be neglected and Eq. 4.A5 reduced to a unsteady pure diffusion equation. Therefore, the solution of Eq. 4.A5 subject to the initial and boundary conditions Eqs. 4.A2a-c can be obtained using the same approach presented in Fu et al. (1995). The solution procedure is shown in Chapter 3. The dimensionless result is

$$\alpha = \frac{2\pi}{B}\frac{\tilde{D}_t}{\tilde{D}^{(3)}}\frac{1}{\ln\frac{4t}{B^2} - 0.5772} \tag{4.A6}$$

Result (4.A6) is Eq. 4.23 in the main text.

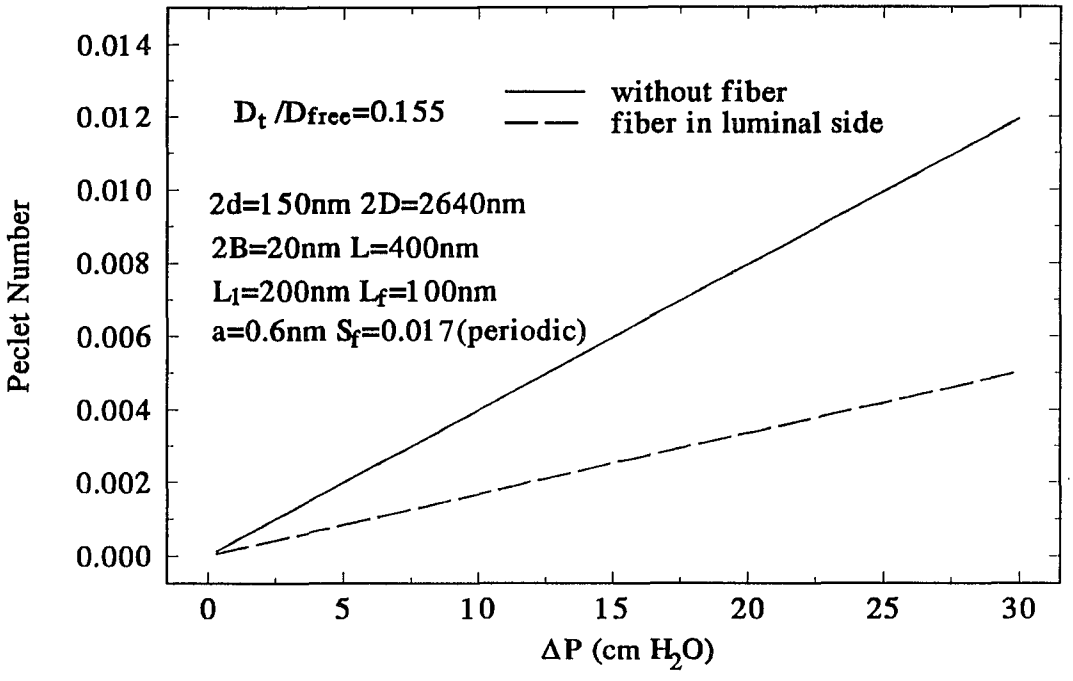

Fig. 4.A Peclet number in the tissue space as a function of pressure gradient across the vessel wall ΔP when (-) the cleft without matrix; and (--) matrix in the luminal side of the cleft.

BIBLIOGRAPHY

Abramowitz, M and Stegun, I.A. (1970). Handbook of Mathematical Functions with formulas, graphs and mathematical tables Dover publications, Inc. New York.

Adamson, R.H. (1990). Permeability of frog mesenteric capillaries after partial pronase digestion of the endothelial glycocalyx. J. Physiol. **428**, 1-13.

Adamson, R.H. (1992). An extension of the fiber matrix model of vascular permeability. Microvasc. Res. **43**, 352-356.

Adamson, R.H. and Clough, G. (1992). Plasma proteins modify the endothelial cell glycocalyx of frog mesenteric microvessels. J. Physiol. **445**, 473-486.

Adamson, R.H. and Michel C.C. (1993). Pathways through the intercellular clefts of frog mesenteric capillaries. J. Physiol. (London) **466**, 303-327.

Adamson, R.H., Lenz, J.F. and Curry, F.E. (1995). Quantitative laser scanning confocal microscopy on single capillaries: permeability measurement. Microcirculation. **1**(4), 251-265, 1994.

Anderson, J.L. and Malone, D.M. (1974) Biophys. J. **14**, 957-982.

Anderson, J.L. (1981) J. Theor. Biol. **90**, 405-426.

Bundgaard, M. (1980). Transport pathways in capillaries - in search of pores. Annu. Rev. Physiol. **42**, 325.

Bundgaard, M. (1984). The three-dimensional organization of tight junctions in a capillary endothelium revealed by serial-section electron microscopy. J. Ultrastruct. Res. **88**, 1-17.

Casely-Smith, J.R., Green, J.L., and Wadey, P.J. (1975). The quantitative morphology of skeletal muscle capillaries in relation to permeability. Microvasc. Res. **10**, 43-64.

Clough, G. and Michel, C.C. (1988). Quantitative comparisons of hydraulic permeability and endothelial intercellular cleft dimensions in single frog capillaries. J. Physiol. **405**, 563-576.

Crone, C. and Christensen, O. (1981). The electrical resistance of a capillary endothelium. J. Gen. Physiol. **77**,349.

Crone, C. and Levitt, D. (1984). Capillary permeability to small solutes. In "Handbook of Physiology"(E.M. Renkin and C. C. Michel, Eds.), Sect.2, Vol.4, pp.411-466. American Physiological Society, Bethesda, MD.

Curry, F.E. (1979). Permeability coefficients of the capillary wall to low molecular weight hydrophilic solutes measured in single perfused capillaries of frog mesentery. Microvasc. Res.

17, 290-308.

Curry, F.E. and Michel, C.C. (1980). A fiber matrix theory of capillary permeability. Microvasc. Res. **20**, 96-99.

Curry, F.E. (1984). Transcapillary exchange. in Handbook of Physiology (Renkin, E.M. and Michel, C.C. ed.), sect. 2, The Cardiovascular System, Vol. 4, The Microcirculation, Bethesda, Md, American Physiological Society, 309-374.

Curry, F.E. (1986). Determinants of capillary permeability: a review of mechanisms based on single capillary studies in the frog. Circ. Res. **59**, 367-380.

Curry, F.E. (1994). Regulation of water and solute exchange in microvessel endothelium: studies in single perfused capillaries. Microcirculation. **1**, No.1, 11-26.

Dean, J.A. Lange's Handbook of Chemistry. New York: McGraw-Hill, 1985.

Firth, J.A., Bauman, K.F., and Sibley, C.P. (1983). The intercellular junctions of guinea-pig placental capillaries: A possible structure basis for endothelial solute permeability. J. Ultrastruct. Res. **85**, 45-57.

Fox, J.R. and Wayland, H. (1979) Interstitial diffusion of macromolecules in the rat mesentery. Microvasc. Res. **18**, 255-276.

Frokjaer-Jensen, J. (1991). The endothelial vesicle system in cryofixed frog mesenteric capillaries analyzed by ultrathin serial sectioning. J. of Elec. Micro. Tech. **19**, No.3, 291-304.

Fu, B.M., Tsay, R., Curry, F.E., and Weinbaum, S. (1994). A junction-orifice-entrance layer model for capillary permeability: application to frog mesenteric capillary. ASME J. Biomech. Eng. **116**: 502-513.

Fu, B.M. Curry, F.E., and Weinbaum, S. (1995). A diffusion wake model for tracer ultrastructure-permeability studies in microvessels. Am. J. Physiol. (accepted)

Ganatos,P., Weinbaum S., and Pfeffer, R. (1980). A strong interaction theory for the creeping motion of a sphere between plane parallel boundaries. 2. Parallel motion. J. Fluid Mech. **99**(4), 755-783.

Ganatos, P., Weinbaum, S., Fischbarg, J. and Liebovich, L. (1981). A hydrodynamic theory for determining the membrane coefficients for the passage of spherical molecules through an intercellular cleft. Adv. Bioeng. **3**, 193-196.

Gingell, D. (1976). in Mammalian Cell Membranes, edited by Jamieson, G.A. and Robinson, D.M.. Boston, **1**, 198-223.

Happel, J. (1959). Viscous flow relative to arrays of cylinders. AIChE J. **5**, 174-177.

Karnovsky, M.J. (1967). The ultrastructural basis of capillary permeability studied with

peroxidase as a tracer. J. Cell Biol. **35**, 213-236.

Karnovsky, M.J. (1968). The ultralstructure basis of transcapillary exchange. J. Gen. Physiol. **52** , 645.

Kedem, O. and Katchalsky (1963). Permeability of composite membranes. Trans. Faraday Soc. **59**:1931-1953.

Landis, E.M. and Pappenheimer, J.R. (1963). Exchange of substances through the capillary walls. in Handbook of Physiology. Circulation, edited by Hamilton, W.F., Washington DC., Am. Physiol. Soc. sect. 2, **2**, 961-1034.

Levitt, D.G.(1975) Biophysical Journal **15**, 533.

Lee, J.S. (1969). Slow viscous flow in a lung alveoli model. J. Biomech. **2**, 187-198.

Lee, J.S., and Fung, Y.C. (1969). Stokes flow around a circular cylindrical post confined between two parallel plates. J. Fluid Mech. **37**, 657-672.

Luft, J.H. (1966). Fine structure of capillary and endo-capillary layer as revealed by ruthenium red. Fed. Proc. **25**, 1773-1788.

Mauri, R. (1995). Lagrangian self-diffusion of Brownian particles in periodic flow fields.Phys. Fluids **7**, No. 2, 275-284.

McConnell, B.L., Williams, K.C., Daniel, J.L., Stanton, J.H., Irby, B.N., Dugger, D.L., Maatman, R.W. (1964). J. Phys. Chem. **68**, 2941-2946.

Michel C.C. (1984). Fluid movements through capillary walls. In "Handbook of Physiology" (E.M. Renkin and C.C. Michel, Eds.), Sect. **2**, Vol. 4, 375-410. American Physiological Society, Bethesda, MD.

Michel, C.C. (1985). Vascular permeability - the consequence of Malpighi's hypothesis. Int. J. Microcirc. **4**, 265-284.

Michel, C.C. (1988). Capillary permeability and how it may change. J. Physiol. **404**, 1-29.

Ogston, A.G., Preston, B.N., and Wells, J. D. (1973). On the transport of compact particles through solutions of chain polymers. Proc. R. Soc. London, Ser. A. **333**, 297-316.

Pappenheimer, J.R., Renkin, E.M. and Borrero, L.M. (1951). A construction to the pore theory of capillary permeability. Am. J. Physiol. **167**, 13-46.

Pappenheimer, J.R. (1953). Passage of molecules through capillary walls. Physiol. Rev. **33**, 387.

Perl, W. (1971). Modified filtration-permeability model of transcapillary transport - A solution

of the Pappenheimer pore puzzle. Microvasc. Res. **3**, 233-251.

Perry, M.A. (1980). Capillary filtration and permeability coefficients calculated from measurements of interendothelial cell junctions in rabbit lung and skeletal muscle. Microvasc. Rec. **19**, 142-157.

Renkin, E.M. and Curry, F.E. (1978). Transport of water and solutes across capillary endothelium. in Transport Across Biological Membranes: Transport Organs, edited by Giebisch, G. and Tosteson, D.C.. Berlin, Springer-Verlag, **4**, 1.

Sangani, A.S., and Acrivos, A. (1982). Slow flow past periodic arrays of cylinders with application to heat transfer. Int. J. Multiphase Flow. **8**, 193-206.

Satcher, R.L. Jr. (1993) A mechanical model of vascular endothelial. Ph.D thesis, Dept. of Chem. Engr., MIT, Feb., 1993.

Schneeberger, E.E. and Hamelin, M. (1984). Interaction of circulating proteins with pulmonary endothelial glycocalyx and its effect on endothelial permeability. Am. J. Physiol. **247**, H206-217.

Schulze, C., and Firth, J.A. (1992). The interendothelial junction in myocardial capillaries: evidence for the existence of regularly spaced, cleft spanning structures. Journal of Cell Science **101**, 647-655.

Silbley, C.P., Bauman, K.F. and Firth, J.A. (1982) Cell Tissue Res. **223**, 165-178.

Sibley, C.P., Bauman, K.F. and Firth, J.A. (1983) Cell Tissue Res. **229**, 365-377.

Silberberg, A. (1987). in Microcirculation Edited by M. Tsuchiya et al., Elsevier, Amsterdam. **1**, 153-154.

Simionescu, M., Simionescu, N., Silbert, J.E. and Palade, G.E. (1981). Differentiated microdomains on the luminal surface of the capillary endothelium. II partial characterization of their anionic sites. J. Cell Biol. **90**, 614-621.

Simionescu, M., Simionescu, N., Santoro, F. and Palade, G.E. (1985). Differentiated microdomains of the luminal plasmalemma of murine muscle capillaries: segmental variations in young and old animals. J. Cell.Biol. **100**, 1396-1407.

Sneddon, I.N. (1966). Mixed boundary value problems in potential theory. John Wiley and Sons, New York. 264-267.

Starling, E.H. (1909). The Fluid of Body. London, Constable, 186.

Sullivan, R.R. and Hertel, K.L. (1942). Adv. Colloid Sci. **1**, 37.

Tsay, R., Weinbaum, S. and Pfeffer, R. (1989). A new model for capillary filtration based on recent electron microscopic studies of endothelial junctions. Chem. Eng. Commun. **82**, 67-102.

Tsay, R. and Weinbaum, S. (1991). Viscous flow in a channel with periodic cross-bridging fibers of arbitrary aspect ratio and spacing. J. Fluid Mech. **226**, 125-148.

Turner, M.R., Clough, G. and Michel, C.C. (1983). The effects of cationised ferritin and native ferritin upon the filtration coefficient of single frog capillaries. Evidence that proteins in the endothelial cell coat influence permeability. Microvasc. Res. **25**, 205-222.

Ward, B.J., Bauman, K.F. and Firth, J.A. (1988). Interendothelial junctions of cardiac capillaries in rats: their structure and permeabilities. Cell & Tissue Res. **252**, 57-66.

Weinbaum, S.,Tsay,R. and Curry,F.E. (1992). A three-dimensional junction-pore-matrix model for capillary permeability. Microvasc. Res. **44**,85-111

Wissig, S.L. (1979). Identification of the small pore in muscle capillaries. Acta Physiol. Scand. Supp. **463**, 33-44.

Yu, C.P., and Soong, T.T. (1975). A random cell model for pressure drop prediction in fibrous filters. J. Appl. Mech. Trans. ASME, June, 301-304.

Zeng, Y. and Weinbaum, S. (1993). Stokes flow through periodic orifices in channel. J. of Fluid. Mech. **263**, 207-226.